

Spring 5-2022

Studies of BONuS12 Radial GEM Detector and TCS Beam Spin Asymmetry in CLAS12

Jiwan Poudel
Old Dominion University, jiwan_poudel@yahoo.com

Follow this and additional works at: https://digitalcommons.odu.edu/physics_etds



Part of the [Elementary Particles and Fields and String Theory Commons](#), and the [Nuclear Commons](#)

Recommended Citation

Poudel, Jiwan. "Studies of BONuS12 Radial GEM Detector and TCS Beam Spin Asymmetry in CLAS12" (2022). Doctor of Philosophy (PhD), Dissertation, Physics, Old Dominion University, DOI: 10.25777/tjx2-ay25
https://digitalcommons.odu.edu/physics_etds/138

This Dissertation is brought to you for free and open access by the Physics at ODU Digital Commons. It has been accepted for inclusion in Physics Theses & Dissertations by an authorized administrator of ODU Digital Commons. For more information, please contact digitalcommons@odu.edu.

**STUDIES OF BONUS12 RADIAL GEM DETECTOR AND TCS
BEAM SPIN ASYMMETRY IN CLAS12**

by

Jiwan Poudel
M.S. May 2017, Old Dominion University

A Dissertation Submitted to the Faculty of
Old Dominion University in Partial Fulfillment of the
Requirements for the Degree of

DOCTOR OF PHILOSOPHY

PHYSICS

OLD DOMINION UNIVERSITY
May 2022

Approved by:

Stephen Bueltmann (Director)

Gail Dodge (Member)

Alexander Gurevich (Member)

Alvin Holder (Member)

Rocco Schiavilla (Member)

ABSTRACT

STUDIES OF BONUS12 RADIAL GEM DETECTOR AND TCS BEAM SPIN ASYMMETRY IN CLAS12

Jiwan Poudel

Old Dominion University, 2022

Director: Dr. Stephen Bueltmann

The Barely Offshell Nucleon Structure (BONuS12) experiment adopted the concept of spectator tagging technique to study the nearly-free neutron structure function F_2^n in the CLAS12 of Jefferson Lab. A novel Radial Time Projection Chamber (RTPC) detector was built, tested and integrated into the CLAS12 system to detect a back-moving low momentum tagged proton in $d(e, ep)X$ deep-inelastic scattering. It was a 40 cm long gaseous detector consisting of 3 layers of cylindrical GEM foils for the charge amplification, with the data readout directly from the surrounding padboard. The RTPC detected the recoiling spectator proton, in coincidence with the scattered electron in the CLAS12.

Nucleon structure functions are directly related to the partonic functions, quarks momentum distribution in one dimension. A Generalized Parton Distribution (GPD) came to the lime-light as it encodes the information of both longitudinal momentum and transverse position of partons inside the nucleons. Factorization of hard process such as DVCS allows to access GPDs. Timelike Compton Scattering (TCS), $\gamma p \rightarrow \gamma^* p$, is another process that allows to access the GPDs. TCS is studied experimentally in the CLAS12 of Jefferson lab using the quasi-real photoproduction of time-like photon which eventually decays to lepton pair.

This dissertation presents the concept of spectator tagging in BONuS12, and the research and development efforts during the BONuS12 preparation leading up to the successful data-taking during spring and summer 2020. In addition, analysis framework to extract the beam spin asymmetry of TCS events through the CLAS12 Run group A data is presented.

Copyright, 2022, by Jiwan Poudel, All Rights Reserved.

ACKNOWLEDGEMENTS

I have been connected to the BONuS12 Experimental group starting Summer 2016 as a graduate student. In these years, I grew up from a spectator to an expert of a BONuS12 detector: GEM based Radial Time Projection Chamber. In addition to the detector study, data acquisition and data analysis are two other important areas I tackled the most. Almost all of the research activities during my PhD are supervised and supported by Stephen Bueltmann, whose continuous encouragement and thorough guidance made me achieve the anticipated goals. His hands-on support and in-person assistance during the preparation of BONuS12 was quite remarkable. I am truly grateful to Dr. Bueltmann for his support, care and trust towards me, which stimulated to complete the assignments timely.

In addition to my supervisor, I am very thankful to Sebastian Kuhn, an important member of BONuS12 group I worked closely with, whose extended guidelines and instructions were extremely helpful to pave the way forward in the BONuS12 experiment. I also want to thank Gail Dodge, another BONuS12 member and a member of my dissertation committee, for her immense support and guidance during the prototyping of a flat detector and TDC based data acquisition. Many thanks to all other ODU BONuS12 group members, Gabriel Charles, Mohammad Hattawy, David Payette, Nathan Dzbenski and Madhusudhan Pokhrel who assisted me at different stages of my work.

Additionally, I would like to thank Eric Christy, Narbe Kalantarians, Carlos Ayerbe Gayoso and Aruni Nadeesharni, non-ODU members of BONuS12, for their hands-on support at the Jefferson Lab test-bench. My special thanks to Irakli Mandjavidze from Saclay, France for his remote as well as in person support throughout the setting-up of the DREAM based Data acquisition. I would further like to thank staff members of Jefferson lab, Brian Eng and Marc McMullen (Detector support group); Bob Miller, Denny Insley and Cyril Wiggins (Hall B Engineering group); Chris Cuevas, Mark Taylor and Benjamin Raydo (Fast Electronic group), Nathan Baltzel (Slow control), with whom I collaborated at various phases of BONuS12.

Furthermore, I want to thank Stepan Stepanyan for his continuous supervision, support and guidance in the TCS analysis. Thanks to Rafayel Paremuzyan and Joseph Newton for their cooperation in analyzing the CLAS12 Run group A data. Thank you all the members of the CLAS12 di-lepton analysis group providing invaluable suggestion and feedback on my data analysis work.

I want to extend thanks to the members of my dissertation committee, who have provided

invaluable feedback during these years. I also want to thank the department of Physics, ODU for all of the opportunities. Special thank you to all my professors and friends.

It was a life-long experience working with such amazing people. Thank you all who assisted me directly or indirectly.

Especially, I want to thank my parents, sister, my wife, Chandni, and all other family members for always being supportive and caring throughout all ups and downs.

TABLE OF CONTENTS

	Page
LIST OF TABLES.....	viii
LIST OF FIGURES	ix
Chapter	
1. INTRODUCTION.....	1
2. PHYSICS MOTIVATION AND FORMALISM	4
2.1 MOTIVATION OF THE BONUS12 EXPERIMENT	4
2.2 PHYSICS FORMALISM OF BONUS12	4
2.3 MOTIVATION OF TIMELIKE COMPTON SCATTERING	10
2.4 PHYSICS FORMALISM OF TCS	11
3. RTPC AND THE BONUS12 EXPERIMENT.....	18
3.1 THE BONUS12 DETECTOR: RTPC WITH GEM FOILS	18
3.2 PROTOTYPING AND TESTING A GEM DETECTOR.....	24
3.3 OBSERVATION AT THE ODU TESTBENCH.....	39
3.4 TARGET STRAW TESTING AT ODU	48
3.5 THE BONUS12 RTPC AND THE TESTBENCH AT JLAB.....	55
3.6 FINAL EXPERIMENTAL SETUP AND COMMISSIONING	67
3.7 DATA TAKING	85
4. CLAS12 RUN GROUP A AND THE TCS ANALYSIS.....	88
4.1 EXPERIMENTAL SET-UP OF RUN GROUP A	88
4.2 DATA PROCESSING.....	90
4.3 TCS ANALYSIS FRAMEWORK	94
4.4 TCS OBSERVABLE.....	104
5. CONCLUSION AND OUTLOOK.....	109
5.1 BONUS12 EXPERIMENT	109
5.2 TIMELIKE COMPTON SCATTERING	112
5.3 OUTLOOK.....	112
BIBLIOGRAPHY	114
APPENDICES	
A. PEDESTALS COMPARISON OF FEUS	117
B. BONUS12 GAS SYSTEM	120
C. COMMANDS AND CONFIGURATION FOR FEU	122

	Page
D. RG-A 2018 OUTBENDING FIDUCIAL	139
E. RG-A 2018 INBENDING DISTRIBUTIONS	143
VITA.....	147

LIST OF TABLES

Table	Page
1. Operating Voltages of the RTPC at Jlab Testbench during Cosmic run.	66
2. Amount (in Millions) of the collected data during the BONuS12 experiment at the Hall B of the Jefferson Lab in Spring and Summer 2020.	87
3. Summary of preliminary TCS beam spin asymmetry from this analysis of 2018 outbending and inbending runs.	107

LIST OF FIGURES

Figure	Page
1. Matter decomposing to the fundamental particles, quarks	1
2. Deep Inelastic scattering: Electron probing inside a proton with the exchange of virtual particle	2
3. F_2^n/F_2^p versus x with different nuclear corrections along with the indication of different theoretical predictions as $x \rightarrow 1$	5
4. Ratio of Final state interaction to the plane wave impulse approximation with the BONuS12 region highlighted in blue showing a very low effect	6
5. Inelastic scattering $ep \rightarrow e'X$	7
6. $d(e, e'p_s)X$ scattering with back-moving spectator proton.....	8
7. Spectrum of electron scattering events from deuteron as a function of corrected invariant mass W^* in $d(e, e'p_s)X$ compared to invariant mass W in $d(e, e')X$	9
8. Expected result of the BONuS12 experiment contributing data to both structure function (left) and quark ratio at higher Bjorken- x	10
9. Handbag diagram of the TCS reaction with time-like photon decaying to e^-e^+ pair ...	12
10. Diagram of Bethe-Heitler (BH) process with similar final states as TCS.....	14
11. Angles between the hadronic and leptonic planes in different frames involved in TCS reactions	14
12. TCS beam spin asymmetry with circularly polarised photon as a function of ϕ (left) for $t = -0.1 \text{ GeV}^2$ and $E_\gamma = 10 \text{ GeV}$, and as a function of $-t$ (right) for $Q'^2 = 4 \text{ GeV}^2$, $E_\gamma = 10 \text{ GeV}$	16
13. TCS beam spin asymmetry as a function of ϕ (left) for $Q'^2 = 7 \text{ GeV}^2$ and $-t = 0.4 \text{ GeV}^2$, and as a function of $ t $ (right) for $Q'^2 = 7 \text{ GeV}^2$ and $\phi = 90^\circ$ with θ integrated over $(45^\circ, 135^\circ)$	17
14. GEM foil (a) GEM under electron microscope (b) Electric field lines in GEM.....	18
15. Different layers of GEM in detectors (a) single layer (b) double layer.....	19
16. Effective gain of single and double layer of GEM detector.....	20

Figure	Page
17. Padboard readout pattern in the BONuS12 experiment.....	21
18. Transverse (top) and longitudinal (bottom) cross-sectional view of the RTPC in the BONuS12 experiment.....	22
19. BONuS12 GEMs storage box and test-bench in the clean-room of ODU with a GEM in HV test-box. Sectors on the top side of GEM could be seen in the zoomed picture at the bottom right side of text box	23
20. BONuS12 GEMs under optical test from top side after performing the HV: good GEM (left) and hair like contaminated GEM (right).....	24
21. Side view of a flat-prototype assembled using PCBs at ODU.....	25
22. High voltage power supply in Flat-prototype	26
23. Sketch of BONuS12 Test-bench showing necessary components	27
24. RTPC Prototype with the newly installed SHV connectors for each GEM layer replacing the existing potential divider circuit used in the eg6 experiment. Prototype adapter board is inserted from topside to test the new data acquisition electronics	28
25. New HV supply module from CAEN (a) HV supply unit nearby the detector (b) diagram of the modified HV supply from the available module to the RTPC	29
26. Gas mixing chamber for the drift gas (left), and the the gas gauge and flow controller (right) used for the prototype RTPC at ODU testbench.....	30
27. The BONuS12 prototype Adapter board with protection circuit near male connectors (top); Mini Edge Card (MEC8) at the end of the Hitachi Cable (bottom left); protection circuit in the adapter board (bottom right)	32
28. Block diagram of the DREAM chip	33
29. Block diagram of a Front End Unit (FEU) boards with four DREAMs in each side of PCB board.....	34
30. Back pannel of 6 FEUs with the 5 V DC power supply to a FEU at ODU testbench. Ethernet link is connected to transfer data in this Standalone test	35
31. Standalone data acquisition of the RTPC using FEU at ODU testbench	36
32. Pedestal data of all 512 channels of a FEU with individual channel pedestal fitted with the Gaussian function.....	37

Figure	Page
33. Mean pedestals (top) and the noise (bottom) of all 512 channels of a FEU plotted against channel number	38
34. Comparison of mean pedestals (top) and the noise (bottom) of all channels with 2 MEC8 cables connecting to the DREAM three and six of a FEU	40
35. Study of the variation of pedestal noise to check the connectivity of the DAQ electronics with the prototype adapter board.....	41
36. A scope used to observe the signal from the prototype with HeCO ₂ as drift gas	42
37. Typical signal of the prototype detector obtained by the DREAM based DAQ over a large time window and the zoomed view of signal fitting using split-normal distribution function with different rising and falling rate	43
38. Cosmic setup with two scintillators (one on top and another at center of the detector) for the coincidence trigger	44
39. Analysis of signals from the various proportion of gas mixtures of Helium and Carbon-dioxide. Probability is obtained with respect to the number of triggers (or events) processed. X-axis shows the gas mixtures and Y-axis the percentage of signals observed in the collected events.....	45
40. Calculation of drift time of the prototype using DREAM data for two gas mixtures, ArCO ₂ and HeCO ₂	47
41. Distribution of the peak ADCs of the observed signals for HeCO ₂ gas observed from DREAM electronics	48
42. Different Target straws (a) Spiral wound Kapton tube (b) Seamless Kapton tube from American Durafilm (c) Aluminized polyimide tube from Paramount Tubing.....	49
43. Set-up to test the polyimide straw gas leaking	51
44. Measurement of the straw diameter using vernier caliper(top) and wall thickness by micrometer (bottom).....	52
45. Evaluation of the straightness of the straw comparing with a straight stainless steel rod over a graph paper of 0.05 cm resolution	53
46. Leakage of Helium from Kapton straw visualized as bubble under water	53
47. Aluminum coated kapton straw under water showing the damaging of coating after a short time	54

Figure	Page
48. Leakage of Helium from the double sided aluminum coated straw visualized as bubble under water	55
49. BONuS12 gas panel with various sensors and safety components approved by the Hall B engineering (right); and control and monitoring of the drift gas (left)	56
50. Wiener MpodC crate with two HV modules for BONuS12 RTPC power supply	57
51. RTPC HV control Interface in EPICS programmable delay setting to ramp up the HV on all channels.....	58
52. BONuS12 RTPC and its installation on the CVT (Central Vertex Tracker) cart.....	59
53. Final version of two different size adapter boards to cover a complete row of connector in the BONuS12 RTPC	61
54. Standalone data acquisition of the RTPC using FEU at ODU testbench	62
55. Components of the CLAS12 BEU consisting of SBC, TI, SSP, SD. Twisted cable with crimp connector are connected to the TI and SD front panel for standalone operation.....	64
56. Cosmic test setup of the RTPC with 8 available FEUs to test the functionality and performance of the detector at Jefferson lab	65
57. RTPC system integrated to the CLAS12 monitoring showing promising result of occupancy, time distribution and pad hits of 8 Rows of connector during the cosmic test at EEL.....	67
58. Continuous Electron beam accelerator facility after 12 GeV upgrade	69
59. Upgraded CLAS12 detector system.....	70
60. Hall B beamline ustream of the CLAS12 detector showing part of the 2H line from the tagger magnet yoke to the entrance of the CLAS12	77
61. Completion of the RTPC installation in the CVT cart which hosted 6 FEU crates in the upstream	78
62. BONuS (RTPC) Overview GUI.....	79
63. Lab-view Interface of the RTPC gas control (top) and Target gas control (bottom) during the BONuS12 experiment	80

Figure	Page
64. RTPC detector installed in the CVT cart (on the left top side) ready to push inside the CLAS12 Solenoid (hollow seen as a white ring on the back).....	81
65. RTPC interlocks in EPICS	82
66. Occupancy and time distribution plot of the RTPC detector without solenoid magnetic field during the commissioning	83
67. Reconstruction of the cosmic radiation in the BONuS12 RTPC	84
68. Cabling work while installing the RTPC in the CVT cart.....	86
69. Design of the Hall B Cryogenic target inside the SVT.....	89
70. Summary diagram of the Data acquisition system of the standard CLAS12	90
71. CLAS12 interdependence of several subsystem within the CLARA framework for Event Builder (EB) service.....	92
72. CLAS12 forward detector to identify and separate the PIDs. Color grading shows the separation power (dark:highest and bright:lowest) in terms of the particle energy.....	93
73. Event Builder Cut on minimum HTCC photoelectrons required for the identification of electrons (left) and positrons (right).....	95
74. Energy deposited by electrons (left) and positrons(right) in the Calorimeter showing PCAL energy cut on 60 MeV for leptons	96
75. Quality cut of 5σ on parameterized sampling fraction provided on chi2pid of particle data bank for electron (left) and positron (right).....	97
76. Sampling fraction distribution of electrons and positrons as a function of momentum in six different sectors of CLAS12 (top: electrons, bottom: positrons).....	98
77. PCAL and ECIN sampling fraction correlation for electron (left) and positron (right) with red line $4SF_{ECIN} + 4.5SF_{PCAL} = 0.8$ to reject pions.....	100
78. Distribution of TCS kinematic variables among the sample events before the selected TCS kinematic cut.....	102
79. TCS kinematic variables after the selected MM^2 and transverse momentum cuts.....	103
80. Distribution invariant mass as a function of t variable and four different t bins to extract BSA.....	104

Figure	Page
81. Beam spin asymmetry calculated using the TCS analysis in various t bins (2018 Outbending run).....	105
82. Beam spin asymmetry calculated using the TCS analysis (2018 Inbending run).....	106
83. TCS beam spin asymmetry as a function of $-t$ in the recent publication of CLAS12 with the RG-A 2018 Inbending data comparing with theoretical models	108
84. RTPC tracks visualized in the online CLAS Event Display (CED) gui during the experiment	110
85. Spot on the target endcap by the irradiation of the electron beam during the first part of the BONuS12 experiment	111
86. Pedestal study of the FEU with the change in the gain capacitance as indicated in the right corner of plot	117
87. Pedestal noise analysis during the the cosmic test at the Jlab testbench consisting of six FEUs.....	118
88. Pedestal noise of the RTPC in the hall (FEU crates 1, 2 and 3).....	119
89. Pedestal noise of the RTPC in the hall (FEU crates 4, 5 and 6).....	119
90. BONuS12 gas system for both RTPC and Target (Gas shed outside of hall)	120
91. BONuS12 gas system for both RTPC and Target (Inside the hall)	121
92. Delay setting with various parameters	137
93. Positron sampling fraction in correlation with l_u (zoomed in near edge) in six different sectors of CLAS12. Red line shows the average sampling fraction corresponding to the x-axis bins.....	139
94. Electron sampling fraction in correlation with l_u (zoomed in near edge). Red line shows the average sampling fraction corresponding to the x-axis bins	140
95. Electron sampling fraction in correlation with l_v (top) and l_w (bottom) (zoomed in near edge). Red line shows the average sampling fraction corresponding to the x-axis bins	141
96. Positron sampling fraction in correlation with l_v and l_w (zoomed in near edge). Red line shows the average sampling fraction corresponding to the x-axis bins	142

Figure	Page
97. Distribution of e^- (left) and e^+ (right) of EC sampling fraction chi2pid (bottom) and HTCC photoelectrons (top) in 2018 inbending run	143
98. Sampling fraction distribution of e^- and e^+ as a function of momentum in six different sectors of CLAS12 for 2018 Inbending runs (top 6: electrons, bottom 6: positrons)	144
99. Distribution of TCS kinematic variables among the sample events before the selected TCS kinematic cut (2018 Inbending run)	145
100. TCS kinematic variables after the selected MM^2 and transverse momentum cuts (2018 Inbending run)	146

CHAPTER 1

INTRODUCTION

Ordinary matter in our visible Universe is understood to be made up of nucleons and electrons, of which electrons are fundamental particles with a mass 1837 times less than that of the nucleons. Nucleons, which are protons and neutrons, reside within a nucleus orbited by electrons to form atoms, and atoms can combine to form molecules as shown in Fig. 1. Nucleons are the core building blocks of our surroundings such as large stars to microscopic viruses. Nucleon binding and interactions determine the properties of nuclei, which further define the dynamics of nuclear reactions at different conditions. Theoretical and experimental research over the past several decades proved that protons and neutrons are not fundamental particles, but are composed of quarks bound by the exchange of gluons. Nuclear and particle physics is still very concerned with the origin and structure of the nucleus and nucleons. A major goal of modern physics is to understand the structure of the nucleons directly from the dynamics of the quarks and gluons and their interaction [1, 2].

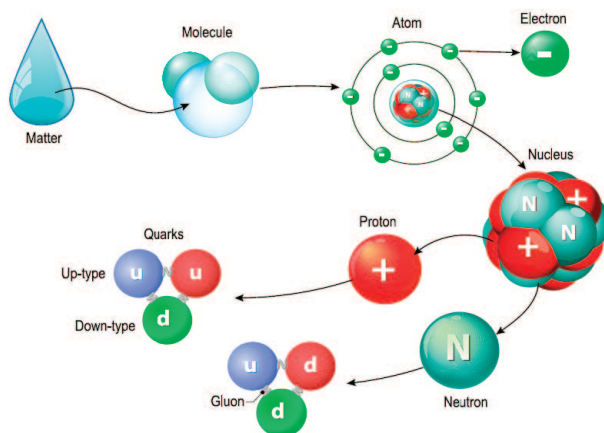


FIG. 1: Matter decomposing to the fundamental particles, quarks [1].

Scattering experiments such as in Fig. 2 have played a crucial role in exploring the structure of the nucleon. Electrons, as point-like fundamental particles, remain a powerful probe of matter at the most basic level in scattering experiments. The very first evidence for the structure of the proton came from measurements of the form factors by electron-nucleon elastic scattering in 1961, which later was awarded with the Nobel prize. The form factors are directly correlated to the spatial distributions of the electric charge and current density inside the nucleon. To explore the nuclear scale at the femto meter level, physicists rely on particle accelerators where high energy particles are generated and collided. These machines along with particle detector systems serve as microscopes for the core of matter, where protons and neutrons combine to form the nucleus, and quarks and gluons come together to build nucleons. In scattering experiments, the analysis of the interactions of particles depends on how well the particles in the final state are measured. The results are then compared with previous results and also used to make conclusions about theoretical predictions. If the reactants are also well known, the conclusions are more precise. Continuous research efforts of physicists over a half century made us to understand quite well details of these nucleons. However, there is still more unknown about nucleons, neutrons compared to protons. Neutrons lack charge and have a short life span which makes it difficult to accumulate and examine enough data on the free neutron.

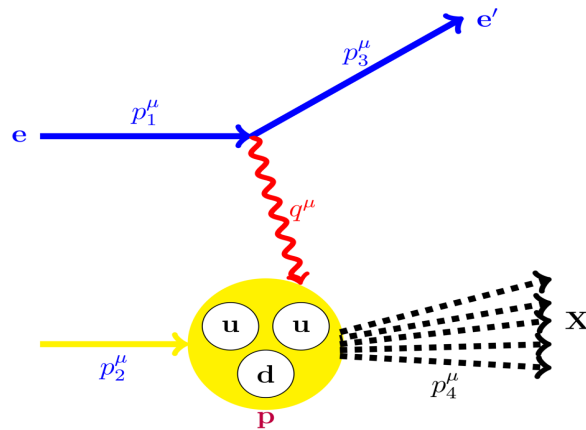


FIG. 2: Deep Inelastic scattering: Electron probing inside a proton with the exchange of virtual particle.

In addition, issues concerning with the quarks and gluons are more appealing such as the distribution of quarks and their interaction within a nucleon. Mass and spin of the nucleon still cannot be explained in terms of its constituent quarks and gluons. Experimental study of the quark distribution requires measurement of the neutron as well. But, details about the neutron structure can only be extracted from nuclear data disentangling the nuclear effects that are model dependent. These nucleon structures are governed by the fundamental theory of strong interaction, quantum chromodynamics (QCD). It describes the structure in terms of fundamental particles: partons, whose interactions follow from a quantum field theory (QFT). The partons, quarks and gluons, are observable only in reactions at high momentum transfers. So, the high Bjorken- x region that corresponds to the higher momentum transfer (Q^2) is a unique and critical testing area for theoretical models of the nucleon.

Different distribution functions such as form factors and parton distributions are available to describe the structure of nucleons, but they are special cases of a more general concept, generalized parton distributions (GPDs) in hadronic physics. The concept of GPDs has led to new methods of imaging the nucleon in the form of 3-D images with 2-D transverse space and 1-D momentum space. The mapping of the nucleon GPDs and a detailed understanding of the spatial quark and gluon structure have been widely considered as key objectives in the coming decades. They can be measured directly in hard exclusive scattering processes at large momentum transfer.

To expand the understanding of the neutron structure as well as the ratio of down to up quark (d/u), the **B**arely **O**ffshell **N**ucleon **S**tructure (BONuS12) group proposed a tagged proton experiment to study nearly free neutrons. In this work I am primarily focused on the BONuS12 motivations and physics, its goals, and the research and development efforts made to make the BONuS12 experiment ready for data taking in spring 2020 at Hall B of Jefferson Lab. In addition to the BONuS12 experiment (Run group F), I am also including analysis of Timelike Compton Scattering (TCS) from CLAS12 Run Group A (RG-A) data (the first experiment in the CLAS12 of Hall B which is different from the BONuS12 experiment) which aims to verify the universality of GPDs, accessing the Compton amplitudes. The next chapter (Chapter 2) includes the motivation and physics formalism of both of these experiments, and the following two chapters are dedicated to the details of the BONuS12 experiment (Chapter 3) and the TCS analysis (Chapter 4), respectively. I will conclude this manuscript summarising the accomplishments of my work in Chapter 5.

CHAPTER 2

PHYSICS MOTIVATION AND FORMALISM

2.1 MOTIVATION OF THE BONUS12 EXPERIMENT

The neutron has no net charge and also has a short decay time (less than 15 minutes) which makes it impossible to obtain a high density free neutron target. So unlike the proton, it is very hard to fully understand the structure of neutrons. Usually, the neutron structure is deduced from experiments on nuclear targets, especially deuterium, tritium and helium-3. However, the extraction of the neutron structure from a nuclear target requires corrections due to Fermi motion, bound states of nucleons, **F**inal **S**tate **I**nteractions (FSI), which are model dependent. Therefore large theoretical uncertainties arise in such measurements, especially when a large fraction of the neutron momentum is carried by a valance quark. Nearly free neutron structure could be extracted using the spectator tagging technique. The BONuS12 experiment at Jefferson Lab is designed to significantly reduce the nuclear binding effects in inclusive electron scattering on loosely bound (almost free) neutrons in deuterium by tagging low momentum (≤ 100 MeV/c) backward moving spectator protons in coincidence with the scattered electrons [3, 4]. The recent upgrade of Jefferson Lab's electron beam energy to 12 GeV, and the upgrade of the Hall B CLAS detector extends the interest to the higher momentum transfer region. Along with the upgraded CLAS12 detector system to detect the scattered electrons, a new Radial Time Projection Chamber (RTPC) detector successfully tracks the back-scattered protons.

2.2 PHYSICS FORMALISM OF BONUS12

The structure of the proton and neutron can be represented by their corresponding structure functions $F_2^p(x)$ and $F_2^n(x)$. The unavailability of free neutron targets leads to the use of light nuclei as target for comparative studies of the neutron structure along with the proton; applying nuclear correction due to Fermi motion, off-shell effects and FSI. Theoretical uncertainties due to nuclear models, however, plays a significant role extracting the data from nuclear targets for large values of the Bjorken scaling x . Bjorken scaling x in deep inelastic scattering represents the fraction of the momentum carried by the struck quark.

Large uncertainty in the ratio of the neutron to proton structure function as $x \rightarrow 1$ along with different theoretical predictions is shown in Fig. 3. At $x \rightarrow 1$, the valence quark follows the relation $u(x) = 2d(x)$ in the SU(6) symmetry model providing $F_2^n/F_2^p \rightarrow 2/3$ following expression 5. With broken SU(6) symmetry, the down quark is suppressed by a gluon exchange implying $d/u \rightarrow 0$ and $F_2^n/F_2^p \rightarrow 1/4$. In addition, the pQCD helicity conservation model predicts $d/u \rightarrow 1/5$ and $F_2^n/F_2^p \rightarrow 3/7$.

The BONuS12 experiment is especially designed to study the structure of free neutrons in Jefferson Lab with comparable detail and precision as achieved for the proton [3]. Hence, in spite of using a nuclear target (deuterium), the constraint on the spectator proton to very low momentum and almost backward scattering angle in the BONuS12 experiment ensures electron scattering from a nearly free neutron and also minimizes the FSI as portrayed in Fig. 4. So this method reduces the nuclear model uncertainties substantially.

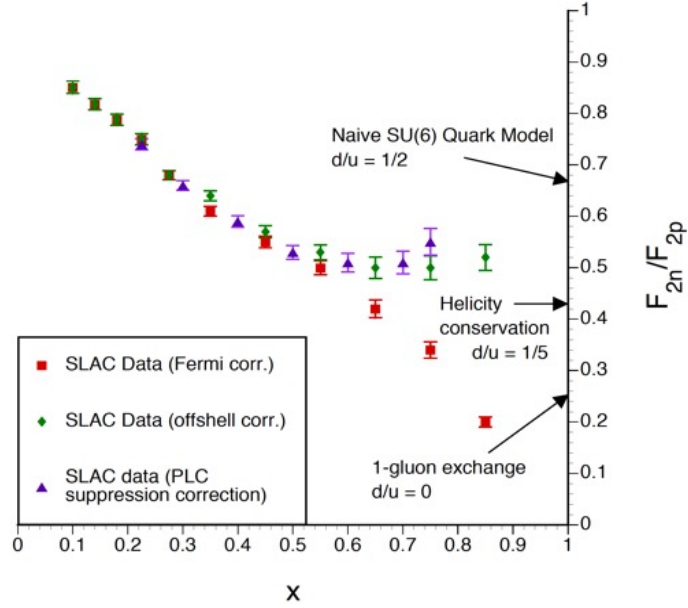


FIG. 3: F_2^n/F_2^p versus x with different nuclear corrections along with the indication of different theoretical predictions as $x \rightarrow 1$ [4].

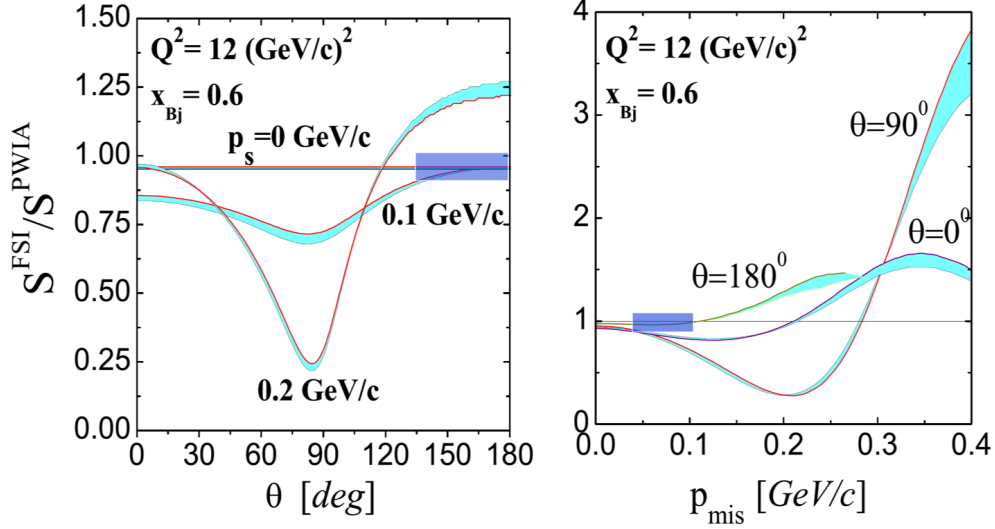


FIG. 4: Ratio of Final state interaction to the plane wave impulse approximation with the BONuS12 region highlighted in blue showing a very low effect [4].

To understand the detailed kinematics, invariant expression for the cross section of inelastic scattering $ep \rightarrow e'X$, as shown in Fig. 5, is expressed using the Lorentz invariant quantities. Some of these quantities are the momentum transfer square Q^2 which is defined as $Q^2 \equiv -q^2 = -q^\mu q_\mu$, invariant mass of the hadronic system W defined as $W^2 \equiv p_4^\mu p_{4\mu} = [p_2^\mu + q^\mu]^2 = M^2 - Q^2 + 2M\nu$ and the Bjorken scaling x defined by $x \equiv \frac{Q^2}{2p_2^\mu q_\mu} = \frac{Q^2}{2M\nu}$, where $q^\mu = (\nu, \vec{q})$ is the four momentum of the virtual photon and M is the mass of the target proton. The invariant differential cross section for this scattering is expressed similar to the Rosenbluth formula [5] as

$$\frac{d^2\sigma}{dx dQ^2} = \frac{4\pi\alpha^2}{Q^4} \left[\left(1 - y - \frac{M^2 y^2}{Q^2} \right) \frac{F_2(x, Q^2)}{x} + y^2 F_1(x, Q^2) \right] \quad (1)$$

where α is the fine structure constant, $y = \frac{p_2^\mu q_\mu}{p_2^\mu p_{1\mu}}$ is known as inelasticity and $F_1(x, Q^2)$ and $F_2(x, Q^2)$ are two structure functions.

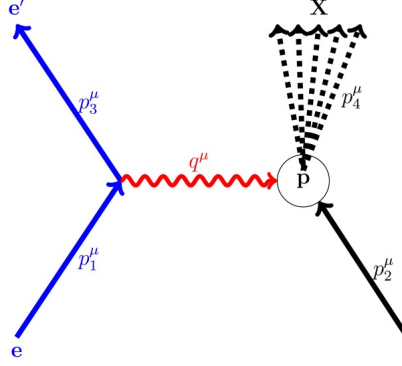


FIG. 5: Inelastic scattering $ep \rightarrow e'X$.

For deep inelastic scattering (DIS) $Q^2 \gg M^2 y^2$, we can write

$$\frac{d^2\sigma}{dx dQ^2} \approx \frac{4\pi\alpha^2}{Q^4} \left[(1-y) \frac{F_2(x, Q^2)}{x} + y^2 F_1(x, Q^2) \right] \quad (2)$$

Experimentally it was observed that the structure functions F_1 and F_2 are almost independent of Q^2 in the DIS regime, so we can write $F_1(x, Q^2) \rightarrow F_1(x)$ and $F_2(x, Q^2) \rightarrow F_2(x)$. It is also found that the Callan-Gross relation holds true in this regime, which states $F_2(x) = 2xF_1(x)$. So equation (2) can be written only in terms of one structure function in the deep inelastic region, which allows us to determine the structure functions of the target particle by measuring the differential cross section in the scattering process.

Furthermore, the Quark-Parton model states that the structure function of nucleons in the DIS regime can be expressed in the partonic distributions as

$$F_2(x) = x \sum_i Q_i^2 q_i(x) \quad (3)$$

where Q_i is charge (+2/3 for up and -1/3 for down quark) and $q_i(x)$ is the parton distribution function of particular type of quark within a nucleon. Hence, restricting the sum to the light flavours of quarks (valence quarks) only, we can write the structure functions of proton and neutron as

$$\begin{aligned} F_2^p &\approx x \left(\frac{4}{9}u(x) + \frac{1}{9}d(x) \right) \\ F_2^n &\approx x \left(\frac{4}{9}d(x) + \frac{1}{9}u(x) \right) \end{aligned} \quad (4)$$

Therefore

$$\frac{d}{u} \approx \frac{4F_2^n/F_2^p - 1}{4 - F_2^n/F_2^p} \quad (5)$$

So, if the structure function of the neutron is calculated precisely at higher value of x , it will help to understand the ratio of down and up quarks (d/u) using the Quark-Parton model.

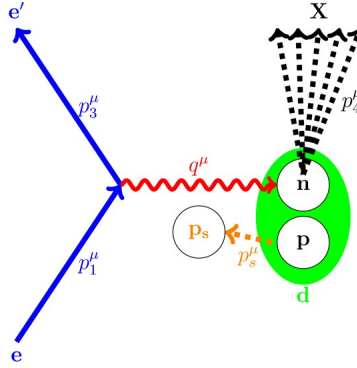


FIG. 6: $d(e, e' p_s)X$ scattering with back-moving spectator proton.

However, we don't have a free neutron target. So, in case of inclusive Deep Inelastic Scattering (DIS) $e + d \rightarrow e' + p_s + X$ with the spectator tagging proton as shown in Fig. 6, the kinematics are changed. This reaction can be expressed using the momentum four vector of off-shell neutrons $p_n^\mu \equiv (M_d - E_s, -\vec{p}_s)$, momentum four vector of spectator protons $p_s^\mu \equiv (E_s, \vec{p}_s)$ and four vector of momentum transfer $q^\mu \equiv (\nu, \vec{q})$ with $Q^2 = -q^2$. The Bjorken scaling x^* and the invariant hadronic mass of the final state W^* are then expressed as

$$x^* = \frac{Q^2}{2p_n^\mu q_\mu} \approx \frac{Q^2}{2M\nu(2 - \alpha_s)} \quad (6)$$

$$W^{*2} = (p_n^\mu + q^\mu)^2 \approx M^2 - Q^2 + 2M\nu(2 - \alpha_s) \quad (7)$$

where M is the mass of the off-shell neutron with four momentum p_n^μ and the parameter $\alpha_s = \frac{E_s - \vec{p}_s \cdot \hat{q}}{M_s}$ is known as the light cone momentum fraction of the spectator proton [4, 6].

Comparing with the previous expression of Bjorken scaling and invariant mass, it is obvious that x^* and W^* contain correction terms α_s obtained from the spectator proton. The effect of the correction term due to spectator tagging can be seen in Fig. 7, where the spectrum of electron scattering events for $d(e, e'p_s)X$ is plotted against the invariant mass compared with $d(e, e')X$. Therefore, by measuring the spectator proton, one can connect the state of the neutron in the deuteron and also select events that are unlikely to be affected by FSI.

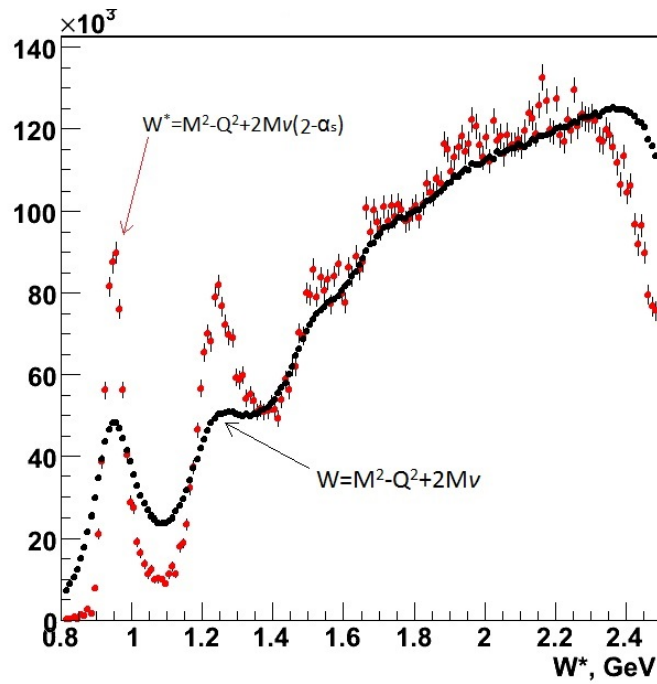


FIG. 7: Spectrum of electron scattering events from deuteron as a function of corrected invariant mass W^* in $d(e, e'p_s)X$ compared to invariant mass W in $d(e, e')X$ [7].

The BONuS12 experiment is expected to contribute the data points for both $F_2^n(x)/F_n^p(x)$ and $d(x)/u(x)$ at higher Bjorken- x as shown in Fig. 8 with the measurement of nearly-free neutrons. Additionally, other physics could be accessed using BONuS12 data. A new run group additional proposal to study the neutron-DVCS with BONuS12 [8] was also approved

in 2019.

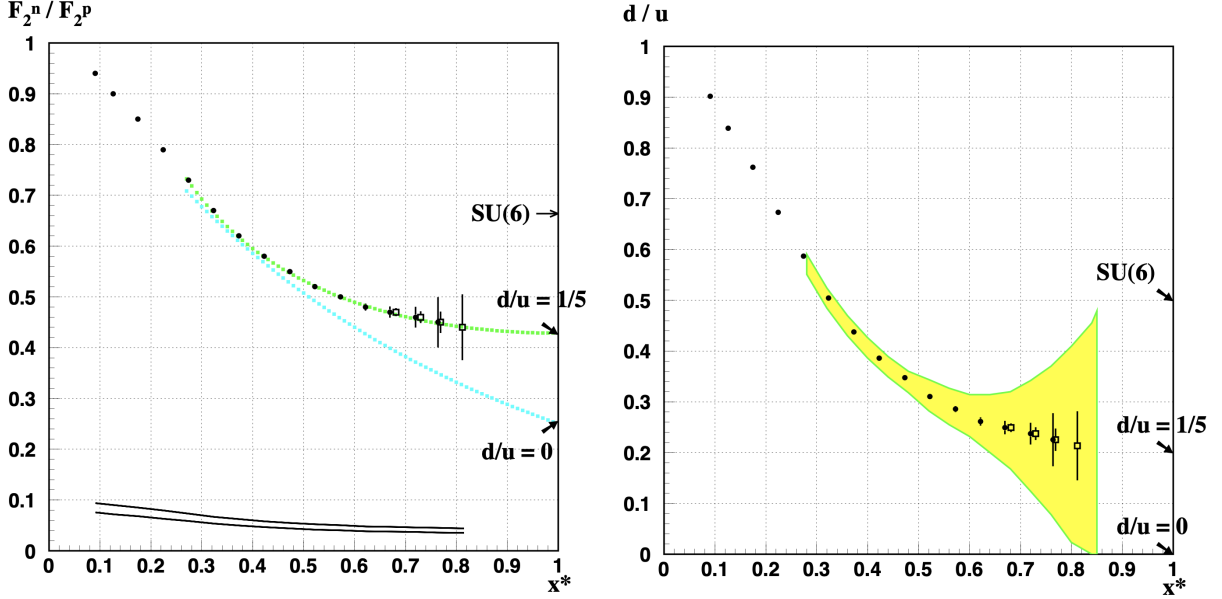


FIG. 8: Expected result of the BONuS12 experiment contributing data to both structure function (left) and quark ratio at higher Bjorken- x [3].

With the motivation of the extracting the structure function of neutron at large Bjorken- x , this work details the research and development activities of BONuS12 preparation and data taking at Jefferson lab in chapter 3. In addition to the instrumentation and laboratory work, I chose the data analysis of earlier nuclear experiment at Jefferson Lab. The motivation for the data analysis of Timelike Compton Scattering using the CLAS12 Run group A (RG-A) experimental data is presented below.

2.3 MOTIVATION OF TIMELIKE COMPTON SCATTERING

Deep inelastic scattering is described in the previous section detailing how the photon virtuality Q^2 much greater than the mass of the nucleon can probe its internal structure. The structure function ($F_1(x)$ and $F_2(x)$) are described in terms of the partonic distributions ($u(x)$)

and $d(x)$) that carry the information projected onto the direction of longitudinal momentum only. These functions miss the correlation with the transverse components. The concept of Generalized Parton Distributions (GPDs) [9–14], which encodes the unified information of both partonic distributions and the correlated transverse spatial densities within nucleons, is widely popular in the theoretical and experimental community of Nuclear and Particle Physics over the last 25 years. GPDs allow the imaging of the nucleon in three dimensional tomography. To access the GPDs, hard exclusive processes are important and the simplest and cleanest process is Deeply Virtual Compton Scattering (DVCS), $\gamma^*p \rightarrow \gamma p$ [10, 11]. Experimentally, the spin asymmetries in DVCS gives direct access to the imaginary part of the scattering amplitude, and hence, access to the GPDs at a specific kinematic point. The real part of the amplitude, which contains integrals of GPDs, is accessible either in cross section or in beam charge asymmetry measurements [15, 16].

A reverse process $\gamma p \rightarrow \gamma^*p$, where the final-state photon has a timelike virtuality ($Q'^2 > 0$), can also access both real and imaginary parts of the GPDs. This reverse process is known as Timelike Compton Scattering (TCS) for which the leading-twist formalism is well established as that for DVCS [15, 17]. With circularly polarized photons, TCS can provide direct access to the imaginary part of the scattering amplitude through the beam spin asymmetry as in DVCS. With an unpolarized photon beam, the real part of the scattering amplitude can be accessed through the azimuthal angular asymmetry of the lepton pair (decay products of the timelike photon). So, TCS is an alternative way to access the GPDs, which can test the Universality of GPDs; functions that don't depend on any process. TCS analysis could also provide additional constraints on the models and parameterizations of the GPDs. Furthermore, there was a pilot study performed by R. Parenduyan (see Refs. [18–20]) providing enough evidence that TCS with quasi-real photo-production could be studied with CLAS12 using 11 GeV electron beam energy in Jefferson Lab.

2.4 PHYSICS FORMALISM OF TCS

TCS with the timelike virtual photon decaying to an electron-positron pair can be expressed as

$$\gamma(q) + p(p) \rightarrow p(p') + \gamma^*(q') \rightarrow p(p') + e^-(k_-) + e^+(k_+) \quad (8)$$

in which the photo-production of timelike photon γ^* follows $q'^2 = Q'^2 > 0$. Here q and p within the parenthesis are four momenta of the incoming photon and the target proton. Similarly, k_- , k_+ and p' are the final state four-momenta of electron, positron and scattered

proton, respectively. Detailed theoretical description of the TCS process is presented in Refs. [15, 17, 21], and the relevant part to this analysis work is described below.

In the region where the timelike virtuality ($Q'^2 \equiv q'^2 = (k_+^2 + k_-^2)$) is large and the invariant momentum transfer square ($t \equiv (p' - p)^2$) is small, the TCS amplitude can be factorized into a hard scattering part calculable using perturbation theory, and a soft non-perturbative nuclear part representing GPDs parametrization. This condition is mostly satisfied with $Q'^2 > 2 \text{ GeV}^2$ and $-t < 1 \text{ GeV}^2$ [17]. Hard and soft parts of the TCS reaction in the leading order is expressed in the quark handbag diagram in Fig. 9.

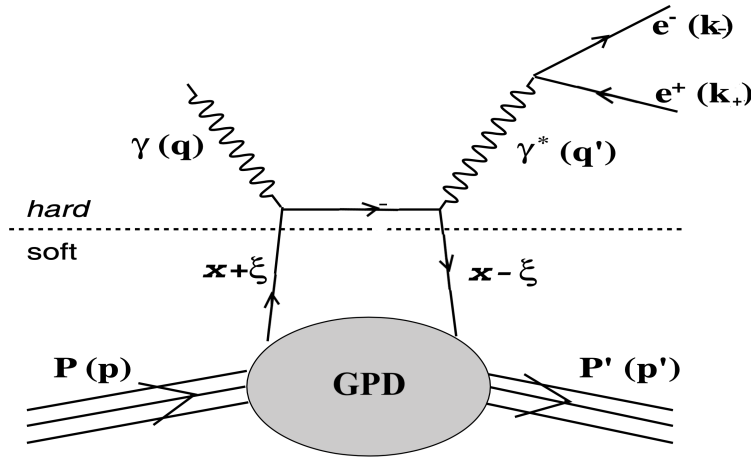


FIG. 9: Handbag diagram of the TCS reaction with time-like photon decaying to e^-e^+ pair.

There are four chiral even nucleon GPDs in the TCS process at leading twist: H , E , \tilde{H} and \tilde{E} . GPDs depend on three kinematic variables x , ξ , t . In the light cone frame, $x + \xi$ and $x - \xi$ define the initial and final quark longitudinal momentum fractions, respectively. In addition, the process involves a small transverse momentum transfer which is contained in t . At $\xi = 0$, GPDs provide access to the probability amplitude to find a quark in the nucleon with a longitudinal momentum fraction x at a given transverse impact parameter, which is related to variable t . GPDs entering into the TCS scattering are proton GPDs which is

the sum of the corresponding quark GPDs [17]. And the quark GPDs are related to parton distribution via the following model independent relations

$$H^q(x, 0, 0) = \begin{cases} q(x) & x > 0 \\ -\bar{q}(-x) & x < 0 \end{cases} \quad (9)$$

$$\tilde{H}^q(x, 0, 0) = \begin{cases} \Delta q(x) & x > 0 \\ \Delta \bar{q}(-x) & x < 0 \end{cases} \quad (10)$$

Similarly, form Factors (Dirac, Pauli, Axial and pseudo-scalar) can also be related to the GPDs through their first x moments:

$$\int_{-1}^1 dx H^q(x, \xi, t) = F_1^q(t) \quad (11)$$

$$\int_{-1}^1 dx E^q(x, \xi, t) = F_2^q(t) \quad (12)$$

$$\int_{-1}^1 dx \tilde{H}^q(x, \xi, t) = G_A^q(t) \quad (13)$$

$$\int_{-1}^1 dx \tilde{E}^q(x, \xi, t) = G_P^q(t) \quad (14)$$

GPDs enter into the Compton form factors (CFFs): $\mathcal{H}, \mathcal{E}, \tilde{\mathcal{H}}, \tilde{\mathcal{E}}$, as integrals over x as

$$\{\mathcal{H}, \mathcal{E}, \tilde{\mathcal{H}}, \tilde{\mathcal{E}}\}(\xi) = \int_{-1}^1 dx C^\pm(\xi, x) \{H, E, \tilde{H}, \tilde{E}\}(x, \eta)|_{\eta=-\xi} \quad (15)$$

Coefficient functions for even and odd parity sectors are

$$\xi C_{(0)i}^\mp(\xi, x) = \frac{Q_i^2}{1 - x/\xi - i0} \mp \frac{Q_i^2}{1 + x/\xi - i0} \quad (16)$$

Dealing with the TCS process, the Bethe-Heitler (BH) reaction also has the same final states ($\gamma p \rightarrow p' l^- l^+$) as shown in Fig. 10, in which the photon splits into a lepton pair and one of them interacts with the proton. Like in DVCS, the TCS amplitude also interferes with the BH amplitudes in the calculation. So, the total cross-section of the reaction can be expressed as $\sigma(\gamma p \rightarrow p' l^- l^+) = \sigma_{TCS} + \sigma_{BH} + \sigma_{INT}$

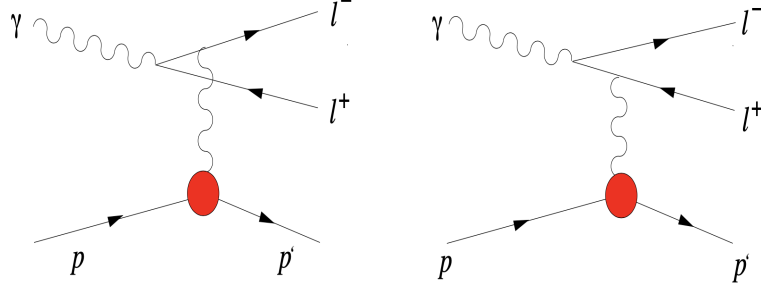


FIG. 10: Diagram of Bethe-Heitler (BH) process with similar final states as TCS [15].

To express the TCS cross-section, kinematic variables are Mandelstam variables $s = (p + q)^2$, $t = (p' - p)^2$, $Q'^2 = q'^2$, and the angle θ and ϕ described as shown in Fig. 11. θ is the angle between the outgoing lepton and proton (angle between k_- and p') in the l^+l^- center-of-mass frame, and ϕ is the angle between the reaction plane and the decay plane of the leptons.

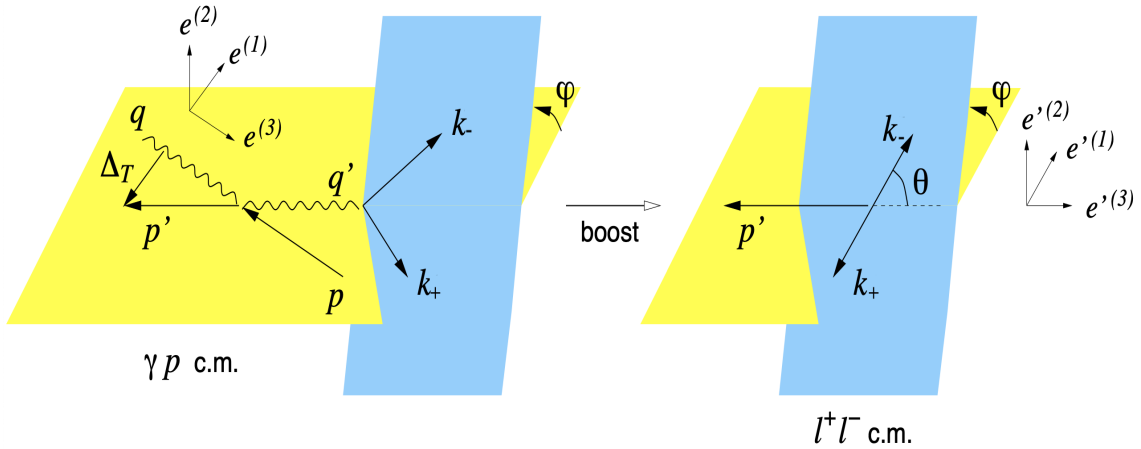


FIG. 11: Angles between the hadronic and leptonic planes in different frames involved in TCS reactions [15].

The unpolarized differential cross-section of the reaction $\gamma p \rightarrow p' e^- e^+$ is expressed as [17]

$$\frac{d^4\sigma}{dQ^2 dt d\Omega} = \frac{1}{64(2\pi)^4} \frac{1}{(2mE_\gamma)^2} |T^{TCS} + T^{BH}|^2 \quad (17)$$

where T^{TCS} and T^{BH} are the amplitude of the TCS and BH processes. Theoretical calculations [15, 17] show that the TCS cross-section is much smaller than the BH cross-section individually, which makes it harder to experimentally extract. There is an interference term hidden in the above expression within $|T^{TCS} + T^{BH}|^2$, which shows some inherent property of the two processes. The amplitude of the TCS and BH process transforms oppositely under lepton charge reversal. While the exchange of e^- and e^+ momenta makes the interference term odd, TCS observables that changes sign with $k_- \leftrightarrow k_+$ will project out of the interference term eliminating the BH contribution. The interference term in $\gamma p \rightarrow p' e^- e^+$ reaction with the circular polarization of photon ν is expressed as [15]

$$\begin{aligned} \frac{d^4\sigma_{INT}}{dQ^2 dt d\cos\theta d\phi} = & -\frac{\alpha_{em}^3}{4\pi^2 s^2} \frac{1}{-t} \frac{M}{Q'} \frac{1}{\tau\sqrt{1-\tau}} \frac{L_0}{L} \left\{ \left[\cos\phi \frac{1+\cos^2\theta}{\sin\theta} \text{Re } \tilde{M}^{--} \right. \right. \\ & \left. \left. - \cos 2\phi \sqrt{2} \cos\theta \text{Re } \tilde{M}^{0-} + \cos 3\phi \sin\theta \text{Re } \tilde{M}^{+-} + \mathcal{O}\left(\frac{1}{Q'}\right) \right] \right. \\ & \left. + \nu \left[\sin\phi \frac{1+\cos^2\theta}{\sin\theta} \text{Im } \tilde{M}^{--} - \sin 2\phi \sqrt{2} \cos\theta \text{Im } \tilde{M}^{0-} \right. \right. \\ & \left. \left. + \sin 3\phi \sin\theta \text{Im } \tilde{M}^{+-} + \mathcal{O}\left(\frac{1}{Q'}\right) \right] \right\} \quad (18) \end{aligned}$$

where α_{em} is the fine structure constant, $\eta = \frac{\tau}{2-\tau}$, $\tau = \frac{Q'^2}{2p \cdot q} = \frac{Q'^2}{s-M^2}$ analog to the Bjorken variable $x_B = \frac{Q^2}{2p \cdot q}$ in spacelike system. L , L_0 are expressed as

$$L = [(q - k_-)^2 - m_l^2] [(q - k_+)^2 - m_l^2] = \frac{(Q'^2 - t)^2 - b^2}{4} \quad (19)$$

$$L_0 = \frac{Q'^4 \sin^2\theta}{4} \quad (20)$$

Convention for the amplitude $\tilde{M}^{\mu'\mu}$ are as mentioned in Ref. [15], which contains the combination of Compton form factors, integral of GPDs over x as explained above. In the interference term, the photon polarization dependent and independent terms are related by reversing $\sin \leftrightarrow \cos$ and $\text{Im} \leftrightarrow \text{Re}$. This interference part of the reaction $\gamma p \rightarrow p' e^- e^+$ allows to access both real and imaginary part of the Compton form factor: real part without polarization, and imaginary part with circular polarization.

The imaginary part of the scattering amplitude is accessed through the calculation of the beam spin asymmetry using the circularly polarized photon beam as

$$A_{\odot U} = \frac{\sigma^+ - \sigma^-}{\sigma^+ + \sigma^-} \quad (21)$$

Here \odot represents the circularly polarised beam, and U as un-polarized target. Similarly, positive and negative indicates the cross-section related with right-handed and left-handed helicity.

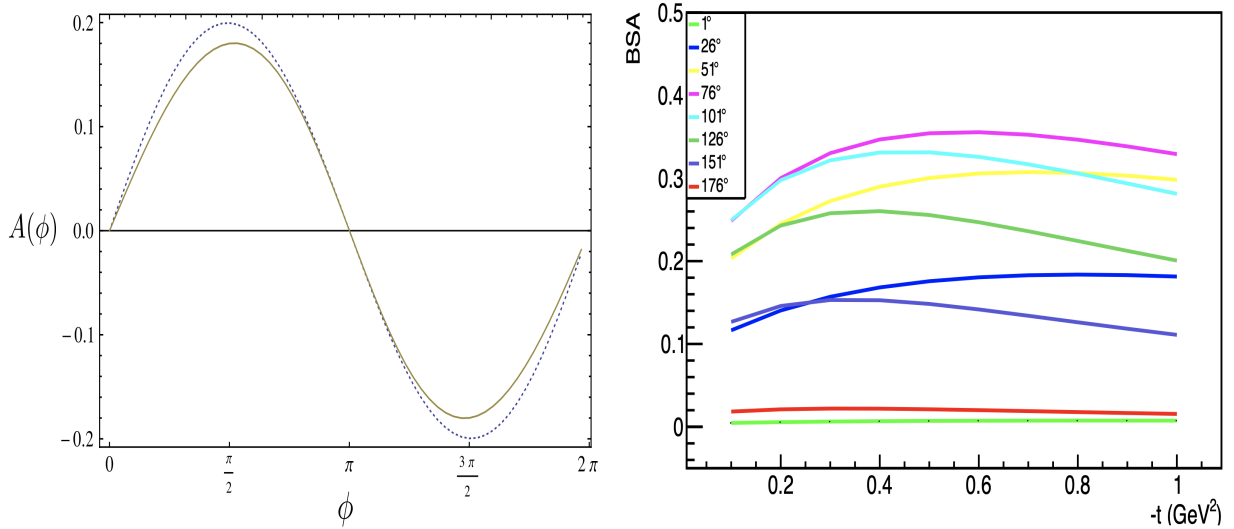


FIG. 12: TCS beam spin asymmetry with circularly polarised photon as a function of ϕ (left) for $t = -0.1 \text{ GeV}^2$ and $E_\gamma = 10 \text{ GeV}$ [21], and as a function of $-t$ (right) for $Q'^2 = 4 \text{ GeV}^2$, $E_\gamma = 10 \text{ GeV}$ [22].

The beam spin asymmetry predicted by theoretical calculation [21] is shown in Fig. 12 on the left, which shows the asymmetry for the leading order TCS reactions on the proton by a dotted line and the next to leading order by a solid line. On the right, beam spin asymmetry as a function of $-t$ is plotted at different θ with VGG model (theoretical model by M. Vanderhaegan, P. Guichon and M. Guidal). This plot on right was obtained by the CLAS12 dilepton group during the data analysis at Jefferson lab. Reference [17] also predicts

the beam spin asymmetry as shown in Fig. 13 which shows that there is no asymmetry for BH, separating out the BH contribution from the TCS sample, leading to an easy access to the imaginary part of the GPDs through asymmetry. Conflicting asymmetry between these two published theoretical predictions was resolved by the CLAS12 di-lepton group by contacting an author of Ref. [17], who provided a hint of wrong sign during their calculation.

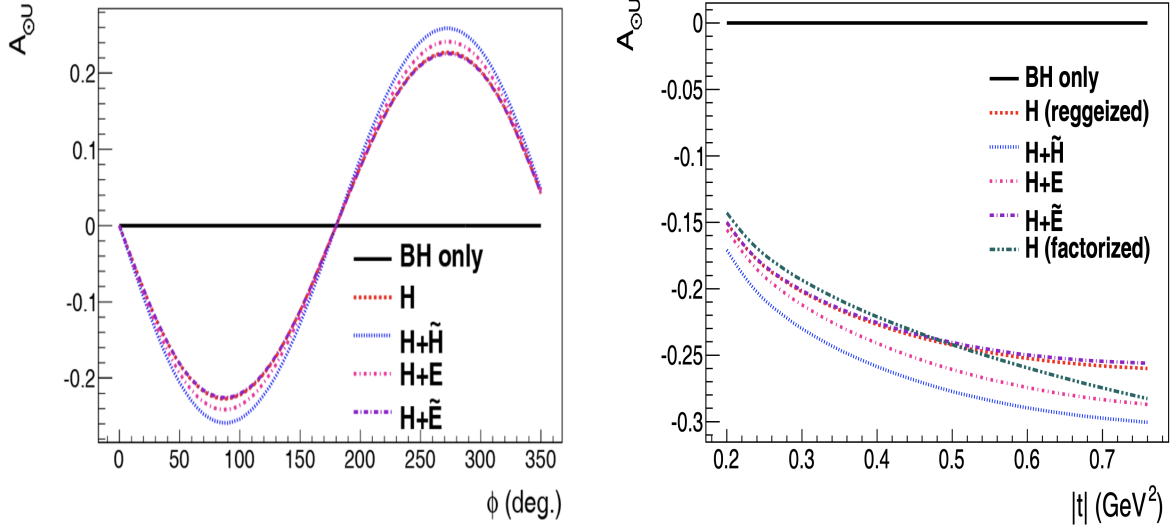


FIG. 13: TCS beam spin asymmetry as a function of ϕ (left) for $Q^2 = 7 \text{ GeV}^2$ and $-t = 0.4 \text{ GeV}^2$, and as a function of $|t|$ (right) for $Q^2 = 7 \text{ GeV}^2$ and $\phi = 90^\circ$ with θ integrated over $(45^\circ, 135^\circ)$ [17].

Preliminary analysis framework to analyze the TCS events and extract the beam spin asymmetry from the RG-A experimental data is detailed in chapter 4.

CHAPTER 3

RTPC AND THE BONUS12 EXPERIMENT

3.1 THE BONUS12 DETECTOR: RTPC WITH GEM FOILS

Different kinds of detectors have been developed and used for the detection of particles in Nuclear and Particle Physics for many years. Among the different types of detectors, gaseous detectors are widely used. However, there were several limitations of gaseous detectors as well, for example; inefficient performance due to low density of gaseous media, modification of electric field inside due to the presence of large number of ions, not adequate for higher space and time resolution, damage of readout electronics due to discharge, etc [23, 24]. Gas Electron Multiplier (GEM) foils help to remove several of these problems by separating the multiplication and readout functions in two different electrodes. The GEM is a thin polymer foil known as Kapton (a polyimide), which has a thin metal cladding on both sides and a high density of small holes. Typically, $50 \mu\text{m}$ thin insulating polyimide is used with $5 \mu\text{m}$ copper coating on both sides and pierced holes of diameter $40\text{-}140 \mu\text{m}$ with a density $50\text{-}100 \text{mm}^{-2}$. For high gain, the hole diameter is comparable to the foil thickness and also two third of the distance between holes [24–26]. A microscopic picture of a GEM foil is shown Fig. 14a.

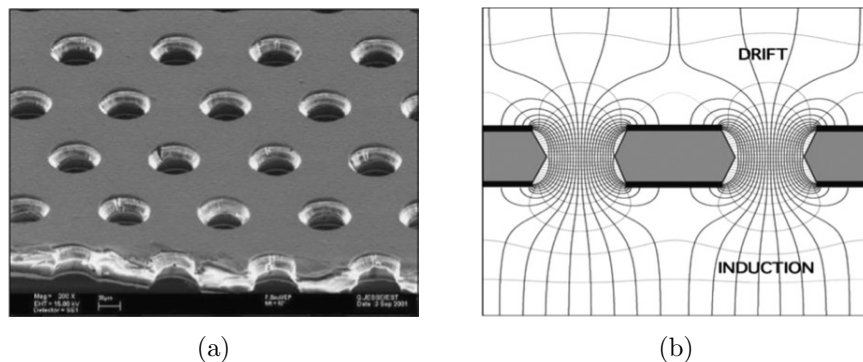


FIG. 14: GEM foil (a) GEM under electron microscope (b) Electric field lines in GEM [24].

A GEM layer is placed between the cathode and the readout electrodes (anode) inside the gaseous detector for pre-amplification as shown in Fig. 15a. The detector is filled with suitable ionizable gases. When a high potential difference is applied across the GEM, a large electric field is produced near the holes as shown in Fig. 14b. With an adequate potential difference applied across the GEM foil as well as the drift region, the electrons produced above the GEM foil drift towards the hole of the GEM and ultimately ionize the gases by acquiring large energy from the high electric field in the holes. This causes the multiplication of electrons through ionization by a factor of about 100, and a large portion of these electrons are transferred towards the anode where they are collected by the readout pad. Usually, a negative potential is applied across the GEM which is favorable for the readout to be at zero potential. This increases the choice of readout patterns: strips or pads. We can also obtain a two dimensional projective readout using thin multilayer board. The gain of the GEM depends on several factors but can be maintained to several thousands for various gases and conditions [25]. Absence of the $E \times B$ effect in the GEM detectors also reduces the distortion of field inside the detector.

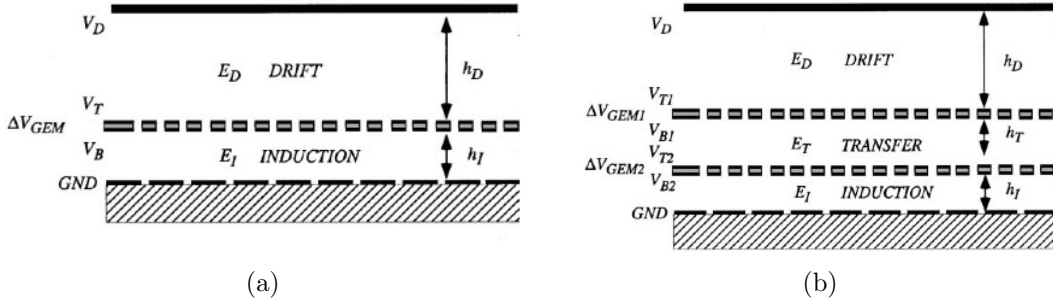


FIG. 15: Different layers of GEM in detectors (a) single layer (b) double layer [26].

Two or more GEMs can be cascaded together with a small gap between them as shown in Fig. 15b. An appropriate potential is applied to each GEM such that electrons flow towards the anode with proportional multiplication, each time they pass through the GEM holes.

Fractions of multiplied electrons from the first GEM are transferred to the second GEM and then into the induction region. The readout pattern at the anode collects avalanches of electrons achieving a very high gain without discharge. The comparison of gains for one and two GEM layers in a detector is shown in Fig. 16.

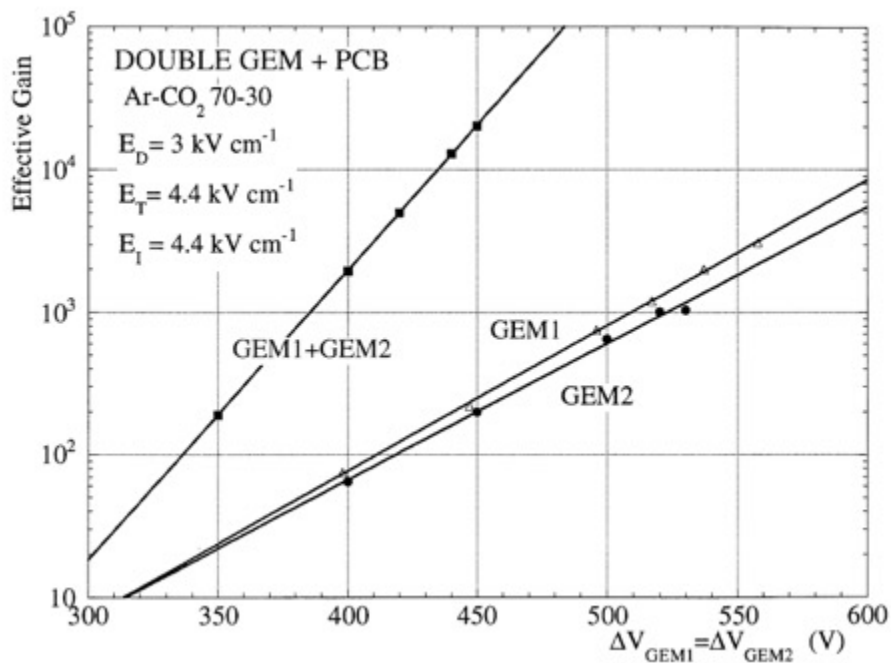


FIG. 16: Effective gain of single and double layer of GEM detector [26].

An important fact of the GEM detector is that the readout signal is only due to collected electrons, with no contribution of slow positive ions. This makes the GEM detector relatively fast, minimizing space charge problems. The proper choice of potential helps to strongly suppress the positive ion re-injection in the drift volume, which motivated the development of GEM Time Projection Chamber (TPC) [25, 27]. Furthermore a most powerful readout scheme: pixel pattern is also possible for the precise measurement while using GEMs. GEM detectors can be used for position accuracy of tens of microns and rate capabilities of 1 MHz

mm^{-2} [27, 28].



FIG. 17: Padboard readout pattern in the BONuS12 experiment.

The flexibility of GEM foils allows for non-planar detectors, which are used at CERN as well as Jefferson Lab in different experiments. The detector used for the detection of recoil protons in the first BONuS experiment at JLab was the GEM based RTPC (**R**adial **T**ime **P**rojection **C**hamber). The RTPC was a basic component of the BONuS experiment as it was used to detect the slow moving spectator protons. Along with the upgrade of the JLab beam energy and the CLAS spectrometer, the BONuS experimental group also proposed to extend the extraction of observable closer to $x \rightarrow 1$ upgrading the RTPC, an increase in the θ and ϕ acceptance as well as resolution. In the upgraded BONuS12 experiment, the 40 cm long RTPC had 3 cylindrical layers of curved GEM foils, each layer made up of a single foil. The RTPC had a 80 mm radius with the innermost GEM at 70 mm from the center and the other two layers spaced 3 mm further. Other than the GEM, the detector had a cylindrical readout board with conductive pads pattern of 2 degree in phi and 4 mm in the z -direction, as shown in Fig. 17. There was a total of 17,280 readout pads around the outermost cylindrical GEM of the RTPC at a radial distance of 80 mm from the center. Longitudinal and transverse cross-sectional views of the RTPC are shown in Fig. 18.

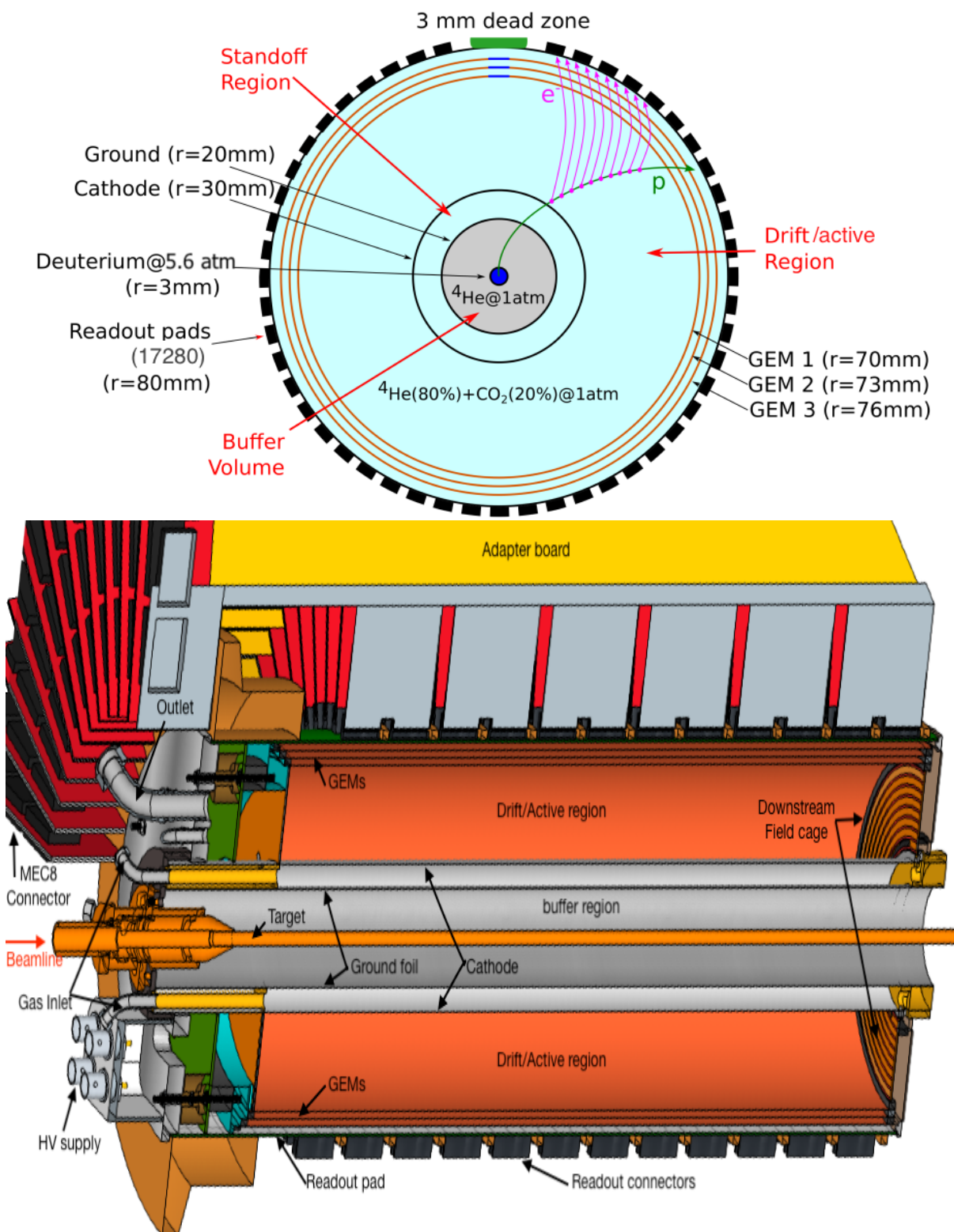


FIG. 18: Transverse (top) and longitudinal (bottom) cross-sectional view of the RTPC in the BONuS12 experiment.

The BONuS12 group ordered GEM foils from CERN which consisted of three different sizes of foil. The foils had the same length but the width was different to be able to make cylinders of different radii: 70, 73 and 76 mm. Those foils were stored in a storage box made up of acrylic plastic in which each foil was kept separated from another so that there was less chance of damaging foils sliding over each other. Also the storage box had a continuous flow of pure nitrogen gas at 5 Ltr/hr, which minimized the air contamination of the GEM foils. A separate box was prepared for the initial HV test of the GEMs as shown in Fig. 19. Each GEM foil for BONuS12 had 16 sectors lengthwise on top-side with 16 different HV panels, and one single layer on the bottom side. This design could make the detector workable even if one sector of any GEM has an issue. With this design only a particular sector of the detector with 22 degree in phi would be inefficient, and other parts would work perfectly.

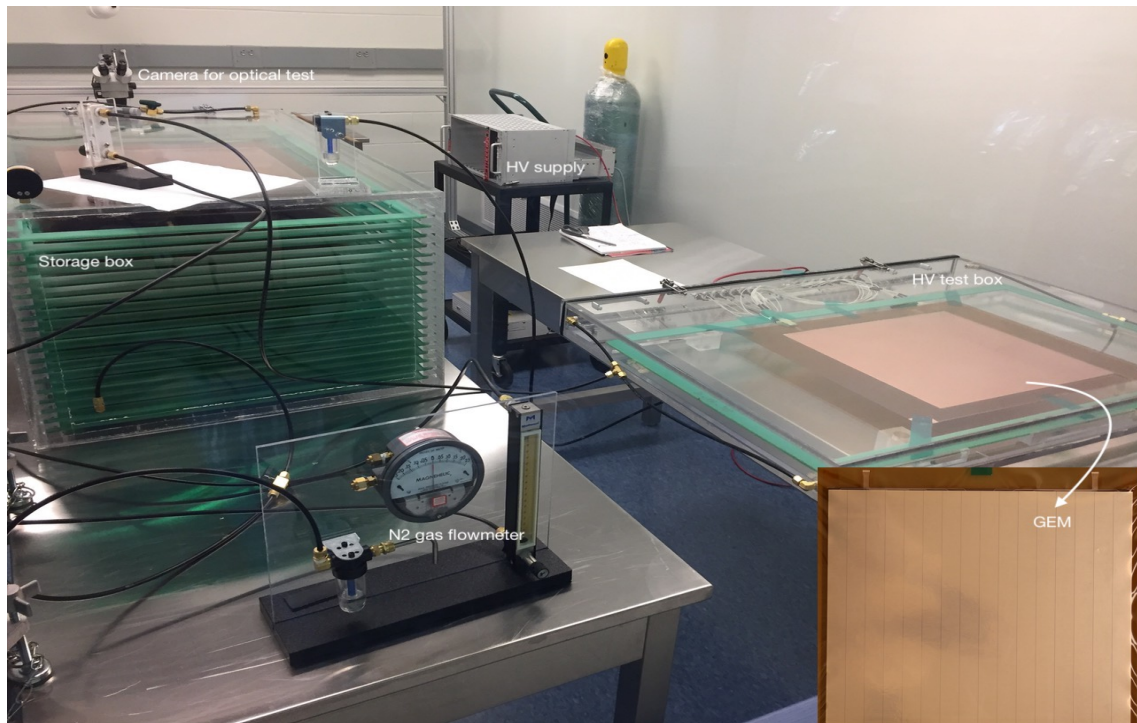


FIG. 19: BONuS12 GEMs storage box and test-bench in the clean-room of ODU with a GEM in HV test-box. Sectors on the top side of GEM could be seen in the zoomed picture at the bottom right side of text box.

High voltage (HV) testing of each GEM was performed at the ODU testbench setup, applying 500 V across each GEM. The HV test box with the testing GEM was first flushed with nitrogen gas to remove moisture inside before applying the HV. With a short pulse of HV, impurities and contamination could be burnt off from the GEM foil, observed by a decreasing current to a few nano-Amperes after a momentary increase to a few micro-Amperes. For the safety of the GEM foil in HV test, a current limiting resistor was used. After the HV test, the GEMs were tested optically with a high resolution camera. The photos were analyzed to see any discrepancy in the GEM, like closed holes of GEMs, burnt off GEMs due to HV, or some other contamination. Two examples of a GEM foil after the HV and optical testing, one good and another contaminated, are shown in Fig. 20.

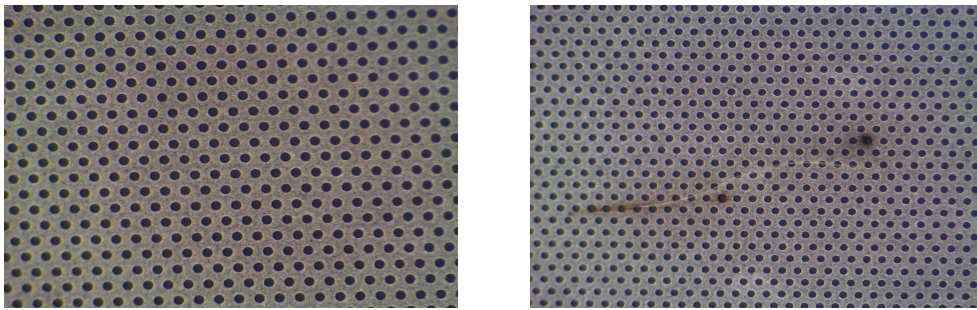


FIG. 20: BONuS12 GEMs under optical test from top side after performing the HV: good GEM (left) and hair like contaminated GEM (right).

3.2 PROTOTYPING AND TESTING A GEM DETECTOR

3.2.1 FLAT GEM PROTOTYPE

A flat prototype GEM detector with a stack of printed circuit boards (PCB) frames as shown in Fig. 21 was built to study the operating conditions of GEM detectors. The prototype consisted of two GEM layers which successfully detected beta particles from a

radioactive Sr-90 source as well as cosmic radiation. An oscilloscope was used to view the signals coming out of the strip readout of this flat prototype. The overall construction of the flat prototype was based on Fig. 22. The electric potential was maintained on different electrodes using a potential divider circuit developed on a bread-board. Current limiting resistors of $1\text{ M}\Omega$ were connected in series with the GEM layers to prevent the foil from burning due to over-current. The cathode was kept at a fixed negative potential with a high voltage supply at HV1. The GEM foils started to show discharge currents when the potential difference across it exceeded 375 V. Therefore, the supply at HV2 was kept below -1950 V, such that the potential difference across each GEM foil due to the potential divider circuit was within the safe limit (below 375 V). A gas mixture of Ar:CO₂ (90:10) was used as drift gas, and the drift field was maintained at $\sim 0.7\text{ kV/cm}$.

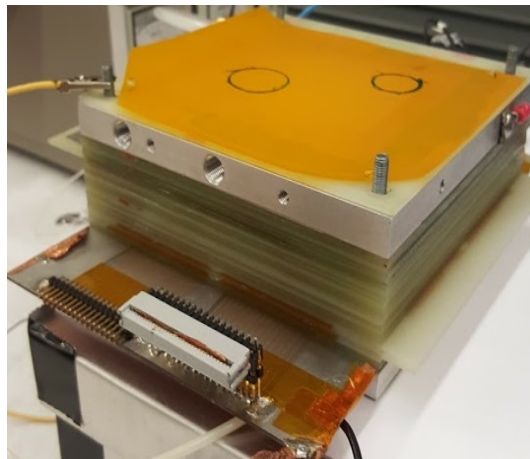


FIG. 21: Side view of a flat-prototype assembled using PCBs at ODU.

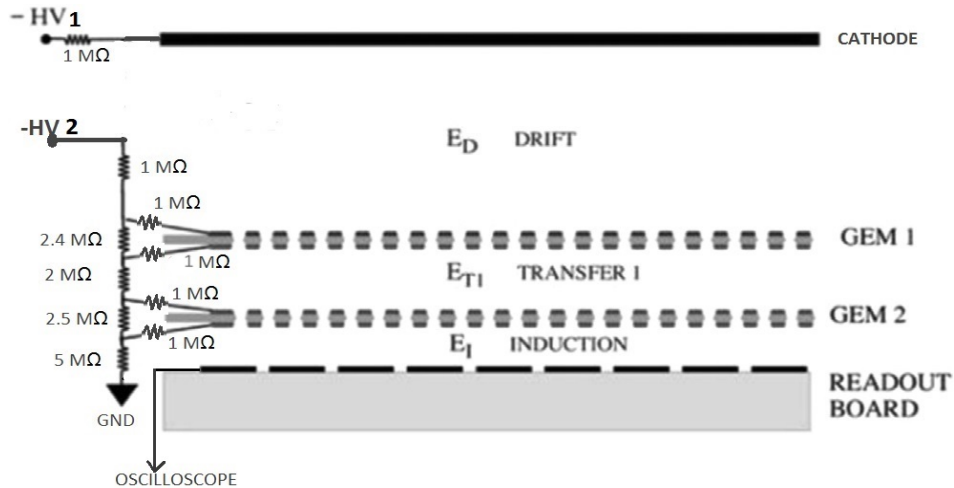


FIG. 22: High voltage power supply in Flat-prototype.

3.2.2 PROTOTYPE RTPC AND THE TESTBENCH AT ODU

The BONuS12 group borrowed the detector built and used by the eg6 experiment from Jefferson Lab while prototyping the new RTPC. Major components tested with this prototype were: HV supply system, readout adapter board and padboard, data acquisition system, drift gas mixture and gas panel. An initial testbench was established in ODU Physics Department Highbay area, which was later transferred to the EEL building at Jefferson Lab. The basic setup of our testbench is sketched in Fig. 23 which comprises of gas bottles, a gas panel, a HV system, a prototype RTPC, a DAQ crate consisting of FEUs and its low voltage supply, and a computer. The computer was set-up to control the standalone DAQ and the HV system. The components at the testbench and their performance are briefly described below:

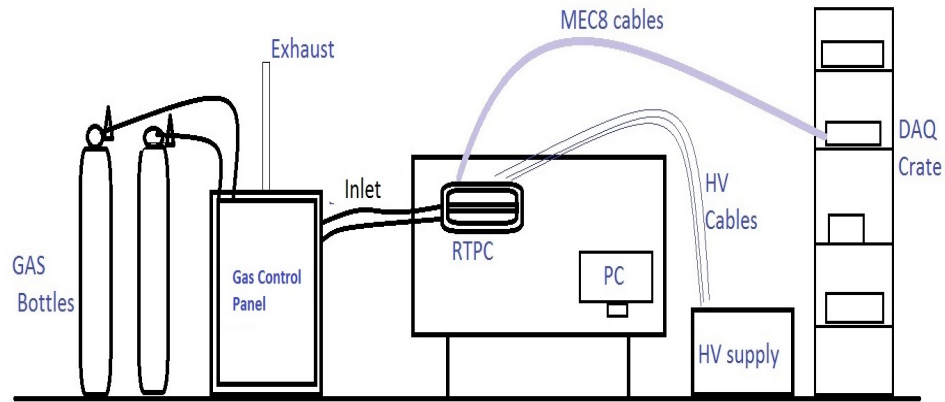


FIG. 23: Sketch of BONuS12 Test-bench showing necessary components.

- (a) **Prototype RTPC:** The eg6 RTPC (Fig. 24) was also a GEM detector with length 20 cm and radius 7 cm in which each cylinder is made up of two GEM foils [29]. Each GEM had four sectors on the inner side and a single outer sector. Potential divider (PD) circuit was used to supply HV to different layer of GEMs. As the prototype RTPC had two GEMs for each cylinder, two such PD circuit were used to supply HV on two halves of the cylindrical detector. Because of this PD circuit, each GEM had pre-defined combination of potential difference across it.

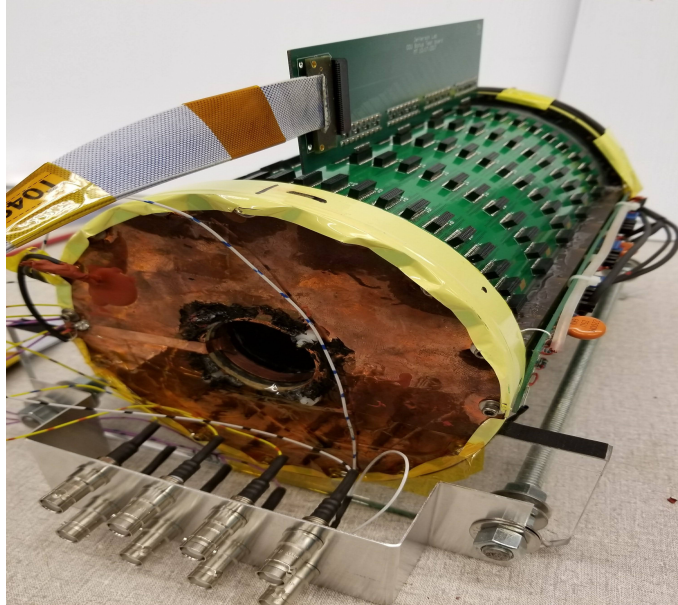


FIG. 24: RTPC Prototype with the newly installed SHV connectors for each GEM layer replacing the existing potential divider circuit used in the eg6 experiment. Prototype adapter board is inserted from topside to test the new data acquisition electronics.

- (b) **High Voltage (HV) supply:** A new HV supply for the BONuS12 RTPC was bought from CAEN, which could supply HV to individual GEM foils with higher resolution of current and voltage. This HV power supply is a combination of a CAEN main-frame S4527, A1515TGHP and A1015G (Fig. 25) from which we have eight HV cables connected to the detector. The power supply was controlled from a PC. We then had flexibility of supplying various combination of PD across each GEM and transfer region without worrying the over-biasing of any GEMs. This power supply was also better if any sector of the GEM behaved uniquely and current flow across GEM became higher. To use this new HV supply, we removed the potential divider circuit and installed new SHV jack connectors towards the downstream of the prototype as shown in Fig. 24.

One drawback of this new HV supply was a default 1 kV maximum supply across two channels, except 600 V max across GEMs. Because of this we modified the supply channel for the cathode as shown in Fig. 25. This modification allows us to supply ~ 3 kV across drift region with nominal operating voltage across GEMs about 380 V.

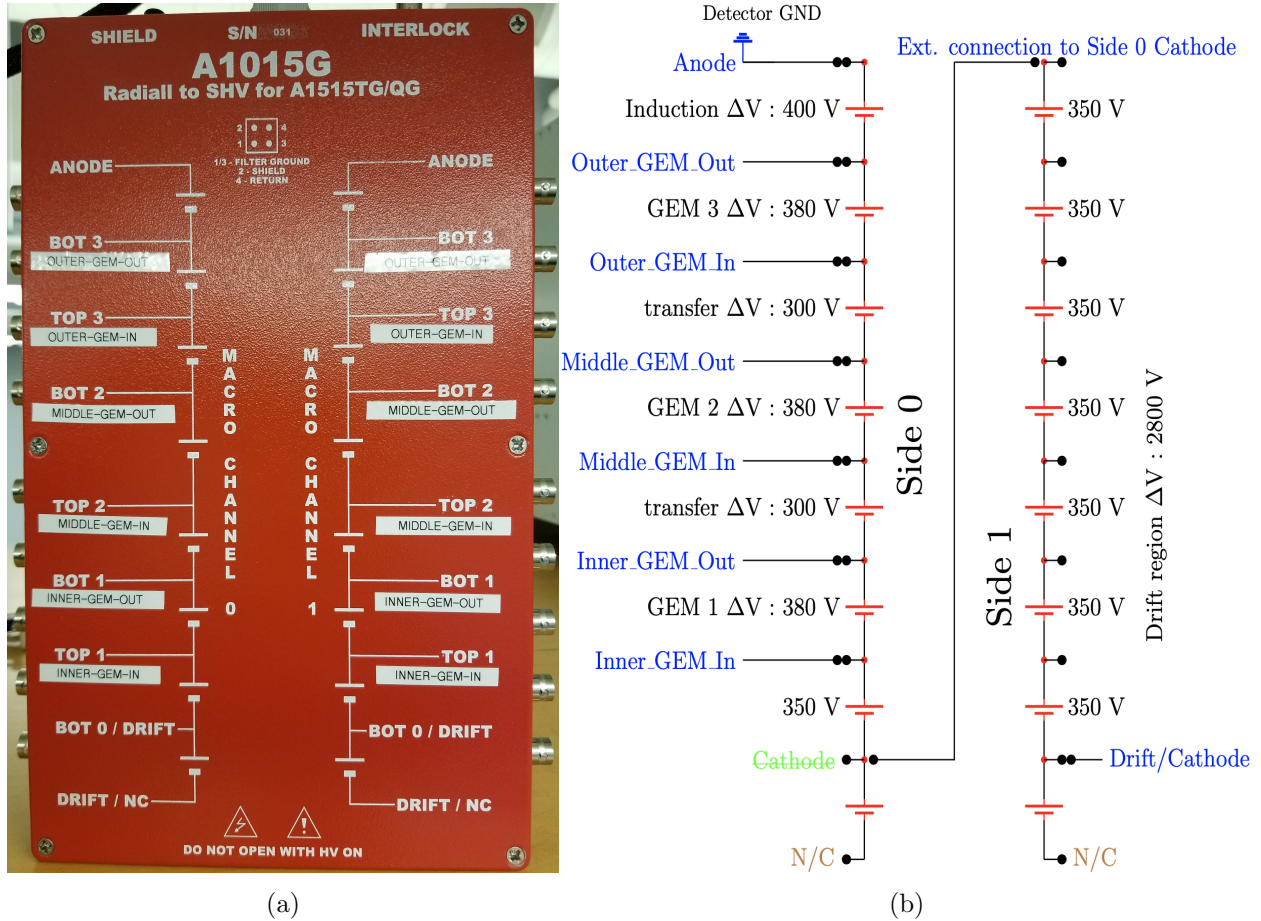
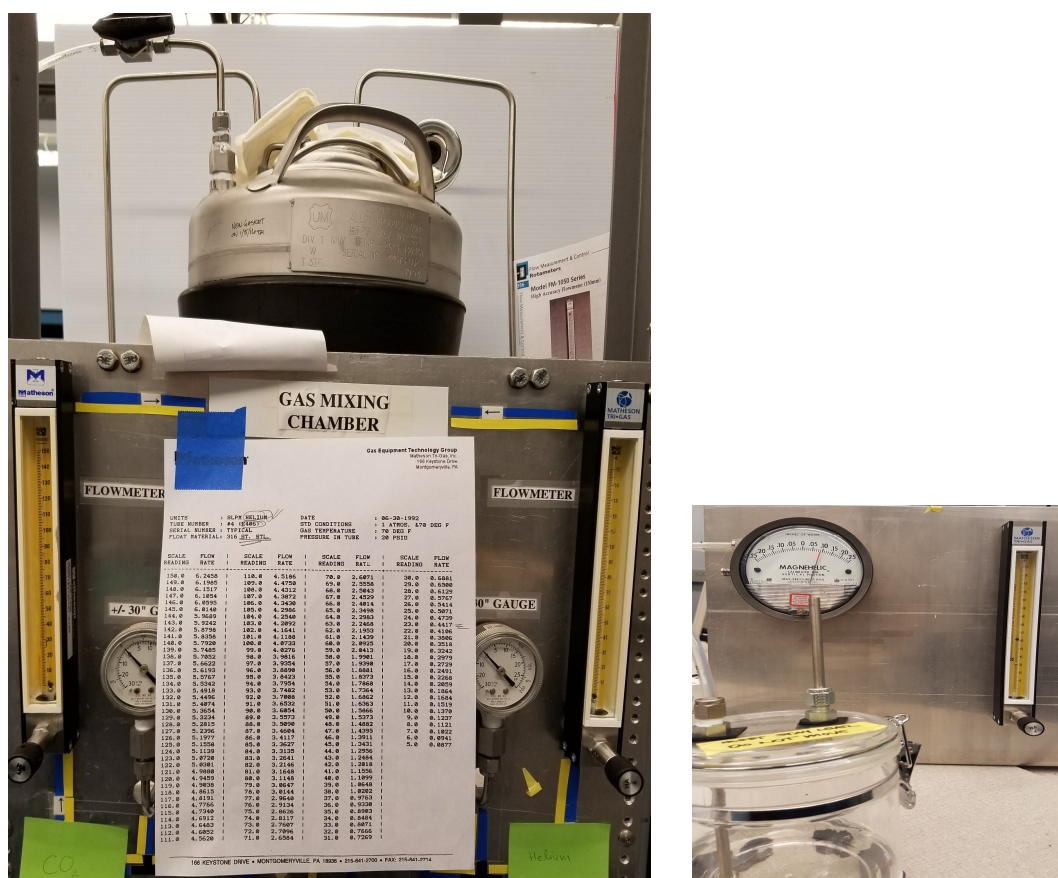


FIG. 25: New HV supply module from CAEN (a) HV supply unit nearby the detector (b) diagram of the modified HV supply from the available module to the RTPC.

(c) **Drift Gas and the controls:** The drift gas is the important component of the RTPC detector and during the prototyping ArCO_2 and HeCO_2 gas mixtures were used. ArCO_2 is a commonly used and safe non-flammable detector gas which allowed us to operate and investigate the detector with low operating voltages and small flow rates compared to HeCO_2 . Even if HeCO_2 is also non-flammable, it has a higher diffusion/leakage rate because of smaller size of helium. This requires higher flow of this gas mixture in the detector to maintain a pressure of fixed water column inside. In this experiment HeCO_2 was chosen because of its low electron density, non-flammability,

and self-quenching property. The low density allowed to have longer recoil tracks of protons, because of less multi-scattering and ionization. Furthermore, CO_2 improved the performance of the detector by improving quenching, raising the threshold of gas breakdown and minimizing diffusion. A study of different proportions of $\text{He}:\text{CO}_2$ using Garfield++ simulations [30] was carried out by the BONuS12 group. Furthermore, the prototype RTPC was also used at the testbench to see the results of different proportions of $\text{He}:\text{CO}_2$. Figure 26 shows the gas mixing chamber to mix two gases in a desired proportion. Helium and CO_2 were mixed by volume, controlling the flow of the two gases using a flow-meter at a particular pressure. This mixed gas was directly sent from the chamber to the detector in real time.



- (d) **Adapter board and MEC8 cable:** Signals from the RTPC readout pads were passed to the DAQ electronics using the adapter boards and micro-coaxial cable assemblies. Each BONuS12 adapter board was designed to transfer signals from 192 channels of the detector: one side had male pins which go into the connectors soldered on the pad-board and the other side had three 70 pin MEC8 connectors. These boards also consisted of protection circuits for individual channel to protect the DAQ electronics from surge currents. Signals are transferred through the printed circuits on flexible polymer in between two ends of the adapter board as shown of Fig. 27. Hitachi micro-coaxial cable assemblies with low capacitance were used to transfer signals from the adapter board to the Front End electronics Unit (FEU). Each ribbon like assembly has 64 flexible micro coaxial signal cables breaded together and assembled on the mini edge card at two ends of cable as shown in Fig. 27. Out of the 35 pins in each side of the MEC8, the outer two pins and one center pin are grounded. With such configuration, three Hitachi MEC8 cable assemblies of length ~ 1.5 m are used to transfer signals from one adapter board to the Front End Unit (FEU).

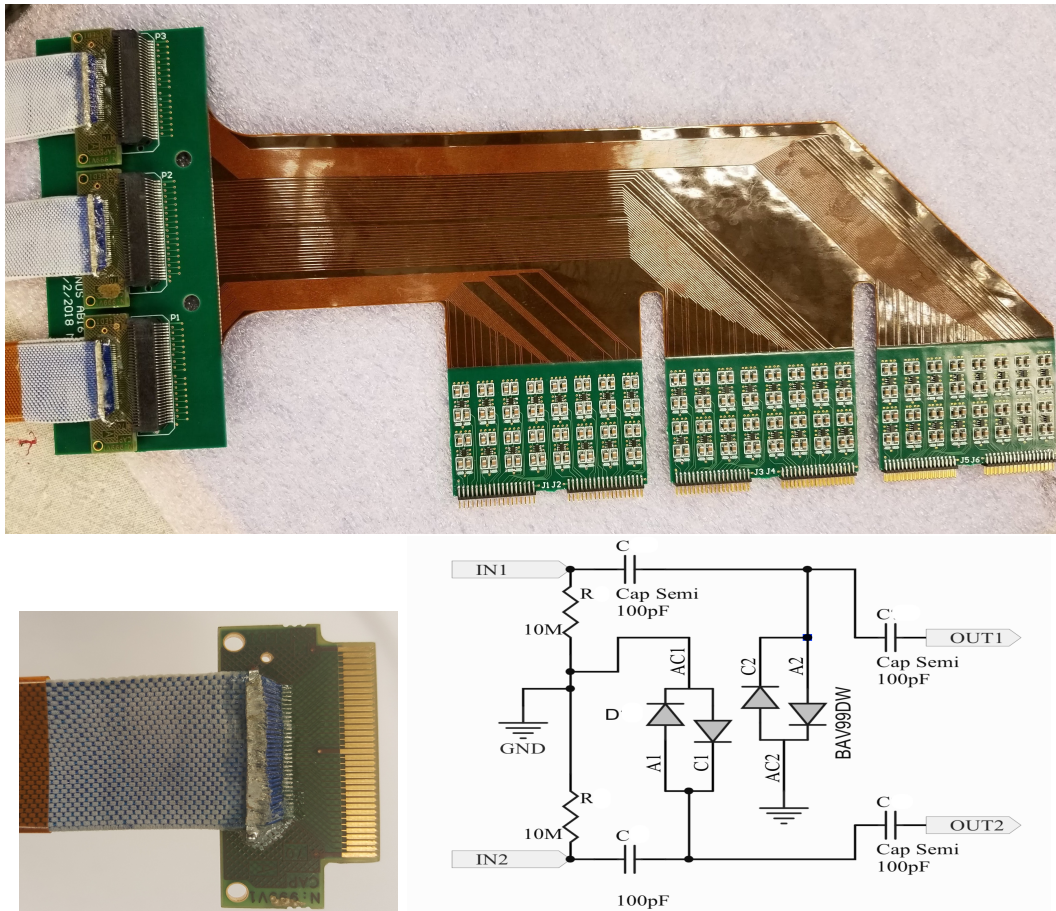


FIG. 27: The BONuS12 prototype Adapter board with protection circuit near male connectors (top); Mini Edge Card (MEC8) at the end of the Hitachi Cable (bottom left); protection circuit in the adapter board (bottom right).

- (e) **DREAM and FEU:** The SACLAY group (France) at the time of the detector development produced a new 64 channel ASIC, called DREAM (for Dead-timeless Readout Electronics ASIC for Micromegas) which could sustain the needed 20 kHz readout rate and provide a $16 \mu\text{s}$ deep trigger pipeline [31]. A block diagram of the DREAM ASIC is shown in Fig. 28 in which each channel has integrated a charge sensitive amplifier (CSA), a shaper/filter, 512-cell Switched Capacitor Array (SCA) analog circular buffer and discriminator for trigger building. It has programmable configuration parameters, which would make it suitable for various detectors. The gain of the amplifier is chosen

by selecting a range of input capacitances among four possible values between 50 fC to 600 fC. Similarly, the peaking time of the shaper is also programmable from sixteen different values between 50 ns to 900 ns. Event sizes of up to 255 samples per trigger with a sample size of 40 ns can be continuously sampled in a 512-cell switched capacitor array circular buffer, which acts as the trigger pipeline memory. This makes the DREAM worthier as it performs dead-timeless readout of up to 20 MHz for a trigger rate of up to 20 kHz [32]. Upon receiving the trigger, a programmable number of samples of all channels, corresponding in time to the event, is read out serially through a differential analog buffer. The sampling is not stopped during the readout process, which allows nearly dead-timeless operation. The DREAM chip is capable to operate with both signal polarities.

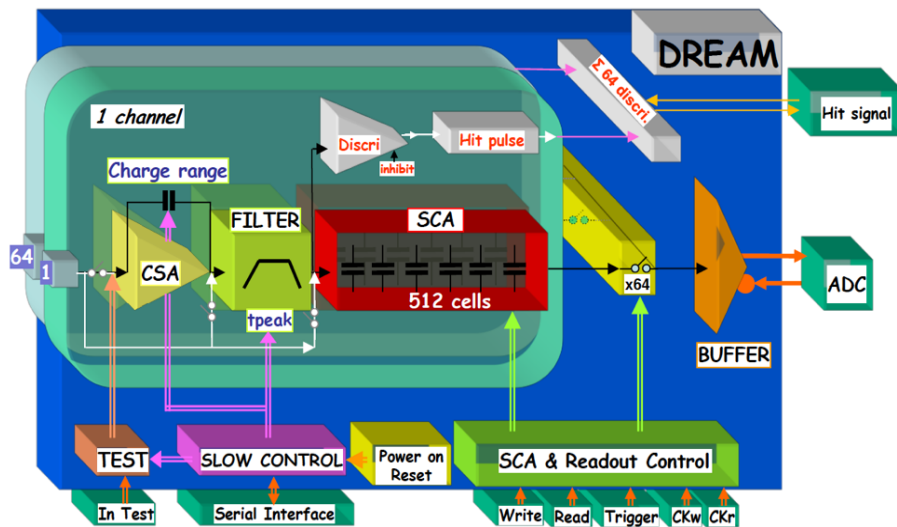


FIG. 28: Block diagram of the DREAM chip [32].

The FEU is comprised of eight input connectors, eight DREAM ASICs, and an 8-channel flash ADC as shown in Fig. 29. The FEU is a 266 mm high, 220 mm wide, and 25.4 mm thick module, which can be powered by a 4.3 V or 5 V source and

it consumes ~ 20 W of energy when all eight DREAMs operate together. The input channels of the DREAM ASICs are connected to the detector readout with the adapter boards containing the protection circuit (Fig. 27). The pre-amplification, shaping, and trigger pipeline functionalities are implemented in the DREAM chips as mentioned above. The analog samples from the eight DREAMs are digitized by an 8-channel 12-bit flash ADC (AD9222). The eight serial streams of digital data are delivered to the FPGA hosted in the FEU board. The digital section of the board comprises an FPGA from the Xilinx Virtex-6 device family, its memory, a 2 Mbyte synchronous SRAM, small form-factor pluggable (SFP) transceivers, an on-board clock synthesizer, and an auxiliary trigger interface circuit [31, 33].

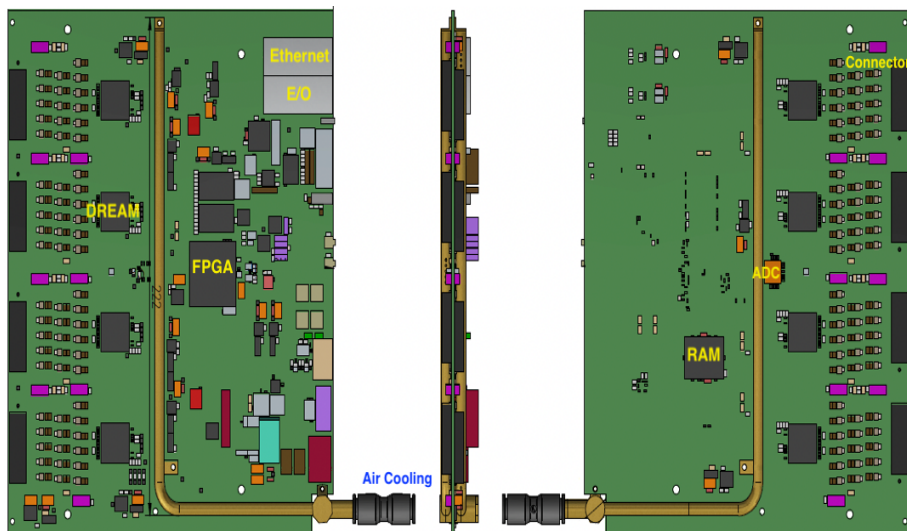


FIG. 29: Block diagram of a Front End Unit (FEU) boards with four DREAMs in each side of PCB board.

The FEU is responsible for the configuration and the readout of the DREAMs and the ADC, and for the pedestal equalization, coherent noise subtraction and zero suppression. The FEU forms the events from the data of the input channels and transmits

to the acquisition back-end. The FEUs can be operated in the residual magnetic field of up to 1.5 T of the solenoid in Hall B without any noticeable change of their power consumption or functionality. However, continuously flow of air is necessary to keep an ambient temperature within the crates.

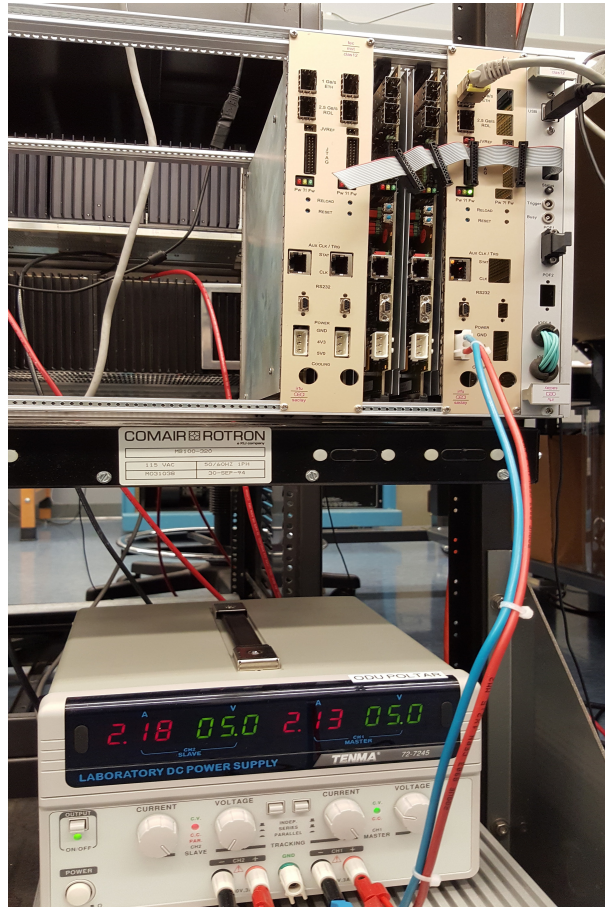


FIG. 30: Back pannel of 6 FEUs with the 5 V DC power supply to a FEU at ODU testbench. Ethernet link is connected to transfer data in this Standalone test.

- (f) **Data flow and performance:** Data from the detector readout padboard were directly fed to the FEUs using adapter boards and MEC8 cables. Trigger were provided to FEU

either using self triggering option of FEU or externally generated TTL signal fed to the back panel of FEU crate. After receiving the trigger signal, the FPGA reads corresponding data samples from the DREAMs and follows the data processing steps: first, the pedestals are equalized after serial-to-parallel conversion; second, for each sample, the coherent noise affecting the DREAM inputs is estimated and subtracted on per chip basis; and last, zero suppression on per channel basis is performed [31]. The FPGA forms an event fragment from the retained channel data and sends it to the acquisition back end using an ethernet/optical link as shown in Fig. 31. The link is also used to configure and control the run parameters of the FEUs.

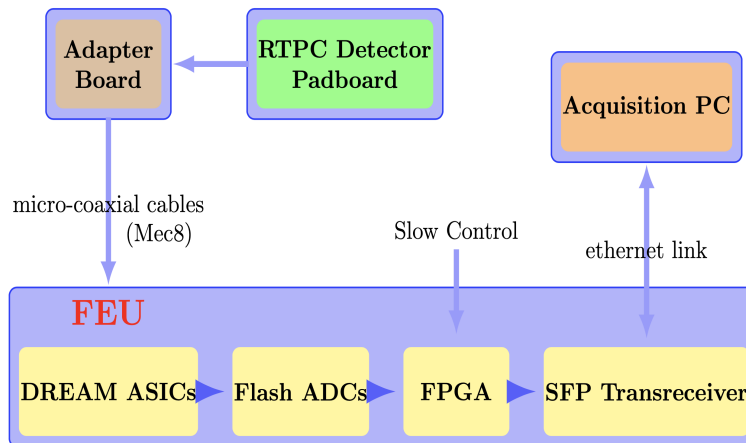


FIG. 31: Standalone data acquisition of the RTPC using FEU at ODU testbench.

Specific software from the SACLAY group is used in a Linux environment to configure and operate the FEUs at ODU. A configuration file and different Linux console commands (see Appendix C) are utilized to acquire data of the RTPC prototype. The raw data from the FEU are converted to the readable text file format for further analysis. The testbench at ODU was important to validate the compatibility of the FEU with the RTPC detector, investigate various components of the detector (HV, adapter board,

drift gas mixture), and optimize the performance and stability of the RTPC detector system. In addition to the successful hardware work during the change of HV supply system and gaseous supply system mentioned above, the data analysis was started with the pedestal analysis of the FEU. Pedestal of a FEU is taken using Linux commands and analyzed using ROOT.

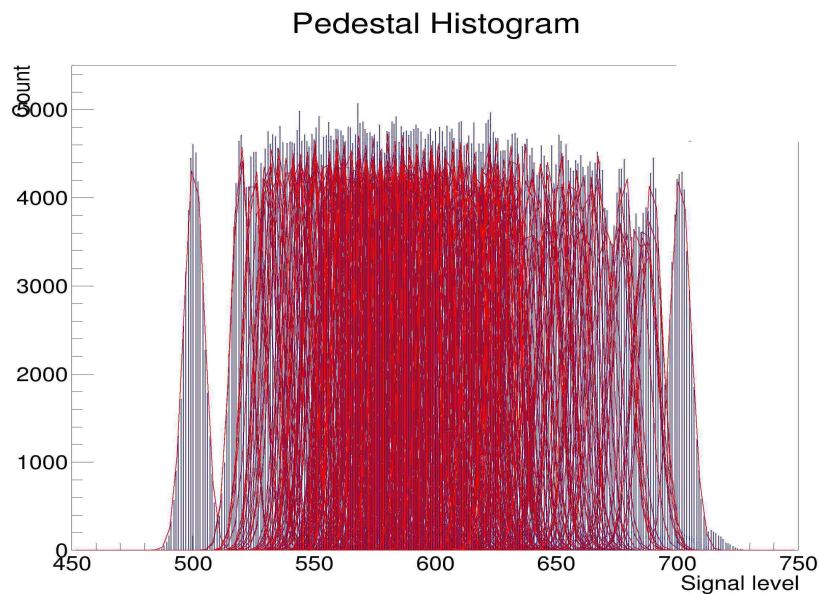


FIG. 32: Pedestal data of all 512 channels of a FEU with individual channel pedestal fitted with the Gaussian function.

Histograms of the pedestal data from each of the 512 channels of all eight DREAM chips in a FEU are plotted and each channel is fitted with a Gaussian function. The super-imposed histograms of all the 512 channels is as shown in Fig. 32. This shows pedestals of the channels range from 490 to 720 ADC units, and most of the channel's pedestals superimpose with each other.

The mean and standard deviation of the Gaussian fit are extracted and plotted against

the channel number as shown in Fig. 33. It is clearly seen that there are eight distinct 'U' shaped patterns of average pedestal value and the noise. If we look from details, the mean value starts to decrease at first, reaches the minimum and again starts to increase. This process occurs after every 64 channels. This indicates that every 64 channel, corresponding to a DREAM chip, are interlinked because of the capacitance and common mode effect. This analysis shows that the average pedestal has a maximum of 700 ADC units and minimum of 500 ADC units. From the standard deviation plot, it is confirmed that the noise of the channels ranges from ~ 3.9 to ~ 5.5 ADC units.

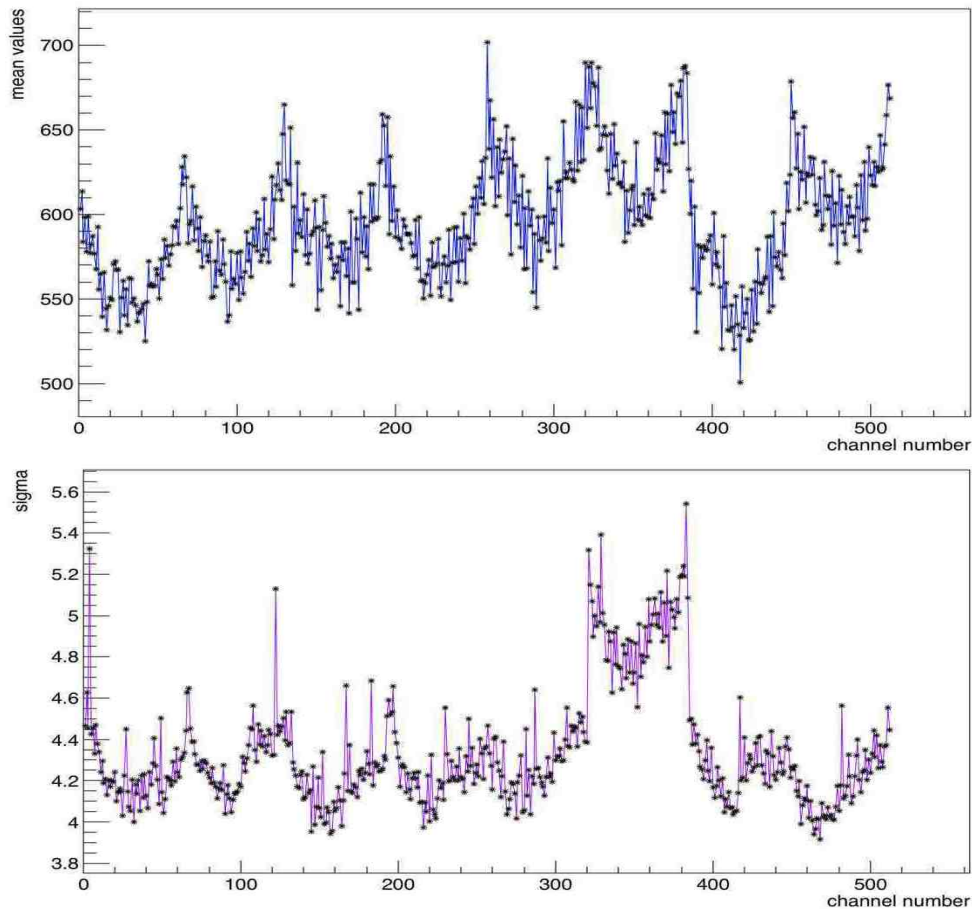


FIG. 33: Mean pedestals (top) and the noise (bottom) of all 512 channels of a FEU plotted against channel number.

3.3 OBSERVATION AT THE ODU TESTBENCH

By analyzing the pedestals with and without the ribbon MEC8 cable connected to the FEU, we saw that it gave a quite good picture of how the noise changes by adding the readout components without any pedestal fluctuation. For example, Fig. 34 clearly shows the pedestal remains almost unchanged, but the noise changes significantly after connecting the FEU to the prototype detector. Among the six clusters for each DREAM of a FEU, only two DREAM were connected to the detector, so the noise only in third and sixth DREAM chips are elevated. The change in these two DREAM chips is also not the same from the plot, it is due to the fact that two different types of cables (one from Hitachi and the other from SAMTEC) were used to connect the detector with the two DREAMs.

While trying to find a better way to check the continuity and connectivity of the RTPC readout components (Padboard to the FEU), we performed further studies on the pedestal noise analysis. As DREAM chips have different programmable gain capacitance (see Appendix C), we changed the capacitance to see how distinctly we could visualize the noise difference and determine which component might have an issue. Appendix A shows that with the maximum available capacitance of 600 fC, it is hard to see the detail. However, lowering the capacitance made it possible to compare each component separately. So, even if we choose higher gain capacitance (lower amplification and corresponding noise) during the data taking, we decided to use higher capacitance to test our readout electronics.

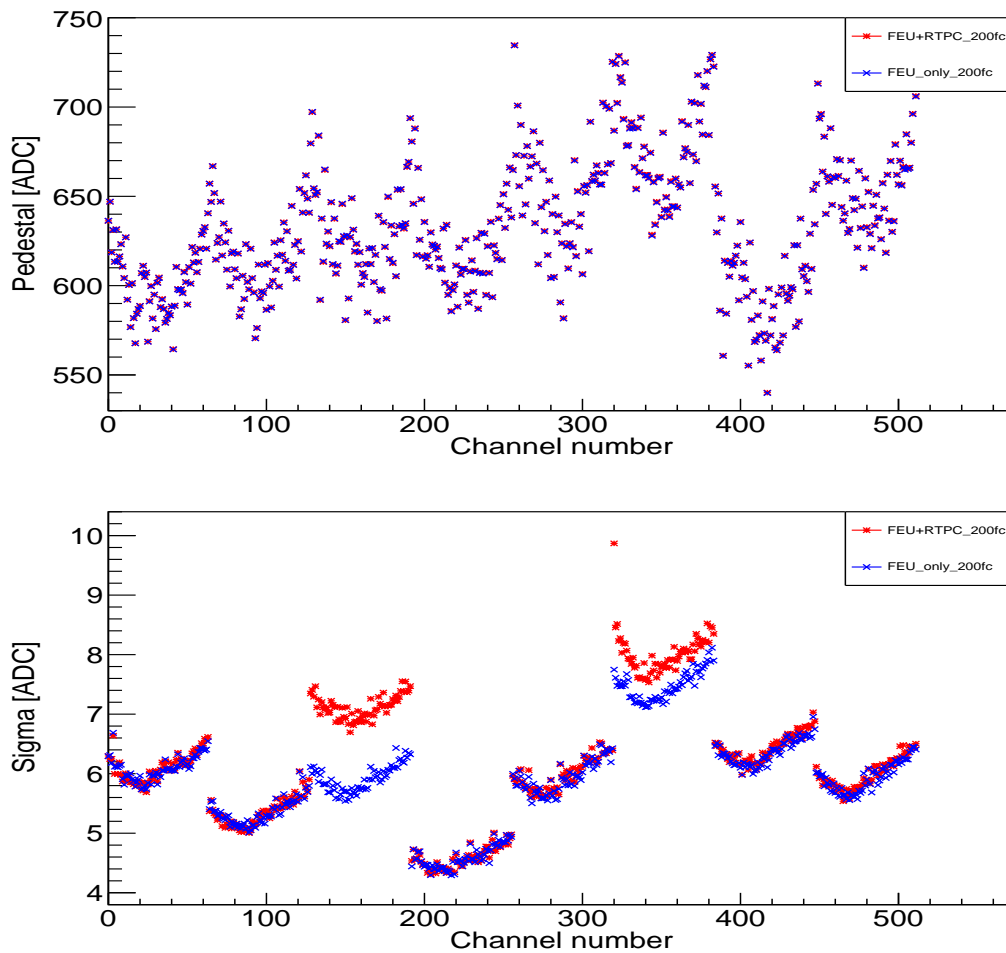


FIG. 34: Comparison of mean pedestals (top) and the noise (bottom) of all channels with 2 MEC8 cables connecting to the DREAM three and six of a FEU.

We also tested the new prototype adapter board to find out its quality. Fig. 35 shows the pedestal noise observed with different configurations. The noise increased smoothly afterwards in all channels (channels corresponding to three DREAMs) when a cable was connected, but observed some spiky channels when adapter boards were connected even if the overall noise level was increased above 10 ADC units. Connecting the padboard did not show much difference as the resolution was lowered by the spiky channels. Those spiky channels were mapped out in the data file and investigated further with other electronic equipment. We found that those channels had issues from manufacturing. We noticed most

of the time that those spikes were the result of two channels somehow connected with each other (or misconnected). Based on the findings, we sent feedback to the corresponding manufacturer to also investigate and improve the product. When the noise was smooth, we could also determine electrical discontinuity in any channel.

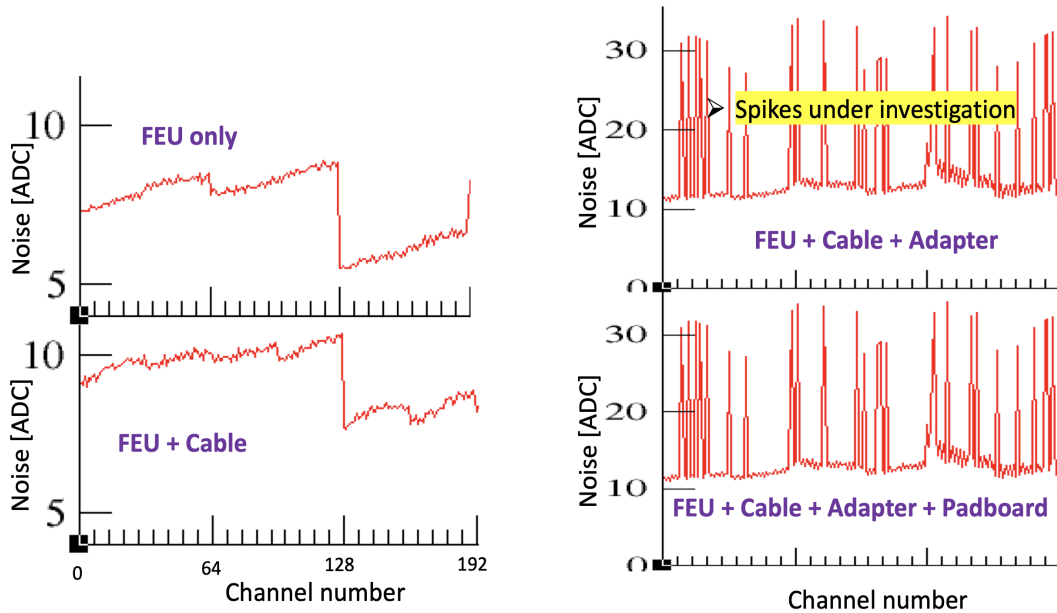


FIG. 35: Study of the variation of pedestal noise to check the connectivity of the DAQ electronics with the prototype adapter board.

After setting up everything at the ODU testbench (prototype detector, HV supply, gas mixing chamber and flow controllers), the prototype was flushed with pre-mixed ArCO_2 for about 4 hrs. A HV test with new CAEN power supply was performed using the GECO2020 HV supply control software. The GEM biasing voltage was gradually increased from 300 V keeping 2000 V across the drift region of 3 cm until we got a clear signal in the oscilloscope from the detector with a Sr-90 source as well as random cosmic radiation as shown in Fig. 36. The Sr-90 source was kept inside the prototype using a long stick to make sure that we could easily observe its beta decay. For ArCO_2 , the signal is observed with a 365 V biasing voltage

across each GEM foil. After successfully observing the signal in the oscilloscope, we decided to use the DREAM based FEU to readout these signals from the detector.

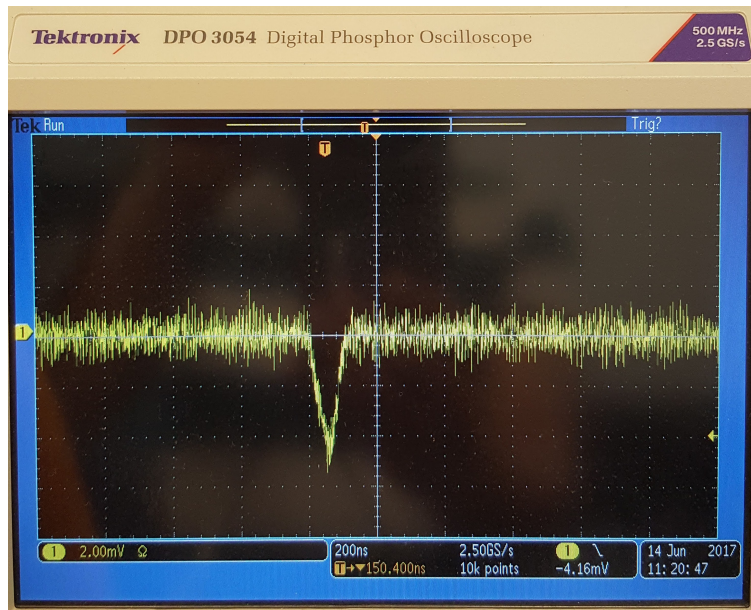


FIG. 36: A scope used to observe the signal from the prototype with HeCO_2 as drift gas.

To readout signals using the FEU, we needed a trigger setup and at the beginning we used the self triggering feature of the DREAM. With self triggering, the FEU readout allotted number of samples with a pre-defined latency if the FEU sees any signal samples above a certain threshold. We took data following the commands (as mentioned in Appendix C), and a typical signal is shown in Fig. 37. The signal from the DREAM was better fitted with the split-normal distribution function (Equation 22) as shown in the right top of the signal. At the beginning we took a small event size of about $2 \mu\text{s}$ and later increased to the maximum limit of about $12 \mu\text{s}$ with 48 ns sample bins. As BONuS12 required to have a large event size of about $8 \mu\text{s}$, we wanted to test the capability and stability of the electronics for a large time window size. The analysis of the large window also helped to understand the processes within our detector better. Towards the end of our testing, we changed the configuration to

have 40 ns sample bin size. We used a feature of the DREAM to readout only every third sample, so the time resolution would be 120 ns.

$$f(x) = [0] + [2] * \exp\left(\frac{-(x - [1])^2}{2((x < [1]) * [3] + (x \geq [1]) * [4])^2}\right) \frac{1}{(0.5 * ([3] + [4])\sqrt{2\pi})} \quad (22)$$

where [0], [1], [2], [3] and [4] are parameters corresponding to baseline, peak value, normalization constant, sigma of left and right curve respectively.

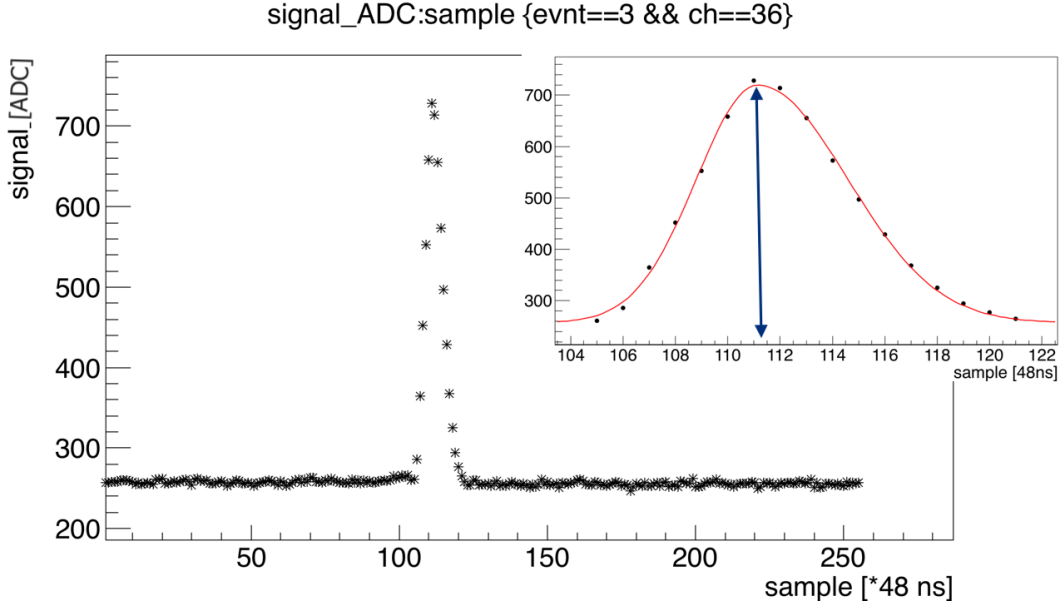


FIG. 37: Typical signal of the prototype detector obtained by the DREAM based DAQ over a large time window and the zoomed view of signal fitting using split-normal distribution function with different rising and falling rate.

An external trigger was set up using cosmic rays as shown in Fig. 38 with two scintillators, one on top of the detector and another, smaller detector inserted into the central bore of the detector. The coincidence signal from both scintillation counters were converted to NIM signals using a discriminator, which then passed through an ‘AND’ gate to form the

coincidence. The signal from the gate was then converted to TTL using a NIM to TTL module. This TTL signal was fed to the back panel of FEU crate (shown in right side of Fig. 30) with a LEMO connector.

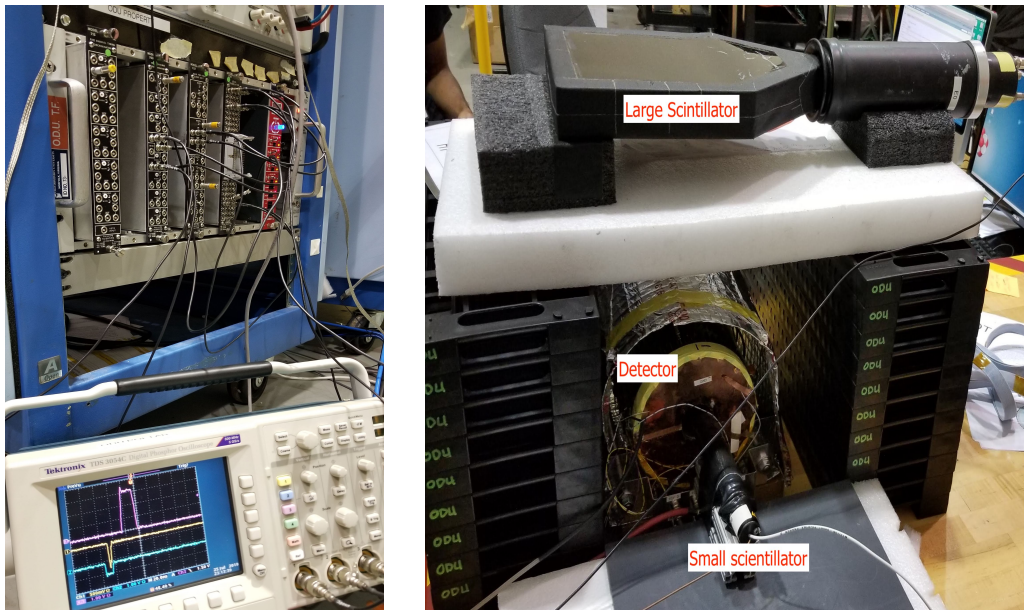


FIG. 38: Cosmic setup with two scintillators (one on top and another at center of the detector) for the coincidence trigger.

With the standalone DAQ running at the ODU testbench and mostly compatible with our detector, we tested different proportions of He:CO₂ gas mixtures as drift gas. As a first impression, we found smaller and less signals with a 70:30 proportion of He:CO₂ which was promising based on the simulation [30] of drift angle, drift time and the diffusion. So we used the mixing chamber (as shown in Fig. 26) to mix the different volumetric proportion of He:CO₂ instead of using premixed bottles. We collected more than 5000 events with the external cosmic trigger. All the events were taken with the same HV setting and flow rate to the RTPC. Figure 39 shows our observations, concluding that a sharp decline of observing a signal from cosmic radiation appears if the CO₂ proportion is increased. We

tested five different mixtures of He:CO₂ 90:10, 80:20, 75:25, 70:30 and 60:40, among which only about 0.4% of cosmic ionization produced detectable signal in the detector readout in the 70:30 mixture, whereas 15.8% of similar events produced a detectable signal in the 90:10 gas mixture. Within the accuracy of the mixing proportions, it proved that large fractions of CO₂ suppress ionization electrons to reach the readout plane. The higher recombination rate of CO₂ could be a major cause of this sharp decrease in detection of ionization events inside the detector. However, keeping also in mind the gas study mentioned above, we decided to use the 80:20 mixture in our experiment noting that protons, not cosmic rays, would be the ionizing particle in the final experiment. The energy loss of low-momentum protons in the drift gas is much higher than that of minimum ionizing particles.

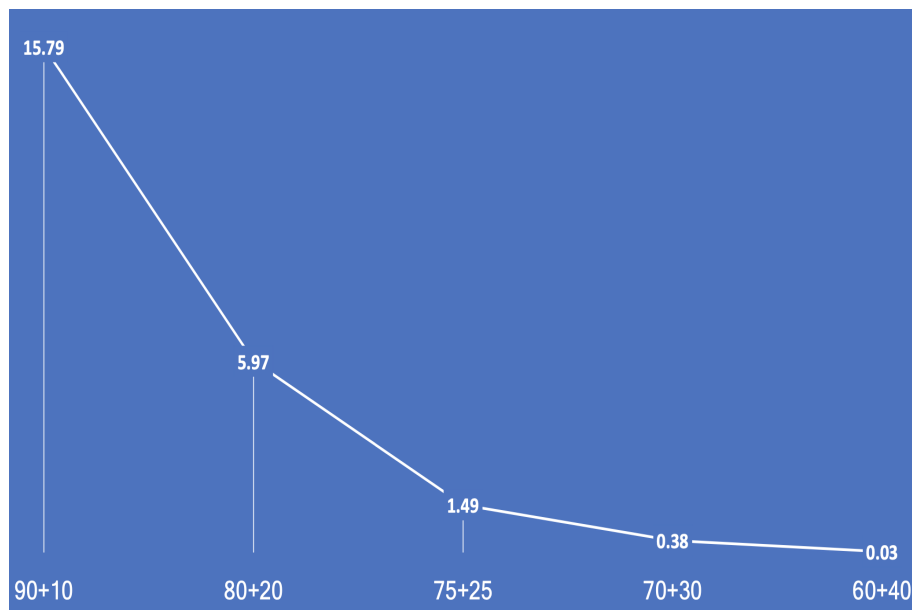


FIG. 39: Analysis of signals from the various proportion of gas mixtures of Helium and Carbon-dioxide. Probability is obtained with respect to the number of triggers (or events) processed. X-axis shows the gas mixtures and Y-axis the percentage of signals observed in the collected events.

After deciding on a gas mixture of 80:20, premixed gas bottle of He:CO₂ were ordered and used for the rest of the experiment. We already had 90:10 Ar:CO₂ for preliminary testing, so we used both gases to calculate the drift time of our detector with the drift field of ~ 2300 V across the 3 cm region. To calculate the drift time, we used the external trigger and collected 250 samples per event with sampling time of 48 ns. We also used the trigger latency option of the FEU (see details in Appendix C) to readout 100 samples prior to the trigger arrival. Each signal was fitted with a double-Gaussian function (see Fig. 37) and the time (x axis value) corresponding to the signal peak was extracted and plotted as shown in Fig. 40. In this plot we can clearly see our choice of trigger latency with a peak starting around sample 100 along the x -axis. This distribution clearly shows the specific time period over a long window in which signals from the detector are available to the readout, providing the maximum and minimum time limit. This difference in the readout limits is equivalent to the drift time. From these two plots, we found the drift time $18 \times 48 = 864$ ns being much shorter in ArCO₂ than $48 \times 48 = 2304$ ns in HeCO₂ in the prototype. We compared these result with the simulated predictions, which are in agreement within 10% uncertainty. This uncertainty could be due to lack of measuring the exact potential at the cathode and first GEM (GEM1), as well as some potential drop across the current limiting resistor which made drift field slightly different from the calculated value using supply voltage.

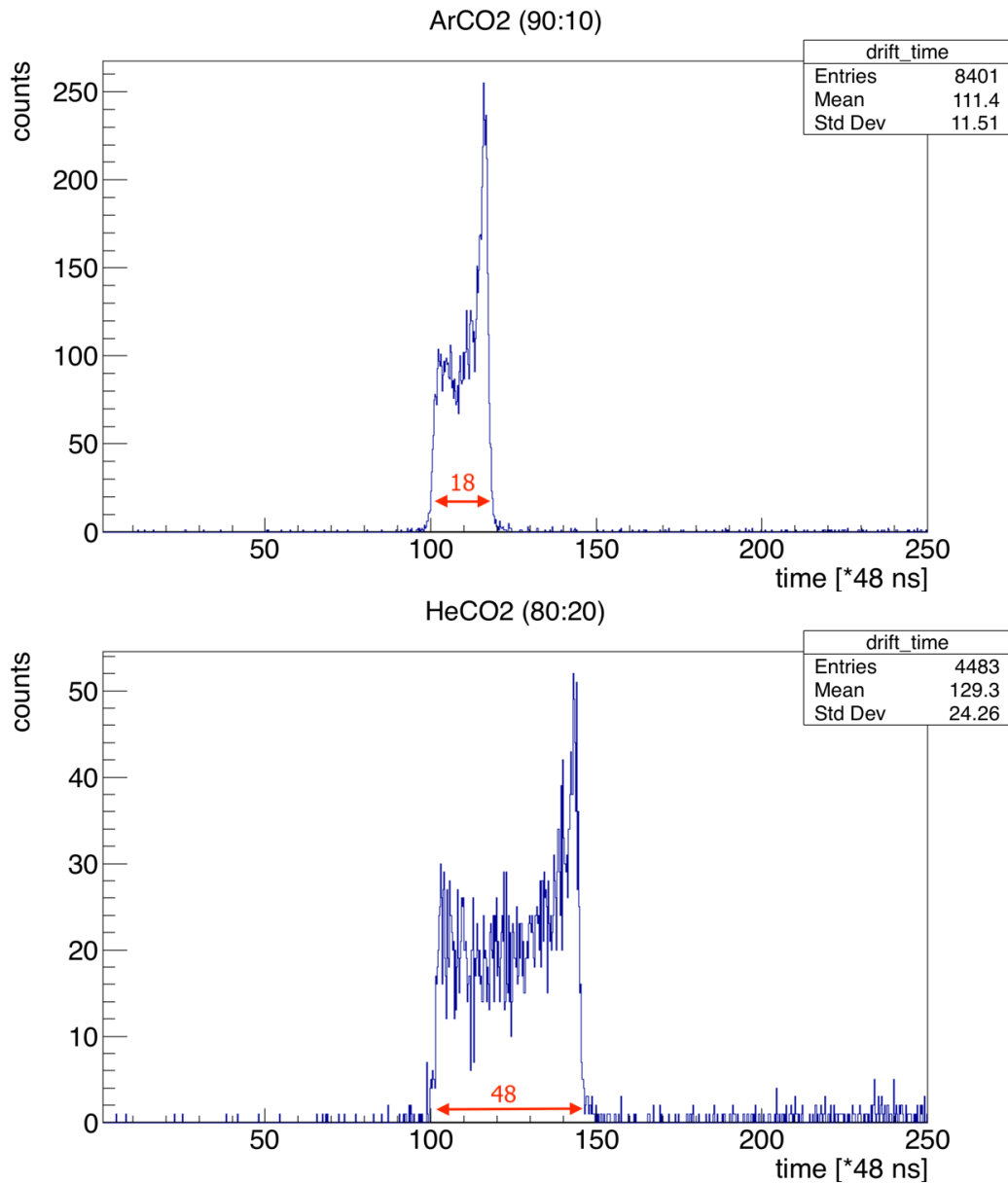


FIG. 40: Calculation of drift time of the prototype using DREAM data for two gas mixtures, ArCO₂ and HeCO₂ at the potential difference of ~ 2300 V across the drift region of 3 cm.

While using the 200 fC gain capacitance of the DREAM, signals read out from the FEU were noisy and many signals were saturated as well. So we changed to the next available

gain capacitor of 600 fC (max value). It is important to compare the average signal height of the FEU collected signals. With similar gas and HV configuration of HeCO₂ as above, except the decreased event window to 50 samples, we collected more events and plotted the distribution of the peak ADC value of all the signals as shown in Fig. 41. The distribution shows that signals peak ranged from 700 to 2800 ADCs, and the maximum number of signals have peak about 1000 ADC. The highest possible output of the FEU could be 4095 ADC, because of the 12 bit ADC hosted in it. No saturation was observed in this data set with the gain capacitance of 600 fC, which was increased from 200 fC after observing saturated ADC events. All these analyses were performed without pedestal equalization.

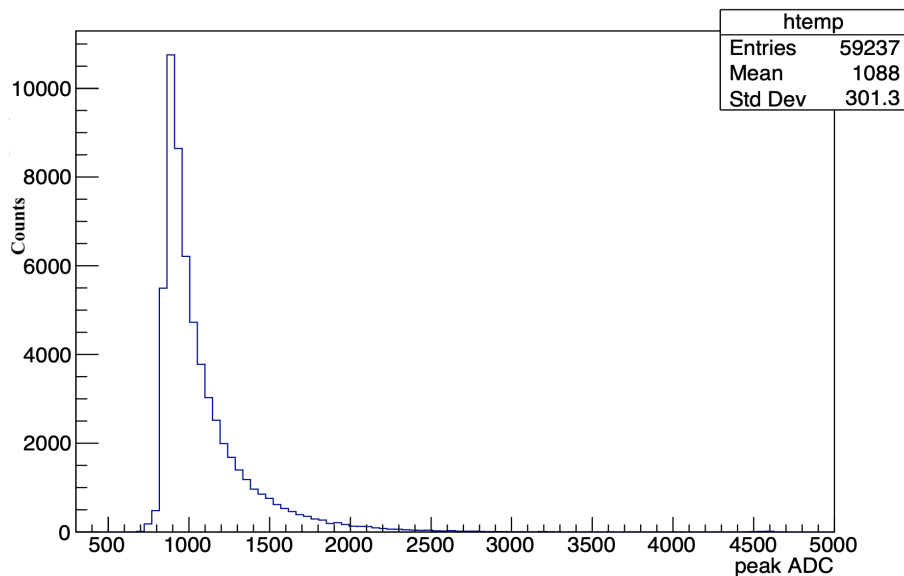


FIG. 41: Distribution of the peak ADCs of the observed signals for HeCO₂ gas observed from DREAM electronics.

3.4 TARGET STRAW TESTING AT ODU

The BONuS12 experiment used a high pressure deuterium target for the $d(e, e'p)X$

interaction. The dimension of the target tube was 6 mm diameter with a length of more than 40 cm. The target was made up of thin polyimide/Kapton film (few microns) to confine the deuterium, helium as well as hydrogen gas.

3.4.1 TARGET TUBE: POLYIMIDE STRAW

Various types of polyimide straws manufactured by different companies were tested to check the bursting limit, leakage rate and the straightness over length. Effectiveness of the polyimide straws were tested in our lab using non-flammable nitrogen as well as helium gas.

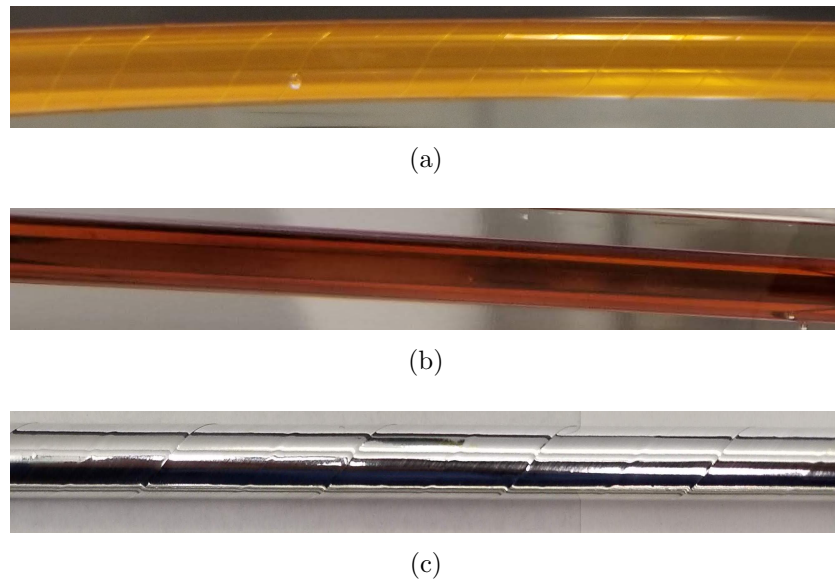


FIG. 42: Different Target straws (a) Spiral wound Kapton tube (b) Seamless Kapton tube from American Durafilm (c) Aluminized polyimide tube from Paramount Tubing.

Four different types of tubes were tested to choose the best suited for BONuS12. The first type was a spirally wound Kapton tube as shown in Fig. 42a, in which two thin Kapton foils, overlapping halfway in its breadth, were spirally wound with a fixed angle to make tubes. These tubes were manufactured in China and have a length of 50 cm and diameter

of 6 mm.

The second type was a Kapton straw from American Durafilm which are not spiral wound. This tube is made from a single foil fused along its length.

Third type was prepared by coating 0.1 - 0.5 microns of various compound in the second type of the straw. We obtained aluminum and other oxide coated straws from Orsay in France and Argonne National Laboratory.

The fourth was a straw from Paramount Tube, a leading company to produce custom tubes under Precision Products Group Inc., which manufactured polyimide straws on our request using a one side aluminized polyimide film. The polyimide (Kapton) film sputtered with aluminum was ordered from Caplinq and sent to Paramount Tube to prepare straws. Two thin films were spirally wounded to form a straw in which the non-aluminized sides of the film were glued together and the aluminized layers were both inside and outside of the final straw. We could clearly see the spiral lines of overlapping foils in the straws which can be seen in Fig. 42c. These straws had 50 cm length and 6 mm diameter.

3.4.2 TARGET LEAK TEST

To test the tubes, one end of it was completely closed by a metallic piece (iron/aluminum) with the help of glue and the other end glued to a metallic tube. The metallic tube was connected to the gas supply system. At the beginning, the inward fitting of the polyimide tube was glued, while later the outward fitting. 3M Scotch-Weld (DP 190) and Loctile EA 1C epoxies were used to glue the polyimide tubes to the metal. The first has longer cure time than the later one. After the glue dried, the straw was fitted with a pressure gauge and a gas stopper to evaluate the gas leakage from the straw. This set-up was then connected to a gas supply bottle along with a gas regulator and another pressure gauge. The overall set up to test the polyimide straw is shown in Fig. 43. In this setup, the transparent vessel around the polyimide straw with top side open was used to test the straw under water. This set-up helps to visually inspect from which point of the straw the gas is leaking. In every set-up, we wanted to be sure that the leakage was not from the fittings. During the test nitrogen as well as helium gas was used, because both of them are non-flammable, and the helium has a comparable molecular weight as deuterium.

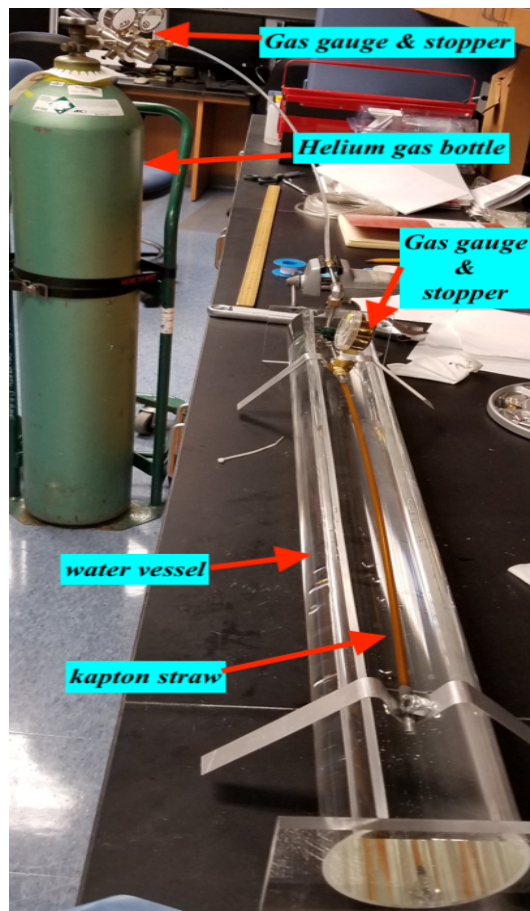


FIG. 43: Set-up to test the polyimide straw gas leaking.

The first test was to see how much pressure the straw could withstand. We used nitrogen gas to pressurize the straw and found the bursting limit. The leakage rate of nitrogen from polyimide is very much less than helium, so the straw could be under high pressure for a longer time. In this process, the pressure was slowly increased from 60 psig to 150 psig by 5 - 10 psig per half an hour. After the first trial with bursting straw the process was repeated by increasing only 5 psi/day or less towards the bursting limit. The second test was to find the actual leakage rate of the polyimide straw. In this process, nitrogen gas was used first and then helium gas in the straw at a pressure of 80 to 120 psig based on the type of straw. In addition to the leakage rate, also the leakage region of the straw was observed by dipping the straw under water. The last test was to keep the straw at a constant pressure of about

90 psig and find out how long the straw could withstand that pressure.

3.4.3 TARGET TESTBENCH OBSERVATIONS

The thickness of the straw was measured using a micrometer and the diameter using a vernier caliper as shown in Fig. 44. The straightness of the straw was confirmed by comparing with a straight iron rod over a graph paper as shown in Fig. 45. We also used a high zoomed camera attached to the optical bench to measure the deviation of the straw compared to the rod.

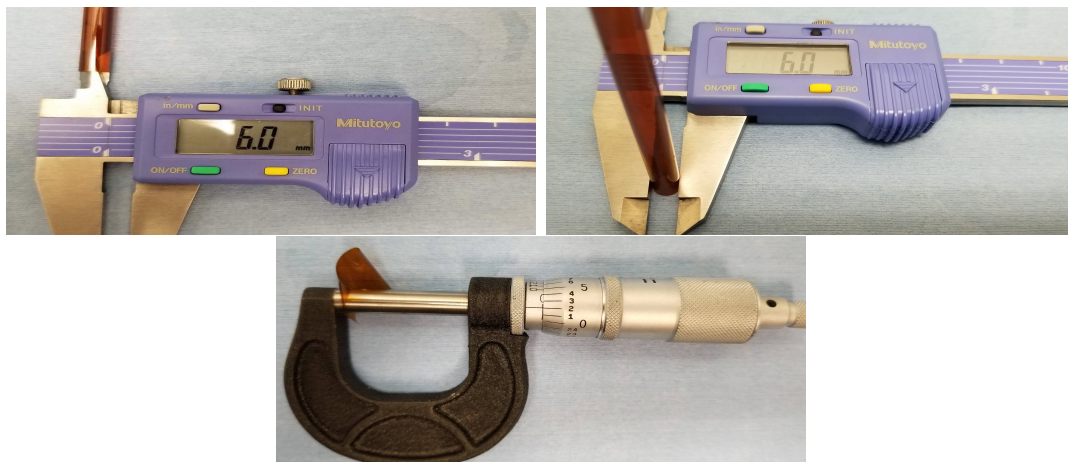


FIG. 44: Measurement of the straw diameter using vernier caliper(top) and wall thickness by micrometer (bottom).

- a. First type (Fig. 42a): After the initial test, the first type of straw was rejected. The first type of straw sent as $50 \mu\text{m}$ and the package also mentioned the same, but its wall thickness was actually $96 \mu\text{m}$. Because of its thick wall, the leakage rate was lower and bursting limit was higher.



FIG. 45: Evaluation of the straightness of the straw comparing with a straight stainless steel rod over a graph paper of 0.05 cm resolution.

- b. Second type (Fig. 42b): The second type had wall thickness of $50\ \mu\text{m}$, except $54\ \mu\text{m}$ along a line of fusion. Fifty centimeter long these Kapton straws were not perfectly straight. They seem to be curved a little, both in the pressurized state and without any pressure. Some straws were found to deviate less than 1 mm from straightness over their length. So, these could be used in the experiments. Using appropriate tension at the end could also achieve the straightness. Stretching as well as applying a small shear stress at the end of the straw could make it almost straight.

In the first test, the Kapton straw (from Fig. 42b) burst at about 165 - 170 psig. When keeping two other straws of this type at 160 psig nitrogen gas pressure for more than three weeks, the straws were still good and the leakage rate was about the same after this time.

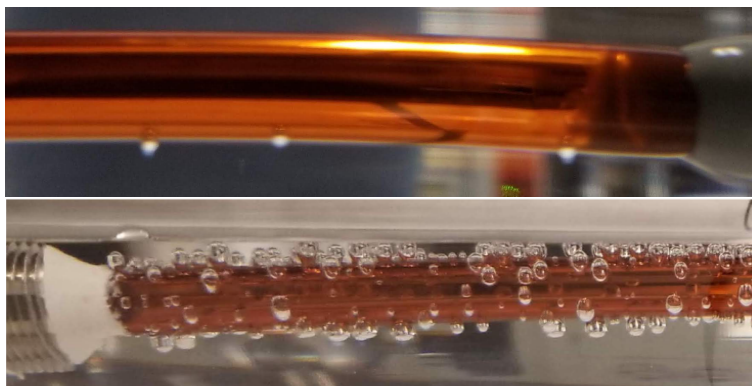


FIG. 46: Leakage of Helium from Kapton straw visualized as bubble under water.

The leakage rate for the nitrogen gas was about 1 psi/day at a pressure of 100 - 120 psig from the Kapton straws of 50 μm wall thickness. Helium leaks at a faster rate from the straws at about 4 - 6 psi/hr at a pressure of 100 - 120 psig in the similar straws of 50 μm wall thickness. The larger leakage rate could easily be seen by the large amount of larger bubbles inside the water as shown in Fig. 46.

- c. Third type: While testing the aluminum coated straws from Orsay, the coating came off within an hour when dipped inside water which is shown in Fig. 47. In addition, when another similar straw was left in air for a week in the lab, the coating started to come off the Kapton. The coating was not suitable.

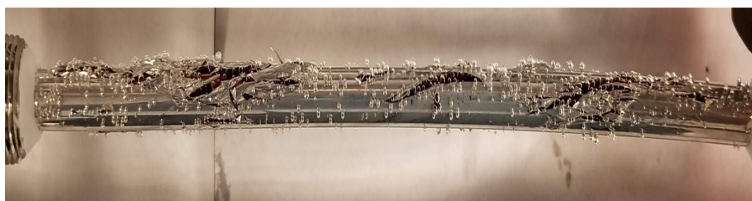


FIG. 47: Aluminum coated kapton straw under water showing the damaging of coating after a short time.

Results for the aluminum-oxide coating from Argonne were different. The coating did not come off, but there was almost no difference in the leakage rate compared to a straw without coating. It appeared that the thickness of the coating was not sufficient, and the thickness of the coating needed to be increased.

- d. Fourth type (Fig. 42c): These straws were 50 cm long with diameter of 6 mm. The wall thickness of the straw was 63 microns and they looked perfectly straight.



FIG. 48: Leakage of Helium from the double sided aluminum coated straw visualized as bubble under water.

The first straw under test did not burst within an hour until a pressure of 120 psig was reached. This straw was left overnight at 100 psig, and it was holding pressure all the time. This test was done using nitrogen gas.

The leakage test performed using helium gas showed leakage at a rate of about 1.5 psi/hr from the straw at a pressure of 80 - 95 psig. The leakage could be easily seen by a large amount of gas bubbles when dipped under water as shown in Fig. 48.

3.5 THE BONUS12 RTPC AND THE TESTBENCH AT JLAB

The Jefferson Lab (JLab) electron beam energy was upgraded to 12 GeV in 2014 and at the same time, the Hall B CLAS detector was also upgraded to CLAS12. Along with these upgrades, the BONuS experimental group also proposed to extend the BONuS experimental program to extract observable closer to $x \rightarrow 1$ upgrading the RTPC by increasing the θ and ϕ acceptance as well as the resolution of the detector. The spectator protons could be effectively tracked in the new RTPC over a large volume with almost no dead region in ϕ . In addition, the group proposed to use a DAQ system based on a Dead-timeless Readout Electronics ASIC for Micromegas (DREAM) chip to read out the signals from the detector in run group F (BONuS12).

Establishing a testbench at Jefferson Lab's EEL building was crucial to the experiment to perform final tests of our RTPC detector and its various components, including the gas system, data acquisition system and other slow controls which could be easily transferred to the hall. Some of the systems that we tested are summarized below:

- (i) **New gas panel and its control** : A new gas panel as shown in Fig. 49 (see details

in Appendix B) was constructed and tested thoroughly for BONuS12. The gas panel consisted of 3 input lines (1/4" tube) and 3 exhaust lines (1/2" tube), each line dedicated to the RTPC drift gas, buffer gas, and the target gas, respectively. The drift gas line had a manual valve, 500 sccm Mass Flow Controller (MFC), pressure gauge meters and a relief bubbler in the inlet line, while the outlet line had a pressure gauge and two bubblers (normal operation bubbler for the detector and relief bubbler) with an additional bypass area for the Drift gas Monitoring System (DMS) [30]. The RTPC had another gas line also in between inlet and outlet, a pressure sensing line, to observe the absolute pressure of the detector which had a pressure gauge, absolute pressure sensor, and differential pressure sensor with respect to the DMS. These sensors were connected to a Raspberry Pi system for the readout, which was monitored continuously from a desktop computer. Next line was the buffer line which had an electronic valve, a flowmeter, a pressure gauge, and a relief bubbler along the inlet, and a bubbler in the outlet line which was connected together with the RTPC exhaust line going out of the hall. It also had a differential pressure sensor connected with respect to the RTPC outlet.



FIG. 49: BONuS12 gas panel with various sensors and safety components approved by the Hall B engineering (right); and control and monitoring of the drift gas (left).

Even if we used non-flammable pre-mixed gas (HeCO_2) in the RTPC detector, the panel also had the target line which was used to flow both hydrogen and deuterium gases. There was only one line connected to the BONuS12 pressurized target in the final experimental setup, so the exhaust line came out of the inlet at the nearest possible distance from the target position. The filling process of the target was therefore done in a couple of cycles to keep the target less contaminated by the residual gases.

- (ii) **HV supply and slow control** The CAEN supply used for the RTPC operation could not provide the full high voltage to the cathode (~ 6.5 kV), hence, an alternative supply was required. The BONuS12 group decided to use a Wiener power supply (Fig. 50) consisting of a crate with MpodC CPU, and two HV modules. Both modules supplied -ve polarity voltage as required for the RTPC, with the EHS 4080n module (each channel voltage limit 8 kV and current limit 1 mA) supplying HV to the cathode and EHS 8030n module (each channel voltage limit 3 kV and current limit 3 mA) supplying HV to all the GEMs layers.



FIG. 50: Wiener MpodC crate with two HV modules for BONuS12 RTPC power supply.

The CAEN supply we had been using before had the built-in feature of actual biasing voltages across every region. This feature made it possible to tune every GEM region independently without modifying another channel and also protected the individual GEMs from over-biasing. It could be operated in ‘GEM’ mode as well, which would made the detector safe by turning ON/OFF the whole detector simultaneously, preventing reverse-field configurations and any over-current within the detector. The Wiener supply did not have this feature and, hence, the voltage control had to be done more careful. To protect our detector from over-biasing and reverse-field, we chose to add more options and safeguards in the external EPICS control software. The EPICS GUI for the HV control of this new power supply is as shown in Fig. 51. In addition to the ON/OFF option for individual channels, it also accompanied all ON (all OFF) options with programmable delay settings to the channels to make sure that no adverse effect arise. It also incorporated an interlock between two channels to protect individual GEMs from over-biasing. Voltage and current limit for each channel could be set directly from the interface by setting new values.

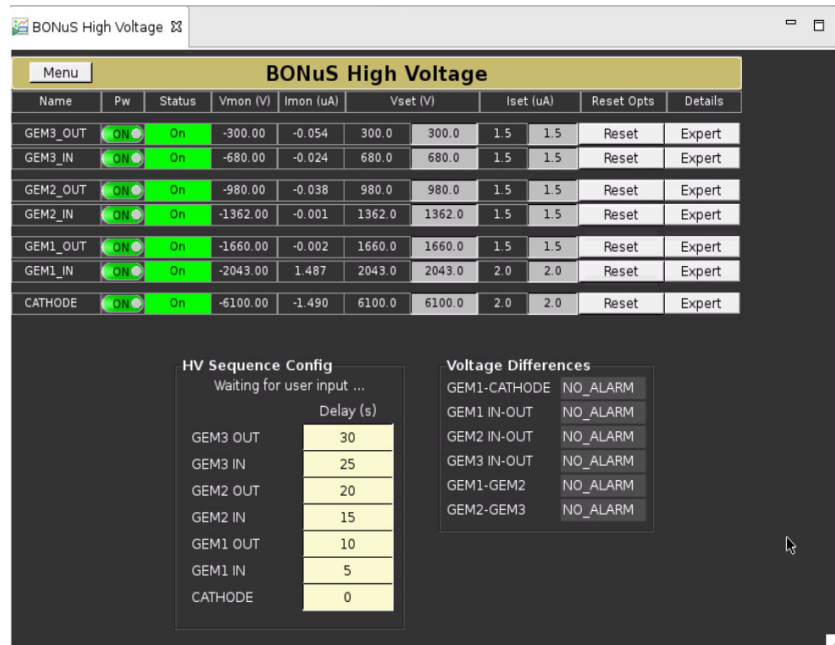


FIG. 51: RTPC HV control Interface in EPICS programmable delay setting to ramp up the HV on all channels.

(iii) **New BONuS12 RTPC detector and adapter boards:** As discussed earlier (see section 3.1), a new RTPC detector was built by the BONuS12 group, which needed to be tested. During the testing of the first RTPC, BONuS12 group also started to construct two additional similar RTPCs as backups. Various tests performed with the first RTPC guided us to modify several components and mechanism for improving the second and third RTPC under construction. The first RTPC test at the JLab testbench was a leak test. As we saw no bubbling from the 1/10" of wc bubbler upto the 500 sccm flow of ArCO₂/HeCO₂, a leak test using 2% hydrogen gas and a flammable gas detector was carried out to find leakage areas in the detector. A major leakage was from the seam of the padboard, the upstream and downstream joints, and the ground foil. All the leakage areas were sealed with DP190 epoxy and leak tested again to see any difference. The remaining leakage from the the ground foil was mostly due to the diffusion of gas into the buffer region which was open at both ends until the target system was installed. So, in further testing of the RTPC, both ends were covered temporarily with end-caps. This leak testing process was followed thoroughly in the RTPC-2 and RTPC-3, but sealing was much improved compared to RTPC-1.



FIG. 52: BONuS12 RTPC and its installation on the CVT (Central Vertex Tracker) cart.

Two more tests were performed after the leakage test before the start of tests with cosmic rays using the new RTPC. One test was a GEM HV test in which individual GEM foils were tested with ~ 400 V biasing voltage across to determine its stability without a noticeable current flow. Even if individual GEM foils looked okay before assembly into RTPC-1, the built detector had issues with the outermost GEM. The GEM tab seemed to be touching the grounding part of the padboard. Because of this we could not establish the operating voltage in every region of RTPC-1. This issue was fixed by inserting an insulating Kapton foil between the padboard and the GEM3 tab. More Kapton foil had to be added to other parts in close vicinity with HV. As the RTPC was a hermetically sealed detector design, it was difficult to repair parts after assembly and, hence, additional insulation was added before assembling RTPC-2 and RTPC-3.

Even though RTPC-2 and RTPC-3 were improved in many aspects, RTPC-2 could not be biased properly. One of the GEM foils had a HV short circuit and the HV supply trace to this sector was cut. We had two ideas to locate the bad sector, (i) use a temporary shunt to maintain the biasing voltage in the GEM remaining sectors (11 out of 12 sectors) and take data to identify the low occupancy sector (ii) break the sealed HV pod out, test resistance across each sector and find the non-resistive sector. There were two HV pods that should be taken out to fully check the resistance of all the sectors, so we decided to use a shunt first and take data using a Sr-90 radioactive source with the standalone Front End electronics Unit (FEU) readout available for the test. We chose limited rows (3) of the RTPC at a time and used the self-triggering option while searching for the bad sector. We were sure that less or no triggers would be generated in the bad sector over a certain time period. We repeated the data taking in different rows by rotating the RTPC and found out the bad sector within a couple of hours. Looking at the RTPC design, we found the exact sector and the corresponding tab location to cut the trace out. Even though RTPC-2 had HV issues, RTPC-3 was in quite good shape except a small gas leakage as usual, which was sealed extensively at the testbench.

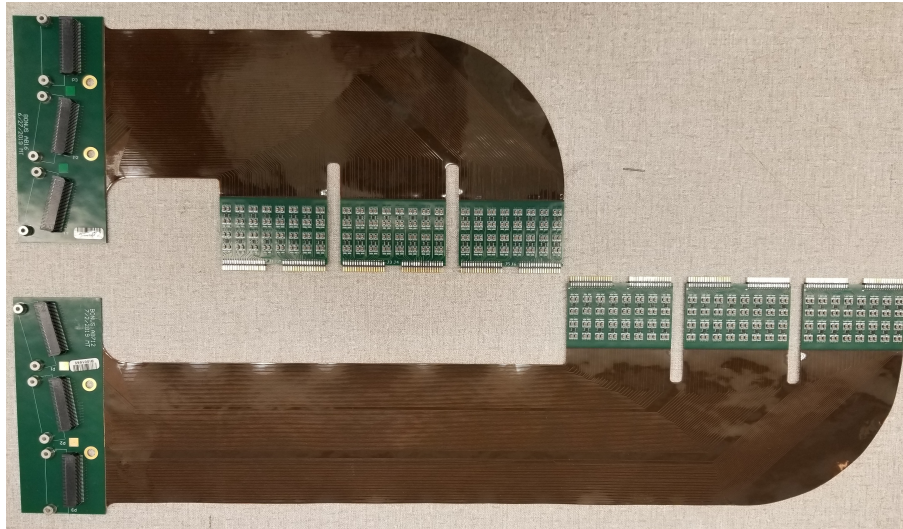


FIG. 53: Final version of two different size adapter boards to cover a complete row of connector in the BONuS12 RTPC.

The active region of the BONuS12 RTPC was 40 cm long and the charge signals were collected in a patterned padboard (as shown in Fig. 17), which were read out by two differently sized adapter boards (see Fig. 53). These two adapter boards covered a complete row of connectors in the RTPC which passed the signals to the FEU with three MEC8 cables connected to each board. There were total 45 rows of connectors in the RTPC, so we used 90 total padboards (45 long and 45 short) and 270 MEC8 cables to cover the RTPC fully.

- (iv) **Data Acquisition System (DAQ):** BONuS12 had the specific requirement to accommodate RTPC data within a large window size of $\sim 7 \mu\text{s}$ per event to reconstruct the proton track efficiently with high resolution. As we had observed at ODU, a normal signal size from the RTPC was $\sim 800 \text{ ns}$ (Fig. 37). It was decided to read one out of three 40 ns DREAM samples to reduce data size and still achieving the average time resolution of $\sim 120 \text{ ns}$. In addition to the sparse mode reading, the experiment also required the zero-suppression technique which allowed to timestamp and readout only those samples which were above the programmable threshold. The initial version of the firmware which checks first some samples of an event to have zero suppression

did not work for BONuS12 as the RTPC signals could be anywhere within a large window. This would allow to run the BONuS12 experiment well within the CLAS12 data flow collection rate, but would need to change the FEU firmware. With help from the SACLAY group from France new firmware as per RTPC readout requirement was prepared. It consisted of pedestal equalization, zero-suppression and sparse readout. The new zero-suppression algorithm checks every sample over a long window with programmed threshold and only reads out the sample above the predefined limit (could also readout up to 3 samples before and after along with it). This firmware required to be tested before implementing, so eight dedicated FEUs available at the EEL test area along with a Back-End Unit (BEU) crate was utilized with the upgraded firmware in a new BONuS12 RTPC.

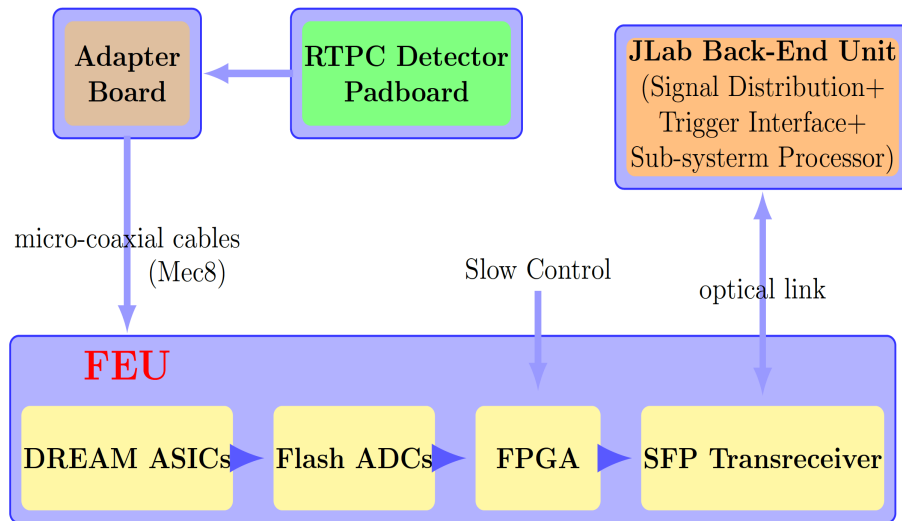


FIG. 54: Standalone data acquisition of the RTPC using FEU at ODU testbench.

The BEU (Fig. 55) of the RTPC data acquisition system consists of the Jefferson Lab standard VME/VXS crate with a crate controller single-board computer (SBC), a Trigger Interface (TI), a Signal Distribution (SD) and a Sub-system Processor (SSP)

module. The SBC runs the Readout Controller (ROC) application of the CEBAF Online Data Acquisition (CODA) framework. It completes the data integrity checks performed in the SSP firmware, disentangles multi-event buffers, forms RTPC events corresponding with the TI data, and sends them to the CLAS12 Event builder over a 10 GB/s Ethernet link. The TI accepts the low jitter 250 MHz system clock and trigger signals from the Trigger Supervisor (TS) and sends the status information of the readout system to the TS. The clock and trigger signals are delivered to the SD board over the VXS backplane. The SD board conveys properly delayed and aligned clock and trigger signals to the SSP boards. It also gathers their status information, and then combines and sends it to the TI board over the backplane. The SSP board was primarily designed to be a part of the trigger system at Jefferson Lab, but various inbuilt components made it acceptable for the fiber readout and front-end synchronization. The RTPC and MVT utilize the SSP in fiber readout mode. The SSP firmware has also been modified and implemented to fit the needs of the BEU as per BONuS12 Experiment. A single SSP can distribute the global system clock, trigger, and synchronous commands to up to 24 FEUs, and also acts as a bridge between custom front-end electronics and the VME based CODA readout. It collects event data through the fiber optic links and buffers events in its 4 GByte DDR2 memory. For each trigger, the SSP performs local event building tasks assembling FEU event fragments. The SSP time stamps the event with the synchronous 125 MHz clock and assign it the event counter value. The 48-bit time stamp along with the 60-bit event identification (ID) is used for local event building. This process implies gathering data packets from all FEUs belonging to the same event (matching time stamps, and event IDs). Multi-event buffers, with a programmable number of events, are constructed in the external DDR2 memory. Upon the request from the crate controller SBC, the contents of the buffers are transferred to its memory over the VME64 back-plane using dual edge Source Synchronous Transfer (2eSST) protocol. Transmission rates of 200 Mbyte/s are routinely achieved. The trigger pulses and fast run control commands are broadcast synchronously to all FEUs with a fixed latency over 2.5 Gbit/s links [31]. The trigger and the fast commands are delivered in a synchronous way with at least 1 ns precision [34].



FIG. 55: Components of the CLAS12 BEU consisting of SBC, TI, SSP, SD. Twisted cable with crimp connector are connected to the TI and SD front panel for standalone operation.

The TI has also front panel with ECL compatible header pins (see Fig. 55) for the input of external triggers in standalone test of the RTPC detector, instead of using the CLAS12 TS. The external trigger is delivered to the TI using a twisted pair cable having 2-pin crimp connectors at the ends during for the cosmic rays test at the test-bench and during the detector commissioning in the experimental hall . Similarly, the SD also has front panel header pins, which could be used for the trigger in/out in the self triggering mode with a fixed latency.

Jefferson Lab has a standard data acquisition system in the CEBAF Online Data Acquisition (CODA) framework [35] which is implemented in Hall-B as well, and was, hence, adopted for the testbench. Transitioning to this framework allowed us to use the existing CLAS12 monitoring software with some relevant changes for the BONuS12 setup. We also had data output in the standard CLAS12 format (EVIO file) enabling also testing of the decoding and reconstruction software.

- (v) **Cosmic Ray Test and RTPC Performance** Tests with cosmic rays at the EEL building was an important step to validate various components necessary to operate

the RTPC detector smoothly during the BONuS12 run in Hall B. Except the of the complete FEU system with all cables, most of the components necessary to operate the RTPC detector, along with the detector itself, was ready at the EEL building testbench. We had only six FEUs and equivalent cables at the EEL, so we decided to validate the functionality and performance of the detector using these limited resources as shown in Fig. 56. Six FEUs could accommodate data from eight rows of connectors (64° in ϕ) out of the total 45 rows. As a result, the adaptor board had to be moved about six times to completely test the performance of all the sixteen sectors. We had coincident cosmic triggers from two scintillators, one on top and another at the bottom of the RTPC. Signals from the scintillators are processed using discriminator, AND gate and NIM to ECL converter to get the required ECL signal which was fed to the front panel of the TI as discussed above.

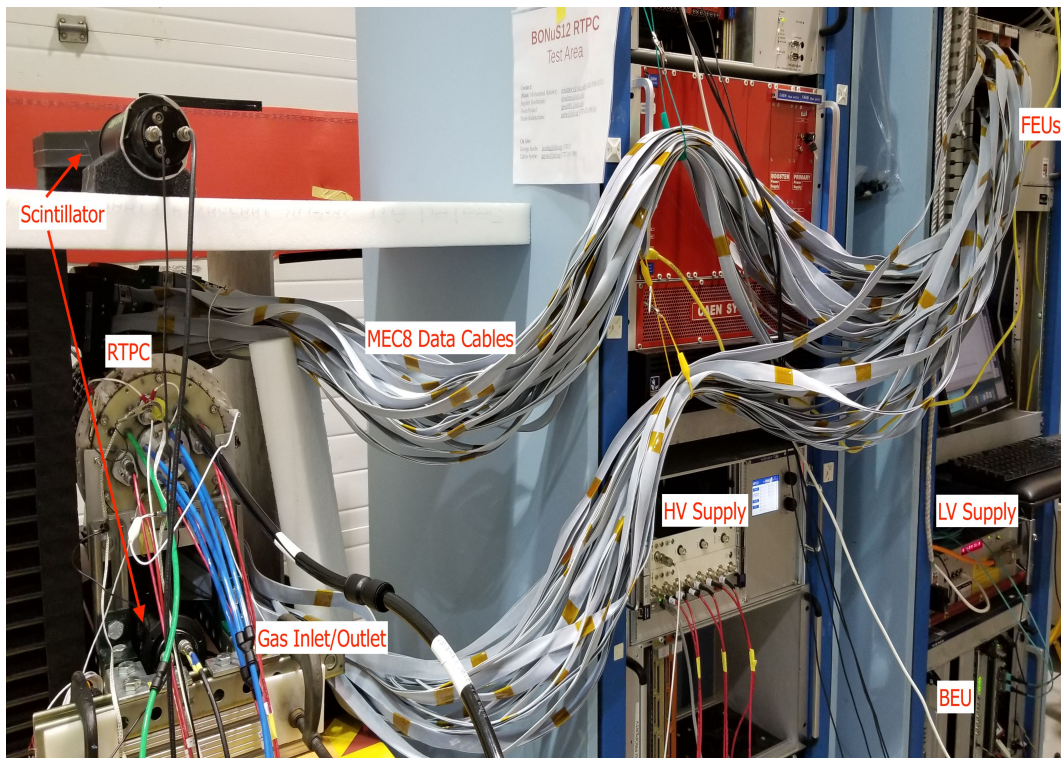


FIG. 56: Cosmic test setup of the RTPC with 8 available FEUs to test the functionality and performance of the detector at Jefferson lab.

TABLE 1: Operating Voltages of the RTPC at Jlab Testbench during Cosmic run.

Region	Voltage
Drift	3800 - 4350
GEM-1, GEM-2, GEM-3	382, 381, 380
Transfer-1, Transfer-2	300, 300
Induction	300

To finalize the operating voltage of this new RTPC, data were taken with a nominal 250 sccm flow of pre-mixed HeCO₂. After some test runs, we decided to use the high voltage setting shown in Table 1 as the best operational voltage.

Establishing pedestals before the cosmic ray test (see Appendix A) was important, as we wanted to test the pedestal equalization, zero-suppression together. Current pedestal or any previous pedestal run could be used for these process, but recent pedestals would be better if we re-assembled the cables or adapter board. No channels looked noisy in the initial tests, hence, no channels were masked during the cosmic ray data taking. Pedestal runs was taken with special standalone FEU commands as mentioned in Appendix C. CODA framework was used for the data acquisition of cosmic data so we could utilize the Hall B resources for monitoring the detector performance. Figure 57 showed a promising result of our test, ensuring that it had good occupancy and time distribution. Almost all rotations of the RTPC had similar good results.

The data from the cosmic test was also used by the members of the BONuS group to reconstruct the cosmic track. Details of the Reconstruction software for the RTPC detector was detailed in Ref. [36].

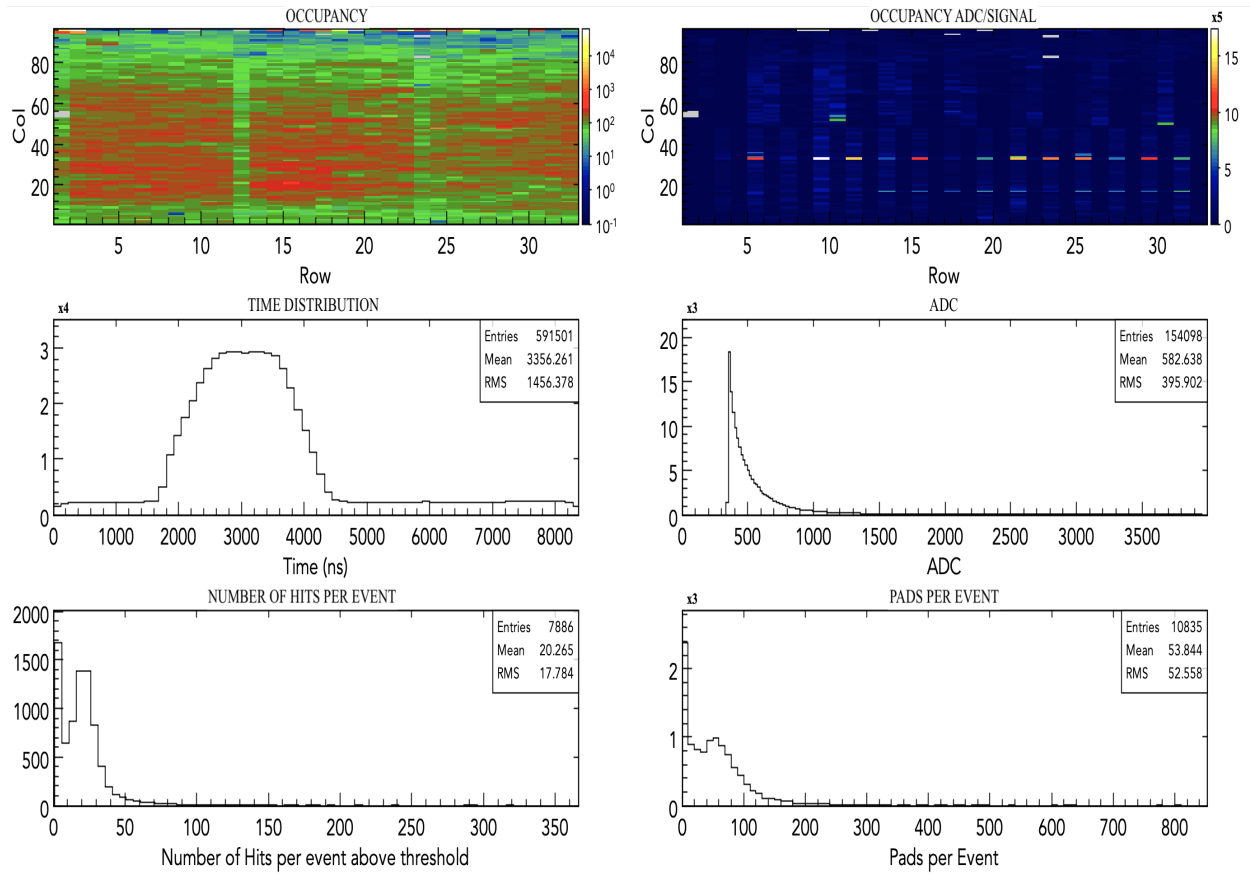


FIG. 57: RTPC system integrated to the CLAS12 monitoring showing promising result of occupancy, time distribution and pad hits of 8 Rows of connector during the cosmic test at EEL.

3.6 FINAL EXPERIMENTAL SETUP AND COMMISSIONING

The Continuous Electron Beam Accelerator Facility (CEBAF) [37, 38] and other experimental facilities at Thomas Jefferson National Accelerator Facility (Jefferson Lab) were designed and constructed in the 1990s and were operated successfully for over 15 years to explore and elucidate a wide range of physics topics. In the last decade, the CEBAF accelerator and experimental halls were upgraded to the new 12 GeV beam energy with an updated configuration as shown in Fig. 58. CEBAF consists of two parallel linear accelerators (Linacs) based on superconducting radio-frequency technology. The accelerator upgrade is achieved

by adding five accelerating cryomodules in each Linac section [39]. The new cryomodules contain 7-cell cavities instead of the 5-cell cavities of the original CEBAF. Polarized electrons are generated in the source (gun), pre-accelerated in the injector, and subsequently injected and accelerated in the north Linac. The electron beam is then bent in an arc to change in the opposite direction and injected into the south Linac, which is again bent by 180° and passed through the north Linac. With the upgrade, each Linac is now capable to accelerate electron beams of ~ 1.05 GeV which allows to deliver a ~ 2.1 GeV beam in 1-pass. Similarly, upgrades to the arc magnets and power supplies make it possible to deliver beam to all three experimental halls (A, B and C) at energies up to 10.6 GeV, with different energies of 1-pass to 5-pass. The intensity of the beam could be a total of up to $85 \mu\text{A}$ with a high polarization of up to 85% [40]. One added arc path for a total of 5.5 passes is capable to achieve the highest beam energy of 12 GeV for Hall D. This highest beam energy generated exclusively for Hall D is irrelevant of the beam energies at the other three halls [38]. The BONuS12 experiment is an experiment proposed to run in Hall B at the maximum electron beam energy available and the upgraded CLAS12 spectrometer discussed below.

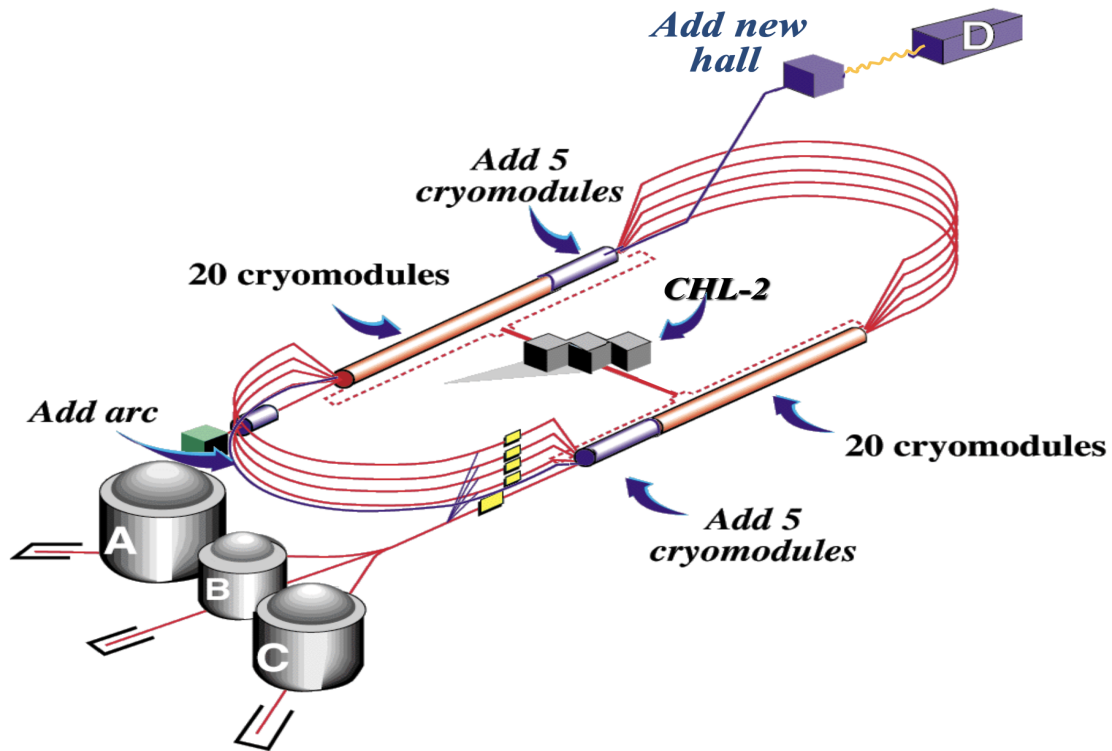


FIG. 58: Continuous Electron beam accelerator facility after 12 GeV upgrade.

3.6.1 CLAS12 SPECTROMETER

The CLAS12 spectrometer is designed to study nuclear and hadronic reactions of electron scattering by providing efficient detection of charged and neutral particles over a large acceptance range. It is based on a combination of a six-coil torus magnet, a high-field solenoid magnet and various particle detectors (tracking detectors, sampling detectors and time of flight detectors). The CLAS12 spectrometer relies on a combination of a toroidal magnetic field of ~ 2 T at polar angles from 5° to 35° , and a 5 T solenoidal field in the central region at polar angle range 35° to 125° seen from the target position. This combination permits the measurement of high momentum charged particles with a good resolution over a large coverage area, while operating the detectors with high luminosity. The solenoidal field also shields the detector system from low momentum electrons due to Møller scattering of the high-energy beam on atomic electrons in the target.

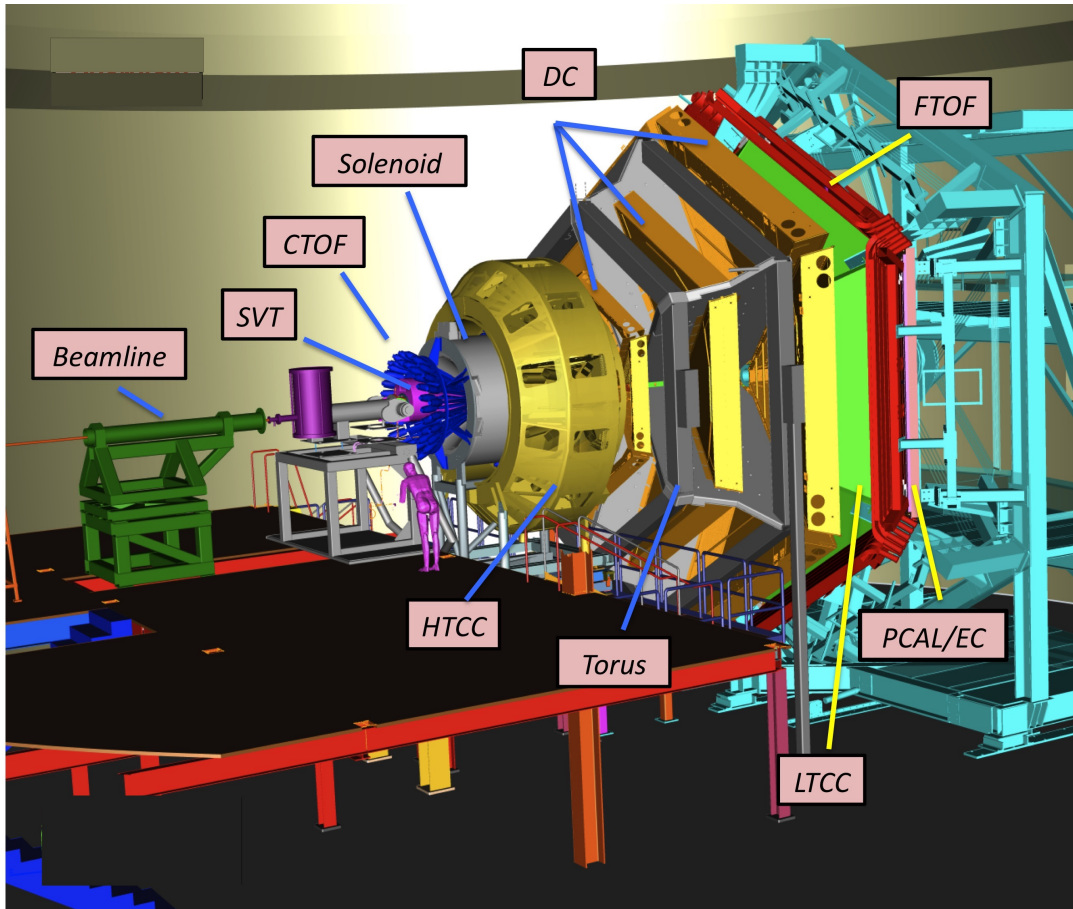


FIG. 59: Upgraded CLAS12 detector system.

The CLAS12 detector system is divided into two parts for convenience, namely Forward Detector (FD) System and Central detector (CD) system. The FD consists of Electromagnetic Calorimeters, Forward Time of Flight, Drift Chambers, High Threshold Cherenkov Counter and Forward Tagger (FT) in some experiments. Similarly, the CD is comprised of a Central Neutron Detector, Central Time of Flight and Central Vertex Tracker (CVT), except during BONuS12, when parts of the CVT were replaced by the RTPC. The Drift chambers track the charge particles at forward angles in an average momentum resolution of $\sigma_p/p < 1\%$. A combination of Cherenkov counters, time-of-flight systems, and calorimeters provides good particle identification for electrons, pions, kaons, protons and neutrons. The

CLAS12 spectrometer with its fast triggering and high data acquisition rates allows experimental operation at luminosity of $10^{35} \text{ cm}^{-2}\text{s}^{-1}$ for extended periods of time. Different subsystems of the standard CLAS12 detector are briefly described below:

- (i) **Torus Magnet:** The Torus magnets in the CLAS12 system divides the forward azimuthal coverage into six symmetric sectors. The geometrical coverage ranges from 5° to 40° in polar angle as seen from the target. This torus configuration provides the magnetic field around the beam-line for tracking of forward-going charged particles and also hosts other detector packages, eg. the Drift Chambers and Forward Tagger. The Torus magnet consists of six coils housed in an aluminum case that is approximately $2 \text{ m} \times 4 \text{ m} \times 0.05 \text{ m}$. The six coils produce a peak magnetic field of 3.58 T when powered at 3770 A. The magnet has an overall inductance of 2.0 H, stored energy of 14.2 MJ, and is roughly 8 m in diameter. Each coil is conductivity cooled by liquid helium supplied at 4.5 K from cooling tubes located on the coil inner diameter. The six coils are mounted in a central cold hub on a common stainless-steel cylinder, which also provides the geometrical symmetry for the alignment of the coils near the magnet center. The acceptance of scattering particles depends on the polar angle of the particle trajectory, with azimuthal coverage ranging from 50% at 5° to about 90% of 2π at 40° as seen from the target. Reference [41] details the design, construction and performance of the CLAS12 Torus magnet.
- (ii) **Solenoid Magnet:** The Solenoid magnet is a self-shielded superconducting magnet around the Hall B beam-line that is used to generate a magnetic field along the beam direction. The CLAS12 Solenoid magnet provides the magnetic field for the tracking of charged particles at large angle and suppression of low energy Møller electron background. The large majority of Møller electrons are prevented from reaching the sensitive detectors as they curl up in the strong longitudinal magnetic field, and are then guided into a shielding pipe to dump their energy. The Solenoid also provides a highly uniform magnetic field along the beam-line for the operation of polarized targets. It hosts several detector packages including the Central Vertex Tracker/ RTPC detector, the Central Time of Flight, and the Central Neutron Detector inside its bore of 78 cm diameter. The solenoid has four main coils and one shield coil. The 4 cylindrical coils are arranged in two packages at different radial distances from the beam-line. A fifth coil is located outside of the 4 coils and generates a magnetic field in the opposite direction of the 4 other coils, acting as an active magnetic shield. The

number of turns in the main coils is 3704 and in the shield coil it is 1392. The solenoid produces a magnetic field of 5 T when powered at nominal 2416 A. The magnet has an overall inductance of 5.89 H and stored energy of 17.2 MJ. The cool down system for the solenoid similar to the torus with liquid helium at 4.5 K. Reference [41] details the design, construction and performance of the CLAS12 Solenoid magnet.

- (iii) **Electromagnetic Calorimeter (EC):** The EC is the outermost layer of the CLAS12 forward detector system. The EC system is used primarily for the identification and reconstruction of charged (electrons, pions) and neutral particles (photons, neutrons) in electron-scattering experiments. The EC includes both the electromagnetic calorimeters (ECAL) of the former CLAS detector and the new pre-shower calorimeter (PCAL) modules installed just upstream of the ECAL. Both ECAL and PCAL are lead-scintillator sampling calorimeters consisting of six modules in compliance with the six sectors of the Forward detector system. The ECAL also consists of two parts namely ECAL-INNER (ECIN) and ECAL-OUTER (ECOUT). They provide longitudinal sampling of electromagnetic showers, as well as of hadronic interactions to improve particle identification. Each EC module has a triangular shape with 54 (15 PCAL/15 ECIN/24 ECOUT) layers of 1 cm thick scintillators segmented into 4.5 cm and 10 cm wide strips for PCAL and ECAL sandwiched between 2.2 mm thick lead sheets. The total thickness corresponds to approximately 20.5 radiation lengths. Scintillator layers are grouped into three readout views with 5 PCAL, 5 ECIN and 8 ECOUT layers per view, providing spatial resolutions of less than 2 cm for energy clusters. The light from each scintillator readout group is routed to the PMTs via flexible optical fibers. Reference [42] details the design, construction and performance of the CLAS12 EC system.
- (iv) **Forward Time of Flight (FTOF):** The FTOF detector is a part of CLAS12 forward detector system located just upstream of the PCAL, mounted on the Forward Carriage in Hall B. This detector is used to measure the time of flight of the particles emerging from the target during the scattering experiments. In each sector of CLAS12, the FTOF detector is comprised of three arrays of scintillators: panel-1a, panel-1b, and panel-2. Each of the panels consists of a set of rectangular plastic scintillation counters with a PMT on each end. The panel-1a and panel-1b arrays are located at polar angles from 5° to 35° and the panel-2 arrays are located at larger angles from 35° to 45° . The panel-1b is located upstream of panel-1a. In each sector, the panel-1a arrays contain

23 counters, the panel-1b arrays contain 62 counters, and the panel-2 arrays contain 5 counters. The FTOF is required for excellent timing resolution in particle identification and good segmentation for flexible triggering options. The average timing resolution of panel-1a, panel-1b and panel-2 are 125 ps, 85 ps and 155 ps, respectively. The FTOF covers a range in polar angle from 5° to 45° , covering 50% in ϕ at 5° and 90% at 45° as seen from target. Reference [43] details the design, construction and performance of the CLAS12 FTOF.

- (v) **Low Threshold Cherenkov Counter (LTCC):** The LTCC is composed of five identical detectors placed just upstream of the FTOF in CLAS12. The LTCC is used for the identification of charged pions at momenta greater than $3.5 \text{ GeV}/c$, providing pion/kaon discrimination. The LTCC consists of boxes shaped like truncated pyramids, equipped in five out of the six sectors of CLAS12. Each LTCC box contains 108 lightweight mirrors with composite backing structures, 36 Winston light-collecting cones, 36 125 mm diameter PMTs, and 36 magnetic shields. The detector is filled with heavy gas C_4F_{10} , with distinct threshold for pions and kaons, supplied by the Hall-B Gas system. The gas is cleaned, re-circulated, and maintained at a pressure between 1 – 4 inches of water column (wc). This subsystem of CLAS12 Forward detector also has coverage from 5° to 30° in polar angle as seen from the target. Reference [44] details the design, construction and performance of the CLAS12 LTCC.
- (vi) **Ring Imaging Cherenkov (RICH):** The RICH detector replaces two sectors of the corresponding CLAS12 LTCC detector, with replacement in sector 4 already completed. The RICH improves the particle identification especially separating kaons from pions and protons in the energy range from 3 to $8 \text{ GeV}/c$. It incorporates a hybrid optic solution with aerogel radiators, light planar and focusing mirror system, and highly segmented photon detectors to reduce the detector area to 1 m^2 . Multi-anode photomultiplier tubes (MaPMTs) allow to have the required spatial resolution and match the aerogel Cherenkov light spectrum in the visible and near-ultraviolet region. This subsystem of the CLAS12 Forward detector also has coverage from 5° to 40° in polar angle as seen from the target. Reference [45] details the design, construction and performance of the CLAS12 RICH.
- (vii) **Drift Chamber (DC):** The DC system consists of 18 identical wire chambers in six sectors located at three different regions: ‘R1’, ‘R2’, and ‘R3’ along the beam-line. The six coils of the torus magnet mechanically support the three independent DCs in each of

the six sectors. Six triangular shaped DC chambers located at the entrance (upstream) of the torus magnetic field are recognized as R1 region, the next six chambers located inside (within) the torus magnet where the magnetic field is close to its maximum are recognized as R2 region, and the remaining six chambers in a low magnetic field space just downstream of the torus magnet are recognized as R3 region DC chambers. In each of the six torus sectors the DCs are arranged identically. Each chamber has wires arranged in two superlayers of 6 layers by 112 sense wires. Two adjacent superlayers are oriented at $\pm 6^\circ$ with respect to the sector midplane. This stereo view enables excellent resolution in the most important polar angle, and good resolution in the less critical azimuthal scattering angle. The DC along with the torus field is used to determine the trajectory of the charged particles. The drift chamber operates within an environment of a mixed, clean, pressure-controlled argon:CO₂ (90:10) gas supplied to each of the 18 drift chambers. The on-chamber amplifier and readout boards are used for data acquisition which are called signal translator boards (STBs). The CLAS12 DC has coverage from 5° to 40° in polar angle with 50% of azimuthal coverage at 5° as seen from the target. Reference [46] details the design, construction and performance of the CLAS12 DC.

- (viii) **High Threshold Cherenkov Counter (HTCC):** The HTCC is a single unit detector that covers the entire working acceptance of CLAS12 in the forward direction. It is mounted on a special cart and located between the Central Detector and the Drift Chambers. The HTCC is constructed using multi-focal mirrors of 48 elliptical mirror facets that focuses the Cherenkov light on 48 PMTs. The HTCC is filled with dry CO₂ gas at room temperature and low positive differential pressure. It is directly connected to a CO₂ gas line and must be continuously purged to keep the relative humidity very low. The CLAS12 HTCC has full coverage of 360° in azimuth from the beamline, and spans between 5° and 35° in polar direction. It is used to separate electrons/positrons with momenta below 4.9 GeV from charged pions, kaons, and protons. This detector operates in conjunction with the EC to identify electrons of specific energies. It is also used to generate a fast signal which is used as a trigger. Reference [47] details the design, construction and performance of the CLAS12 HTCC.
- (ix) **Central Neutron Detector (CND):** The CND is the outer-most detector of the CLAS12 Central Detector system. The CND is a barrel of plastic scintillators of trapezoidal shape, all with their long sides parallel to the beam direction. The CND

is composed of 3 layers of scintillator paddles in the radial direction with 48 paddles in each layer totaling 144 scintillators. Each scintillator is read out only on one side (upstream) using 144 PMTs placed at a low-field region of the solenoid magnet using long, bend light guides. The other end (downstream) of each bar is connected via a ‘U-turn’ light guide to the neighboring paddle so that the light at the downstream end goes through the neighboring paddle to read it out. The CND allows the detection of neutrons in the momentum range from 0.2 to 1.0 GeV/ c by measuring their time of flight from the target and the energy deposition in the scintillators. This CLAS12 CTOF has coverage from 40° to 120° in polar angle and 360° azimuthally as seen from the target. Reference [48] details the design, construction and the performance of the CLAS12 CND.

- (x) **Central Time-of-Flight (CTOF):** The CTOF system consists of 48 scintillators that is located within the superconducting solenoid magnet radially inside of the CND. The array of counters forms a hermetic barrel around the Central tracker. Each scintillator is read out on both ends using PMTs through long light guides. The PMTs reside in inhomogeneous fringe fields of 0.1 T from the magnet and must be operated within specially designed magnetic shields with compensation coils. The CTOF system is used for the identification of charged particles emerging from the target via time-of-flight measurements in the momentum range from 0.3 to ≈ 1.25 GeV/ c with a time resolution of 80 ps. This CLAS12 CTOF has a coverage from 35° to 135° in polar angle and 360° azimuthally as seen from the target. Reference [49] details the design, construction and performance of the CLAS12 CTOF.
- (xi) **Central Vertex Tracker (CVT):** The CVT is a part of the Central Detector to measure the momentum and to determine the vertex of charged particles scattered from the target. The CVT is inside the solenoid magnet covering the target which aligns along the beamline. It consists of two separate system, the Silicon Vertex Tracker (SVT) and the Micromegas Vertex Tracker (MVT). The SVT system includes 3 concentric polygonal regions with 10, 14, and 18 double-sided modules (total 6 layers of 42 modules) of silicon sensors instrumented with a digital readout ASIC (Fermilab Silicon Strip Readout). Reference [50] details the design, construction, and performance of the CLAS12 SVT. The MVT is a combination of the Barrel Micromegas Tracker (BMT) and Forward Micromegas Tracker (FMT). The BMT contains 3 layers of strips along the beamline and 3 layers of circular readout strips around the beamline. The

BMT provides improvement in momentum resolution and in tracking efficiency of the scattered particles in the central region. Each BMT layer is arranged azimuthally in 3 segments of 120° each, covering total of 360° . Both the SVT and MVT have a coverage from 35° to 135° in polar angle and 360° azimuthally as seen from the target. Another component, the FMT, is integrated into the CVT to provide a compact tracking system covering the polar angle from 6° to 30° and provides improved vertex reconstruction for forward-scattered charged particles. Reference [31] details the design and performance of the CLAS12 BMT and the FMT. The CVT is replaced with the RTPC in the BONuS12 experiment, but 3 layers of the FMT remained and were used in this experiment.

3.6.2 HALL B BEAMLINER

The Hall B beamline has two portions: the 2C line and the 2H line. The 2C line starts from the beam switch yard (BSY) to the Hall proper, and the 2H line extends from the upstream end of the experimental hall to the beam dump/Faraday cup in the downstream tunnel. The beamline is comprised of beam optics, beam position and beam current monitors, beam viewers, collimators, shielding, beam profile scanners, and beam halo monitors. Devices that control the beam direction, profile and other critical parameters are controlled by the accelerator operators, whereas collimators, halo monitors, profile scanners, viewers and beam blocker are controlled by the Hall B operators. Reference [51] details the CLAS12 beamline, its components and the operation.

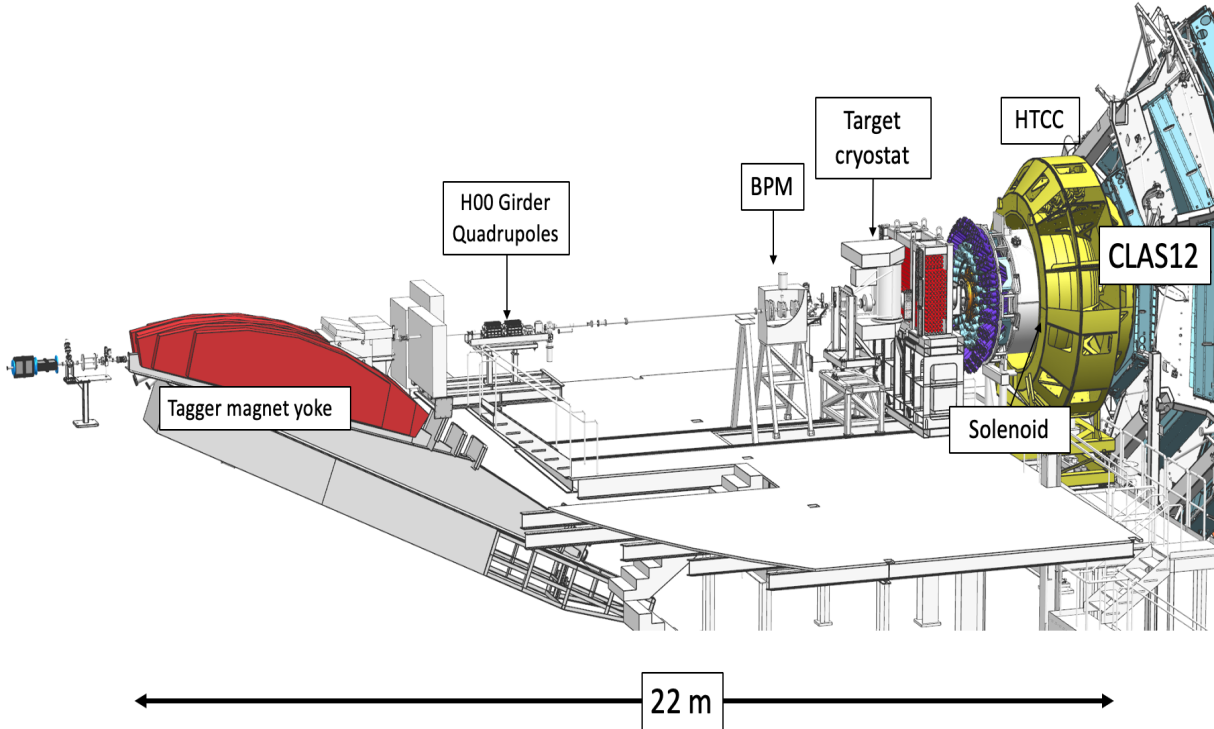


FIG. 60: Hall B beamline upstream of the CLAS12 detector showing part of the 2H line from the tagger magnet yoke to the entrance of the CLAS12.

3.6.3 INTEGRATION OF THE RTPC AND COMMISSIONING

Before data taking with the electron beam in hall B the RTPC detector had to replace the SVT and MVT on the CVT cart. Initially, all components of the RTPC (Adaptor boards, MEC8 cables, HV cables, gas tubes) were installed on the CVT cart of the CLAS12 detector system at our testbench in EEL. The upstream part of the CVT cart hosted six FEU crates (see Fig. 61) symmetrically around it which resided outside the solenoid but within the residual field of ~ 1 T. Each FEU crate had 8 FEUs, among which 6 were reserved for the BONuS12 RTPC and the remaining two for the FMT in each crate. Out of the two BEUs (mvt1 and mvt2) used in the hall, one was available at the test area which was used to test the connectivity of our readout components with the usual pedestal analysis described above. After the installation of the RTPC in the CVT cart and a brief cosmic run was taken to

make sure that nothing was broken during the installation and the RTPC was performing as usual. The results from the cosmic test was promising, and had not changed much compared to the cosmic test before installation, except some noisy channels in the FEUs (less than 10 channels out of 17,280). We could mask or increase threshold of these noisy channels but we waited till we take the whole system to the hall.

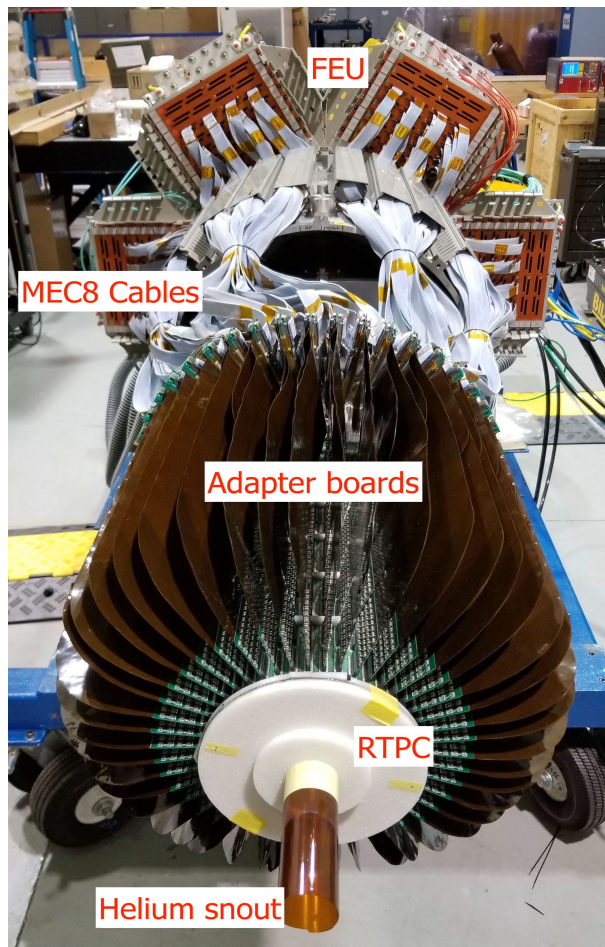


FIG. 61: Completion of the RTPC installation in the CVT cart which hosted 6 FEU crates in the upstream.

After installation of the RTPC on the CVT cart, the HV supply module, the gas panel and its control chassis were taken to the hall and installed in the pre-determined location and preparing for final tests of the RTPC before commissioning of the BONuS12 experiment. The EPICS GUI for the BONuS12 (Fig. 62) was available and some components were also tested from our testbench.

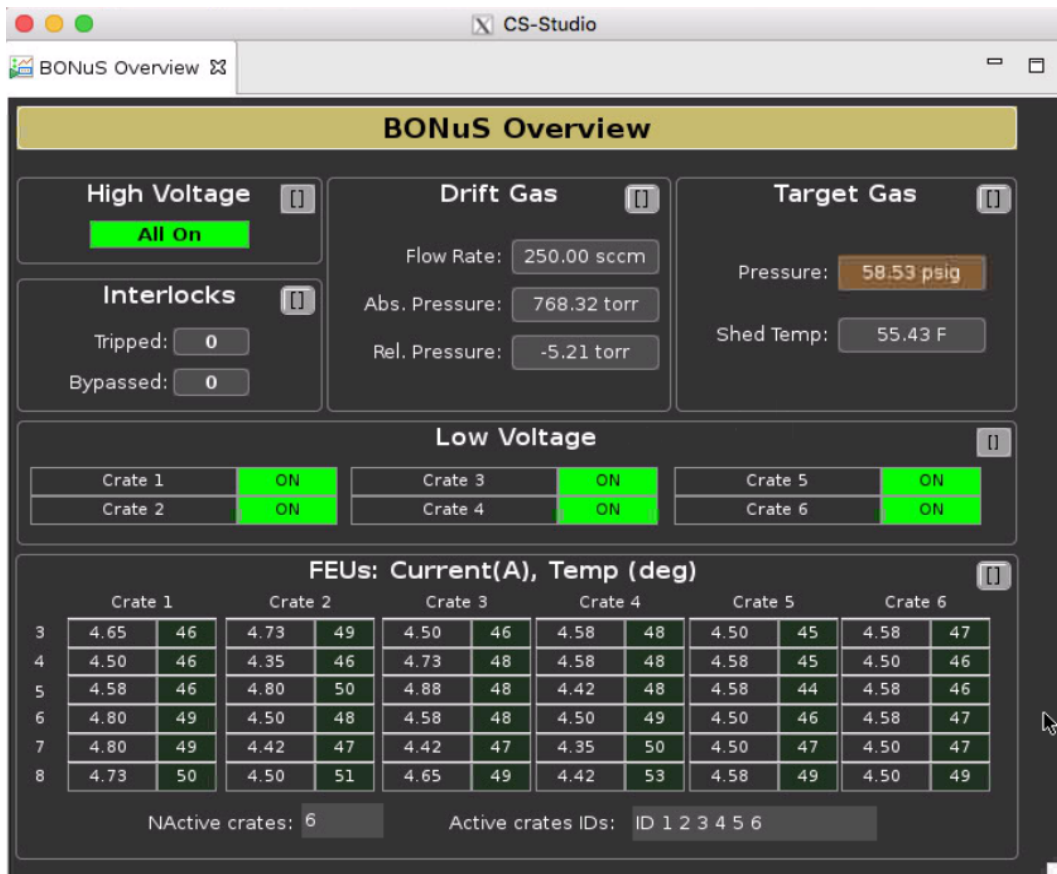


FIG. 62: BONuS (RTPC) Overview GUI.

A Labview program (Fig. 63) was installed on the experimental hall computer to control the drift gas system and target gas system and set up to operate remotely. Gas system monitoring was integrated with the EPICS system.

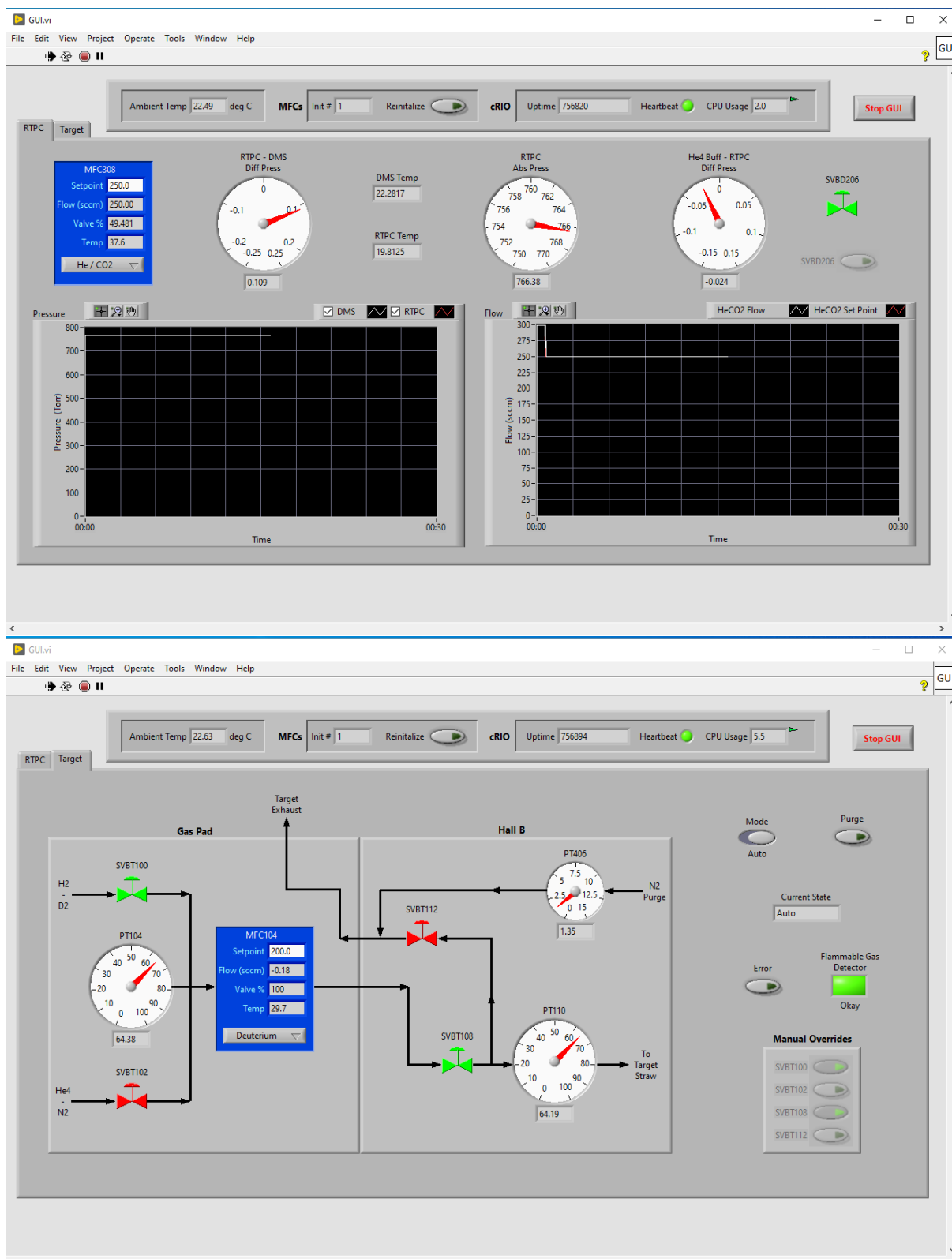


FIG. 63: Lab-view Interface of the RTPC gas control (top) and Target gas control (bottom) during the BONuS12 experiment.

The RTPC detector installed to the CVT card was also moved to the hall from the testbench at EEL, and craned to the Level-2 of the hall where our detector was pushed downstream into the CLAS12 solenoid as shown in Fig. 64. The solenoid was already hosting two other detectors, CTOF and CND. The CTOF detector was used as a cosmic trigger generator during the commissioning of the RTPC detector. The detector readiness was checked by new pedestal data taking before pushing the RTPC inside the solenoid. Some cable connections had to be fixed and another pedestal run taken (see Appendix A). We then masked some channels which were too noisy and also masked some DREAMs which would not be used during the BONuS12 experiment. We took almost all the pedestal runs without HV in the RTPC detector, and also used high rate of data taking with small number of samples only. The files obtained from the pedestal run were later used in the data taking configuration as a reference for the pedestal subtraction and the zero suppression. Zero suppression of the BONuS type was implemented for all data taking following these tests with a threshold of the average pedestal + 6 x sigma (noise).

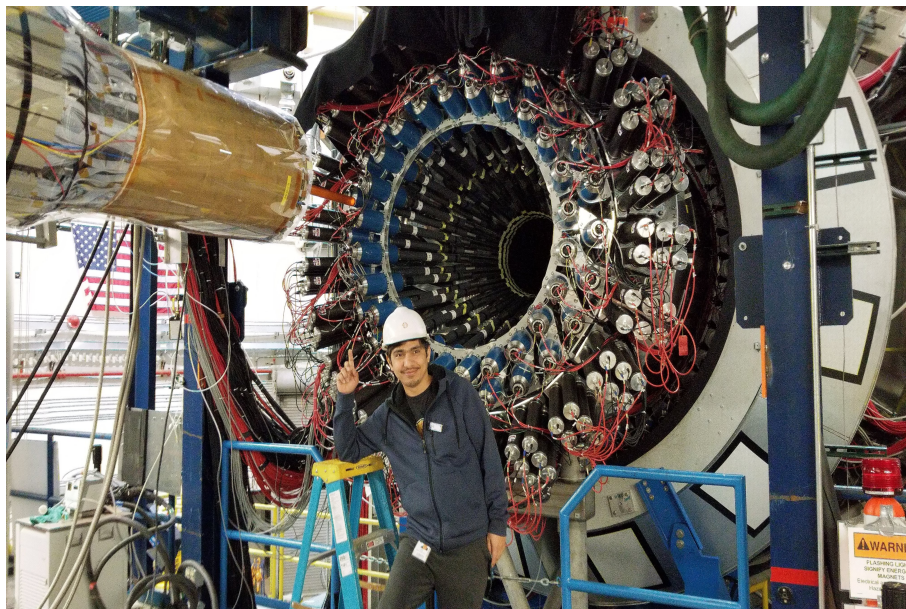


FIG. 64: RTPC detector installed in the CVT cart (on the left top side) ready to push inside the CLAS12 Solenoid (hollow seen as a white ring on the back).

Experimental interlocks, as shown here Fig. 65, were high voltage related as explained above and others were related with the drift gas as it was a critical component of the RTPC detector. Every interlock was working as expected to prevent the systematic as well as human errors. We also included the bypass option in the interlock interface for a debugging purposes, otherwise all the interlocks should be running during the whole experiment.

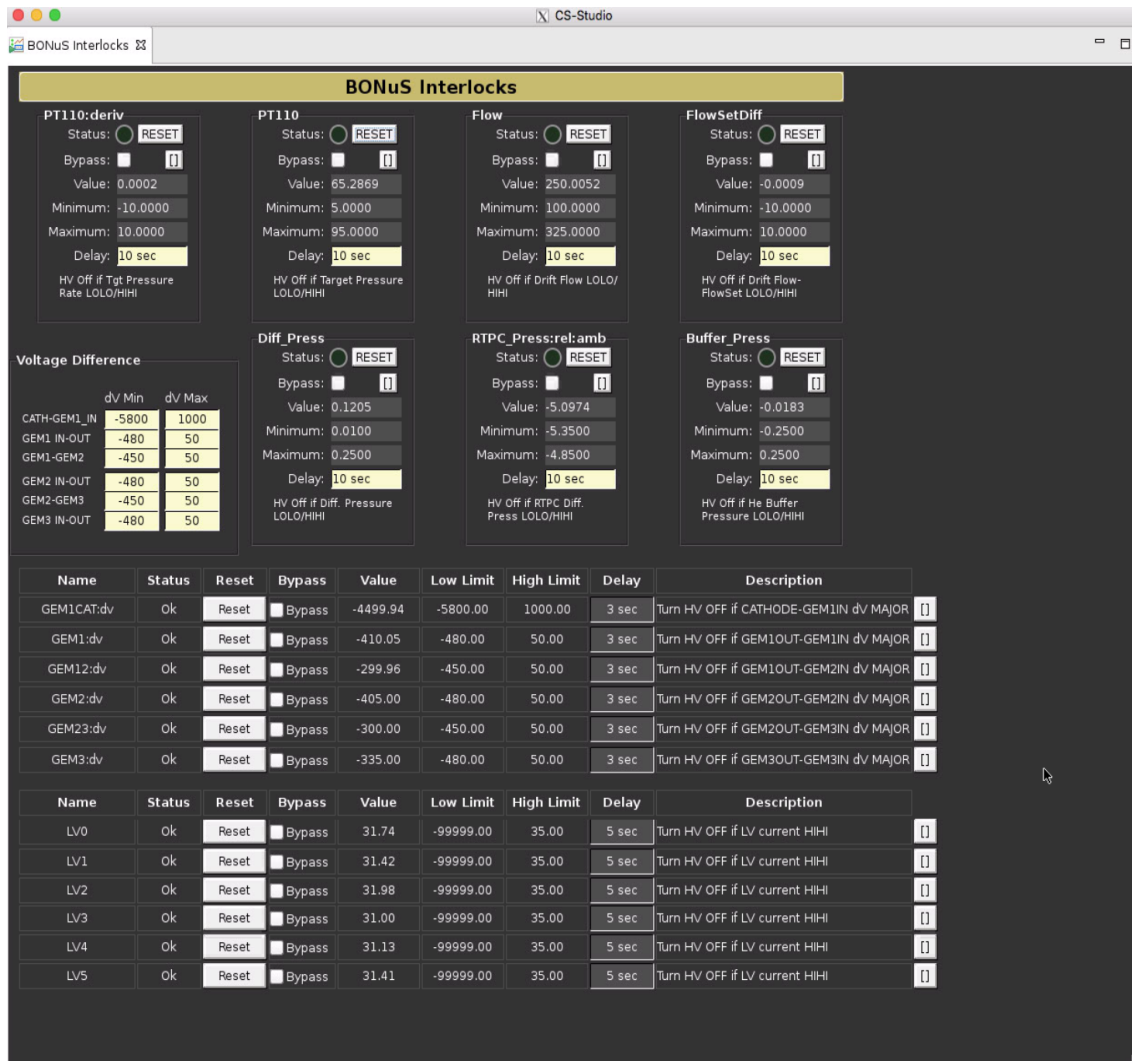


FIG. 65: RTPC interlocks in EPICS.

For commissioning the RTPC in hall B, we prepared a cosmic run with a simple CTOF hit trigger configuration implementing the CLAS12 Trigger Supervisor (TS) and TI. First we chose a usual trigger delay setting of CLAS12 to observe the output data without the solenoid magnetic field. Fig. 66 captured from the online CLAS12 monitoring shows a complete picture of the occupancy of the RTPC, the time distribution, ADC distribution, number of pad hits/event. The performance of the RTPC was elegant with nominal HV setting found at the testbench and 250 sccm flow of drift gas, HeCO₂. In the occupancy plot we could clearly see 16 sectors separated by the fading line parallel to Y-axis manifesting the 16 sectors of the RTPC GEM foils. The time distribution also matched with our prediction and testbench results.

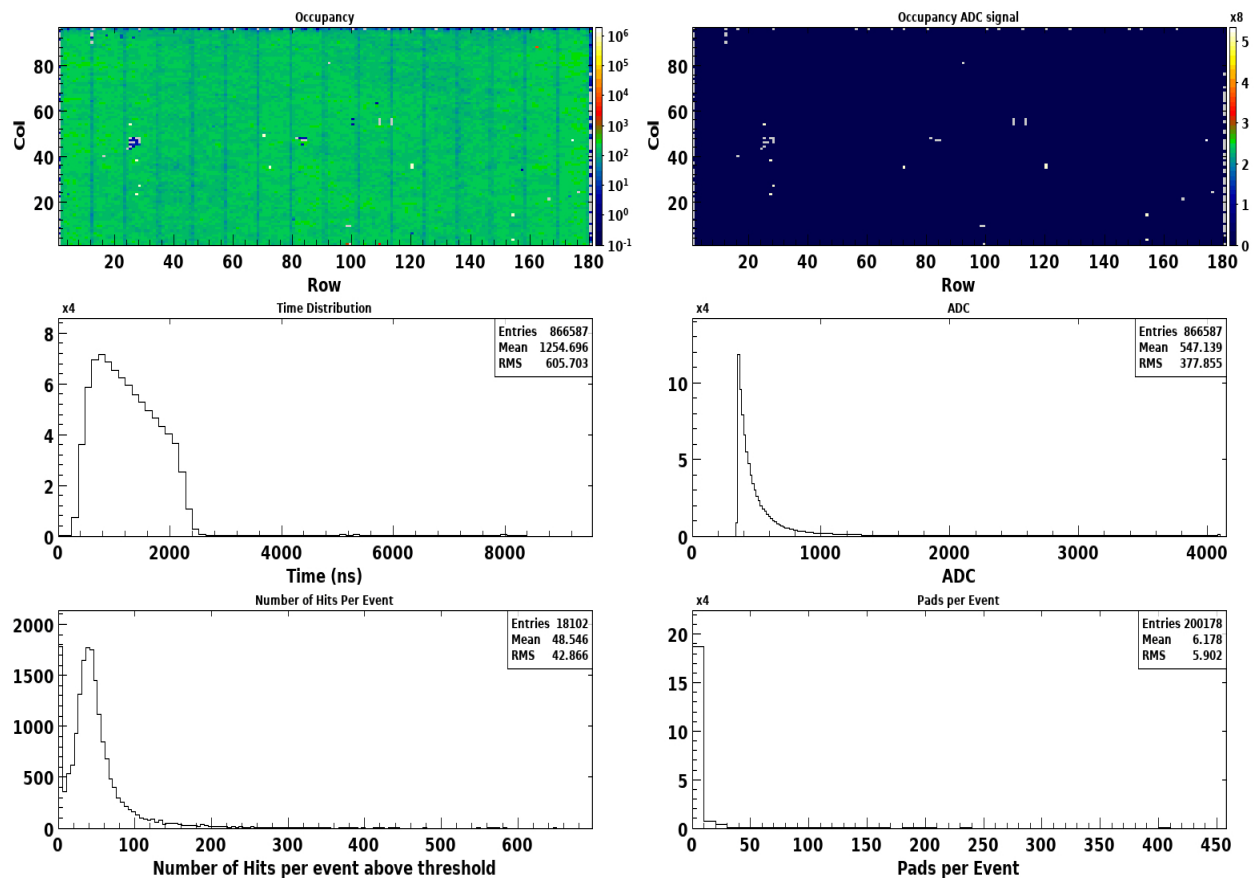


FIG. 66: Occupancy and time distribution plot of the RTPC detector without solenoid magnetic field during the commissioning.

Reconstruction software [36] was tested by reconstructing cosmic ray events as shown in Fig. 67. Portions of the cosmic ray tracks were clearly reconstructed.

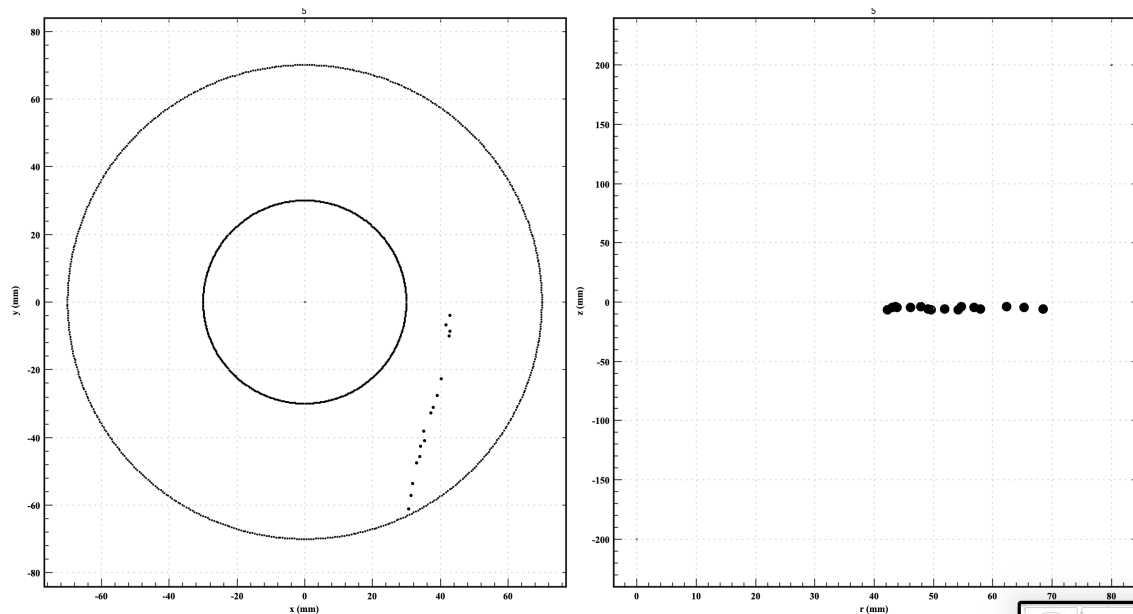


FIG. 67: Reconstruction of the cosmic radiation in the BONuS12 RTPC [courtesy of David Payette].

After completing these tests satisfactorily, the RTPC detector was ready for data taking in Hall B. Even though the BONuS12 experiment was proposed to run with a 5 T solenoid magnetic field, the RTPC did not have its optimal performance at this field strength. We also had issues to see real signals from the RTPC while continuing the cosmic test with the solenoid field. We had to ramp down the magnetic field below 2 T to see cosmic signals. This could be due to the low curvature of ionized electrons moving under electric and magnetic field which hardly reaches the readout pad or it could be the GEM structure which blocked drift electrons to enter through the hole, otherwise made avalanche electrons to recombine curling back to the lower potential side. For the cosmic test, it was also the choice of trigger which might not have traversed through the RTPC. In any case, we tested various

combination of GEM and drift voltages at 5 T but did not see much difference. It was decided to decrease the field in steps and study the performance of the RTPC. After going from 5 T to 3.5 T, we found that the RTPC could work at 3.8 - 4 T without any issues, and it would also not compromise the physics results.

3.7 DATA TAKING

We started data taking on February 12, 2020 with a total of 80 days of run period in Hall B. However, after running for about one month, the first RTPC detector started to show issues of leakage current and was almost inoperable by the middle of March. RTPC-1 was replaced by RTPC-3 beginning on March 16. It was not possible to change the detector at Level-2 of the hall, so the CVT cart was again craned to the ground level of the hall. The recabling process shown in Fig. 68 had to follow the same channel mapping as used for RTPC-1. The testbench BEU was used for a preliminary continuity test of the readout electronics. We completed our change-out process within two days and the CVT cart was again brought back to Level-2. Before re-establishing data taking with the electron beam, we followed the cosmic ray test procedure to make certain that the detector was working.



FIG. 68: Cabling work while installing the RTPC in the CVT cart.

Data taking was again resumed on March 20, but the closing of Jefferson lab due to COVID-19 halted the run. Data taking resumed on August 2, 2020. During the closing of Jefferson Lab, a small amount of drift gas was continuously flowing through the detector system and it was remotely monitored. The data taking of BONuS12 in Hall B was completed successfully on September 21, 2020 with 2 hrs of cosmic data after beam was taken out in the morning. In the spring and summer of 2020, a total of 5.7 billion electron trigger events were collected, details are shown in Table 2.

TABLE 2: Amount (in Millions) of the collected data during the BONuS12 experiment at the Hall B of the Jefferson Lab in Spring and Summer 2020.

Beam energy	Spring 2020 (events) (02/12 - 03/24)	Summer 2020 (events) (08/02 - 09/21)	target gas	total
Pass-1 (2.1 GeV)	1	22	Empty	23
	81	185	H2	266
	37	45	D2	82
	19	44	He4	63
total	138	296		434
Pass-5 (10.6 GeV)	21	45	Empty	66
	151	266	H2	417
	2275	2355	D2	4630
	77	51	He4	128
total	2524	2717		5241

During the writing of this thesis, the calibration and the analysis work of the collected data is ongoing. I have also participated in the calibration of the BONuS12 data (Run group F), but I am more involved in the TCS data analysis of another experiment of CLAS12 (Run group A) so the following chapter details the analysis framework of the TCS analysis with CLAS12 RG-A data.

CHAPTER 4

CLAS12 RUN GROUP A AND THE TCS ANALYSIS

4.1 EXPERIMENTAL SET-UP OF RUN GROUP A

The CLAS12 Run Group A (RG-A) program was formed by a collaboration of 13 experiments of five topical categories: Deep Inclusive and Semi-inclusive Scattering, Deep Exclusive Scattering, Quasi-photoproduction, Nucleon Structure and Meson Exchange (MesonEx) programs. These experiments were designed to study the proton structure, including 3D imaging, and the gluonic excitations within the proton to understand the strong force and the origin of the nucleon mass. Until now, RG-A acquired data in three separate run periods (spring 2018, fall 2018, and spring 2019) utilizing nearly half of the approved RG-A beam time. The standard CLAS12 spectrometer (section 3.6) consisted of the central detector system (MVT, FMT, SVT, CTOF, CND and the Solenoid magnet), the forward detector system (HTCC, DC, FTOF, LTCC, EC and the Torus magnet), and the forward Tagger (FT) to track and identify the associated particles in the RG-A experiment.

The target of the RG-A was cryogenic liquid hydrogen (LH2) with a density $\sim 71 \text{ mg/cm}^3$. Hall B current target cell is a 50 mm long Kapton cone with 23.66 mm upstream and 15.08 mm downstream diameters. The entrance and exit windows for the beam are 30 μm thick aluminum. The scattering chamber is made up of Rohacell XT110 foam and is $\sim 45 \text{ cm}$ long with a 100 mm outer diameter fitting inside the SVT as shown in Fig. 69.

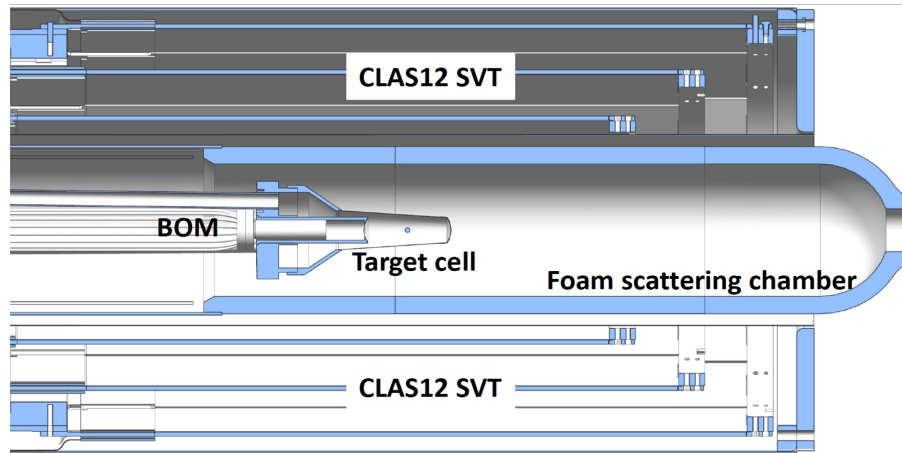


FIG. 69: Design of the Hall B Cryogenic target inside the SVT.

The trigger system of CLAS12 [52] is designed in such a way that it can include potentially any detector that uses Flash Analog to Digital Converters (FADCs) in their front-end electronics. These include: HTCC, LTCC, FTOF, PCAL, EC, CTOF or CND. As RG-A is a collaboration of various physics experiments sharing the common CLAS12 setup, it includes variety of trigger choices, eg. electron triggers, opposite sector triggers (muons), the MesonEx triggers and others.

The Data Acquisition of CLAS12 [35] is a fully network-based system consisting of different hardware and software implementations. These different components (Fig. 70) have to follow certain requirements to be compatible with the CLAS12 DAQ. Parallel optical fibers are used to distribute the synchronization reset and trigger signals to all of these components, and to collect the busy signals from the electronics. Data from the VME/VXS crate are transferred to the Event Builder (EB) via 1 Gb or 10 Gb Ethernet links over the TCP connections. The events built on EB are further passed to the multi-threaded program system, Event Transfer (ET) system. Lastly, events from the ET system are acquired by the Event Recorder (ER) system which writes the events to the disks. These recorded events are then available for the offline analysis.

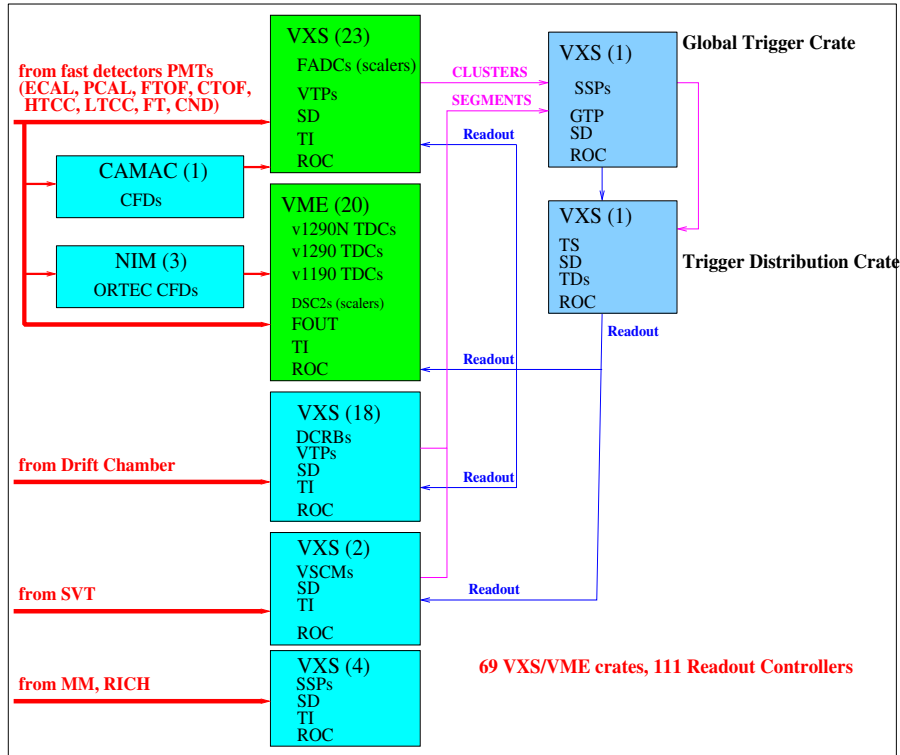


FIG. 70: Summary diagram of the Data acquisition system of the standard CLAS12 [35].

RG-A collected production data of both polarities of the torus magnet (indending and outbending data) with an electron beam energy of 10.6 GeV. The beam current ranged from 5 to 75 nA. During RG-A data taking, the Møller polarimeter located upstream of the CLAS12 tagger dump, periodically measured the beam polarization which averaged about $\sim 87\%$.

4.2 DATA PROCESSING

4.2.1 EVENT RECONSTRUCTION

Keeping in mind the complex nature of the detector systems and corresponding large data volumes, the CLAS12 software group maintains a common framework consisting of essential libraries of software tools, detector reconstruction and analysis applications for physics data processing. The common framework, CLAS12 Reconstruction and Analysis (CLARA)

framework, relies on the data-stream processing and allows to create service-oriented applications with the basic micro-services linked by data-stream pipes. A micro-service receives an input data stream, processes it, and passes output data in CLAS12 bank structure to the next micro-service in the data-flow path. Within the framework, software tools support and standardize event reconstruction including detector geometry, calibration, monitoring and CCDB access. This framework enables execution in multi-threaded mode via event-level parallelization for the CLAS12 reconstruction. Even if CLARA framework supports Java, C++ and Python, all the reconstruction services are using Java within CLARA currently. Reference [53] provides the details for the CLARA framework and its tools.

Within the CLARA framework, the data collected by the DAQ (detector identifier and the digitized ADC and TDC data) are first decoded and grouped into a bank structure [54, 55] for each event. These detector banks contain all components (hits, time, cluster, tracks, etc.) required for the event reconstruction in both CD and FD systems. In both systems, track reconstruction comprises of an algorithm for pattern recognition as well as track fitting. First, charged particle tracks are reconstructed in both the CD and FD tracking systems using hit-based tracking, matching the hit position recorded in the different detectors. In parallel, track reconstruction with the hit time and energy also undergo in other detector systems. Then, matching between two is performed by the Event Builder (see below). The unmatched hits/tracks are reserved as neutral candidates (photon, neutron). With the matching track, reconstruction of start time is imminent, which allows to reiterate the time-based tracking including the drift time of DCs. The improved tracks from the time-based tracking are inputs for the Event Builder again as shown in Fig. 71, which leads to the final event reconstruction.

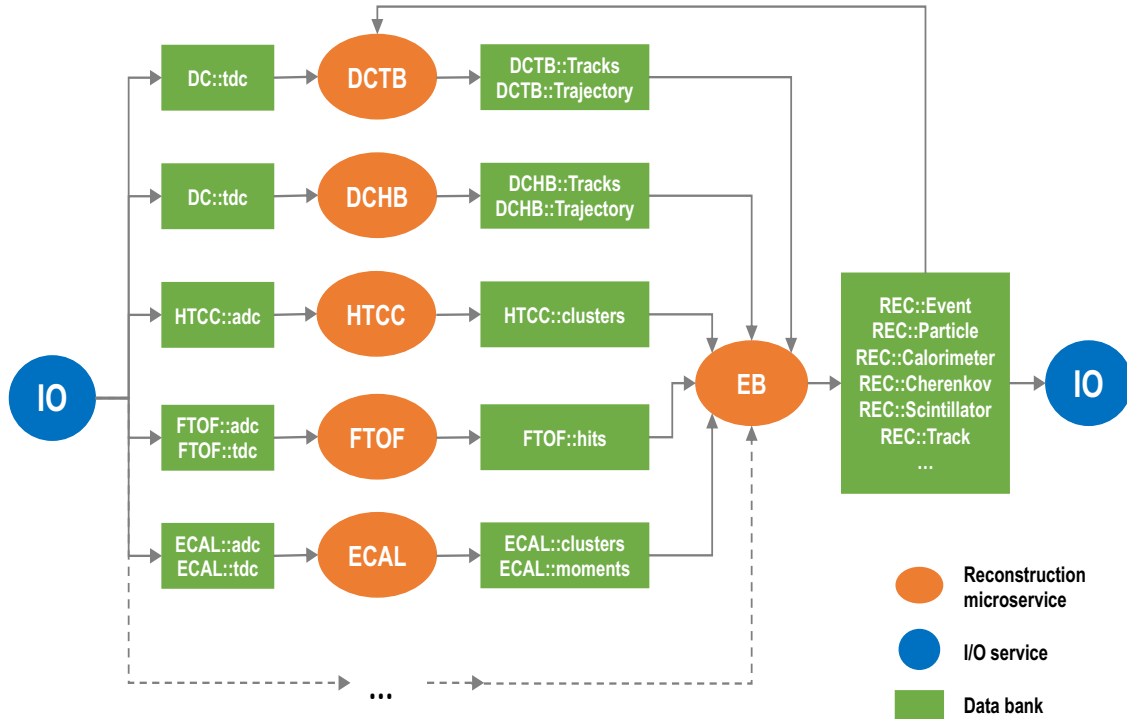


FIG. 71: CLAS12 interdependence of several subsystem within the CLARA framework for Event Builder (EB) service [53].

CLAS12 DAQ stores the raw data in the EVIO (Event Input–Output) format designed by the Jefferson Lab Data Acquisition Group. During the decoding process, EVIO is converted to the CLAS12 data format, known as HIPO (High Performance Output), which is a flexible data container structure minimizing disk space and access during the reconstruction process and further data analysis. Both Java and C++ libraries are supported by the HIPO format.

4.2.2 CLAS12 EVENT BUILDER

The CLAS12 Event Builder (EB) [53, 56], a final service of the reconstruction package, correlates and organizes all of the information of a physics event reconstructed by the CLAS12 detectors. The EB service collects the global event information in the form of data banks structure [54, 55] from the upstream services, and uses that to tie everything together for an event as shown in Fig. 71. It also executes the particle identification schemes and outputs

resulting information in a standard bank structure. Different CLAS12 sub-systems are used in the particle identification scheme to differentiate the particles in the final event-building process as shown in Fig. 72.

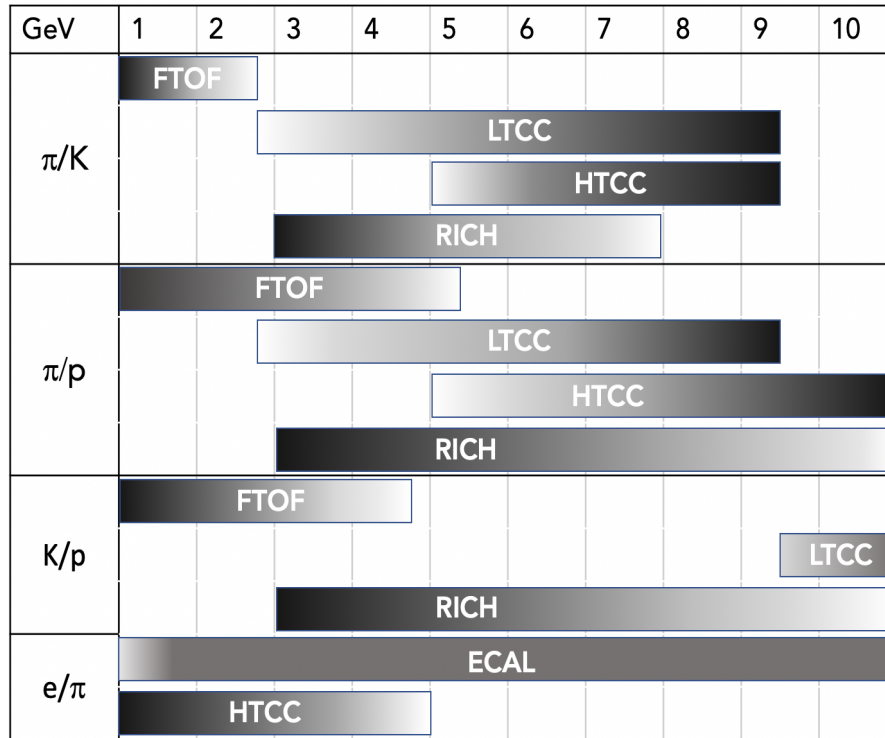


FIG. 72: CLAS12 forward detector to identify and separate the PIDs. Color grading shows the separation power (dark:highest and bright:lowest) in terms of the particle energy [38].

The CLAS12 EB assigns Particle Identification (PID) number as 11 (electron) or -11 (positron) after matching charged particle tracks in the DC and the ECAL cluster with an associated hit in the FTOF, and appending the following HTCC and EC criteria:

1. HTCC photoelectrons ≥ 2.0

2. PCAL energy deposition ≥ 60 MeV
3. 5σ cut on the energy parametrized Sampling fraction

Sampling fraction (SF) of the EC is defined as a fraction of the total energy deposited (E_{dep}) by a particle of certain momentum (P) passing through it. The sampling fraction parameterization is performed using the relation $SF = p_1 \left(p_2 + \frac{p_3}{E_{dep}} + \frac{p_4}{E_{dep}^2} \right)$ [54] where p_1 , p_2 , p_3 and p_4 are associated parameters.

The CLAS12 EB assumes other charged particles, that do have TOF hit, but do not satisfy the above criteria, as hadrons ($\pi/K/p$) based purely on timing information. This is based on minimizing the difference between the vertex time and the event start time [53, 54]. The PID number for (π, K, p) in the particle data bank assigned by the CLAS12 EB are $\pm 211, 321, 2212$, respectively.

EB outputs in HIPO format containing event-specific information such as particle identification and its dedicated values, event helicity, accumulated charge, etc. Physics data analysis is then performed filtering the events with specified final states particles of a nuclear reaction under investigation. Because of the collaboration of different experiments, RG-A data were filtered by various data skims as per the requirement of different groups. TCS-J/psi skim files were created for the di-lepton group to analyze reactions involving TCS as well as J/ψ .

4.3 TCS ANALYSIS FRAMEWORK

TCS is the photo-production of a time-like photon which subsequently decays into a lepton pair ($\gamma p \rightarrow p' \gamma^* \rightarrow p' l^+ l^-$). As real photon beams are presently unavailable in Hall B, TCS is studied with the electron beams impinging on the liquid hydrogen target [$ep \rightarrow (e') p' l^+ l^-$]. The final state lepton pairs ($l^+ l^-$) of TCS are detected in the CLAS12 Forward detector system, whereas the protons (p') could be detected by the Forward or Central detectors. The kinematics of the scattered electrons is deduced from a missing momentum analysis. In order to ensure a photo-production events, the scattered electrons should have very small scattering angles.

Among the three different available data sets of RG-A (2018 outbending, 2018 inbending and 2019 inbending runs), this preliminary analysis framework is used to analyze 2018 outbending and inbending runs. Distribution of various variables related to this analysis from the 2018 outbending runs are included in the following sections, whereas similar distributions for the 2018 inbending runs are put together in Appendix E.

4.3.1 TCS EVENT SELECTION

Based on the TCS kinematics explained above, we selected events (included plots are from the RG-A Fall 2018 outbending runs) with the following final states explicitly :

- 1 electron(e^-) detected in the Forward detector
- 1 positron (e^+) detected in the Forward detector
- 1 proton (p) detected in the Forward or Central detector

and any other background or accidentals in $ep \rightarrow p'e^-e^+X$.

Final state electron, positron and proton are chosen by selecting the Particle Identification (PID) assigned by the Event Builder (EB) as explained above. The electron-positrons pairs with PID (± 11) should pass the EB condition of number of photo-electrons (≥ 2) which could be observed in Fig. 73. HTCC minimum number of photo-electrons allows to distinguish leptons from pions. The choice of gaseous mixture in the HTCC is made in such a way that the HTCC could effectively distinguish between leptons and pions below 4.9 GeV. TCS final states are lepton pairs, so the role of the HTCC was crucial to minimize pion contamination.

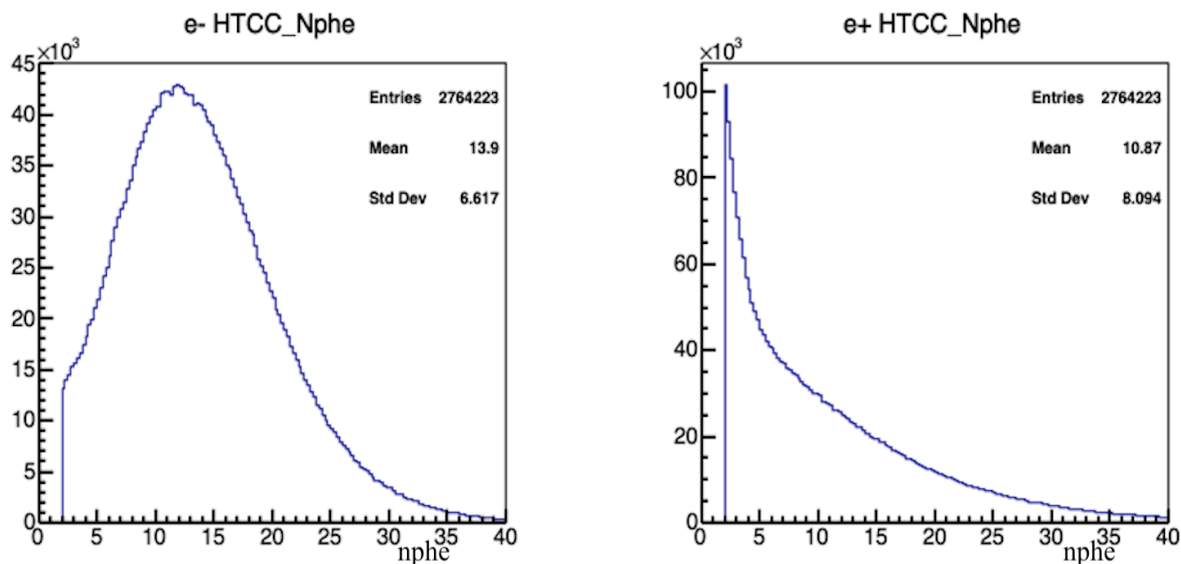


FIG. 73: Event Builder Cut on minimum HTCC photoelectrons required for the identification of electrons (left) and positrons (right).

The additional constraint on EB to assign particles as leptons was a PCAL minimum energy cut, which quantified the basic property of leptons to lose more energy in the pre-shower. More than 60 MeV of energy deposit in PCAL again helped to isolate leptons from hadrons. Figure 74 shows the distribution of energy deposited by electrons and positrons in the CLAS12 Calorimeter system clearly showing the EB cut on PCAL.

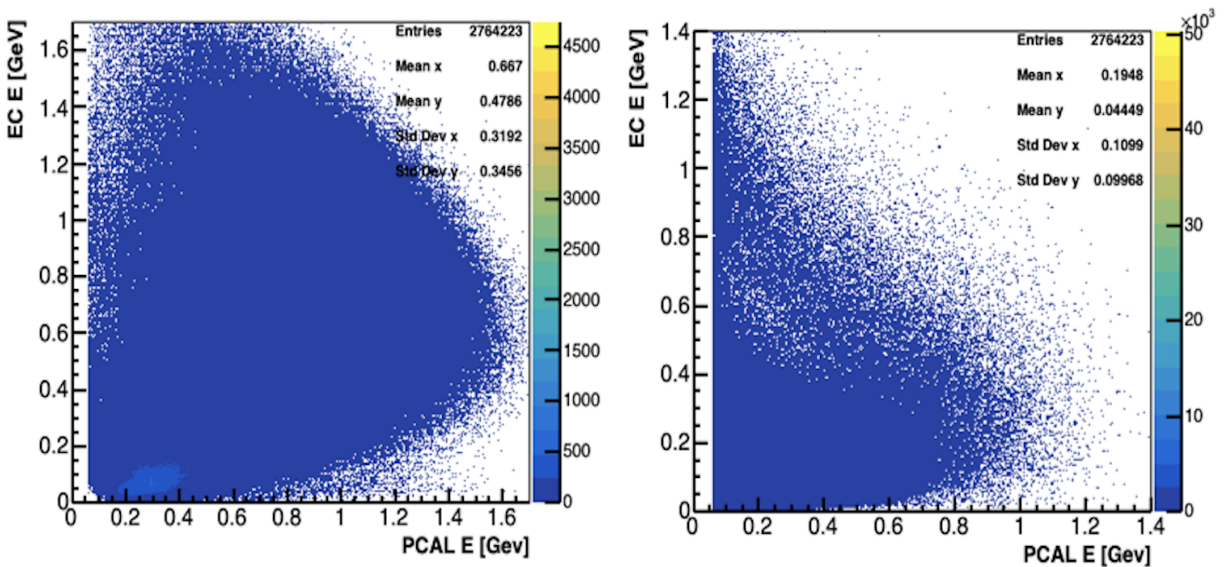


FIG. 74: Energy deposited by electrons (left) and positrons(right) in the Calorimeter showing PCAL energy cut on 60 MeV for leptons.

Furthermore, the 5σ parameterized sampling fraction cut that was utilized in the EB process were written into the particle data bank, which were extracted and plotted in Fig. 75. The sampling fraction distribution with respect to the momentum, showing the upper and lower limit of the sampling fraction accepted by EB, is shown in Fig. 76. This chi2pid provides the information of how close the measured sampling fraction is compared to the expected value, providing us as additional choice for tightening the quality cut of EB particle identification.

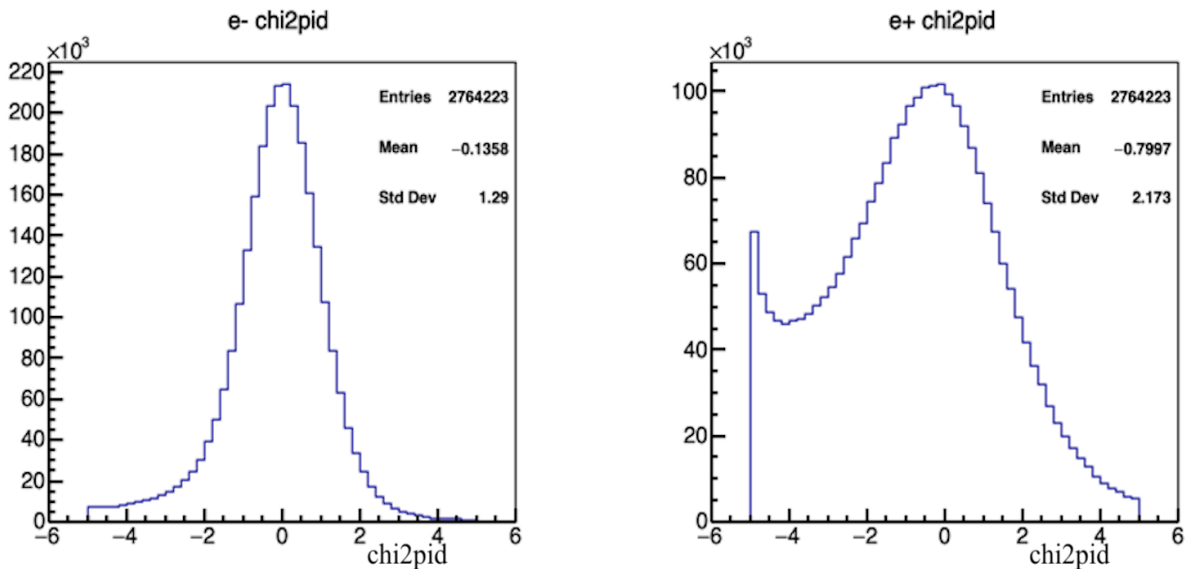


FIG. 75: Quality cut of 5σ on parameterized sampling fraction provided on chi2pid of particle data bank for electron (left) and positron (right).

Even if all the EB criteria were satisfied by the electrons and positrons of the selected TCS events, the distributions of electrons and positrons are not tidy and symmetric. The positron distributions have clusters near the positron-pion separation limit (lower limit of electron distribution in e^\pm HTCC Nphe (Fig. 73), and e^\pm chi2pid (Fig. 75), and higher value of EC Energy at low PCAL Energy in Fig. 74 support the existence of pion contamination in the positron sample. Peak in the number of HTCC photo-electrons and the chi2pid to the lowest threshold limit could be a sign of misidentification of pions as positrons by the EB. Furthermore, the sampling fraction distributions of e^\pm with a long downward tail as shown in Fig. 76 illustrate the inefficiencies of the EB to reconstruct low energy particles accurately. The sampling fraction distributions of positron in each sector also show clusters around 5 GeV positron momentum (towards the lower region of 5σ band), which could be a sign of misidentifying positron/pion after the HTCC threshold of 4.9 GeV. The HTCC is mostly effective to distinguish leptons/pions below this threshold.

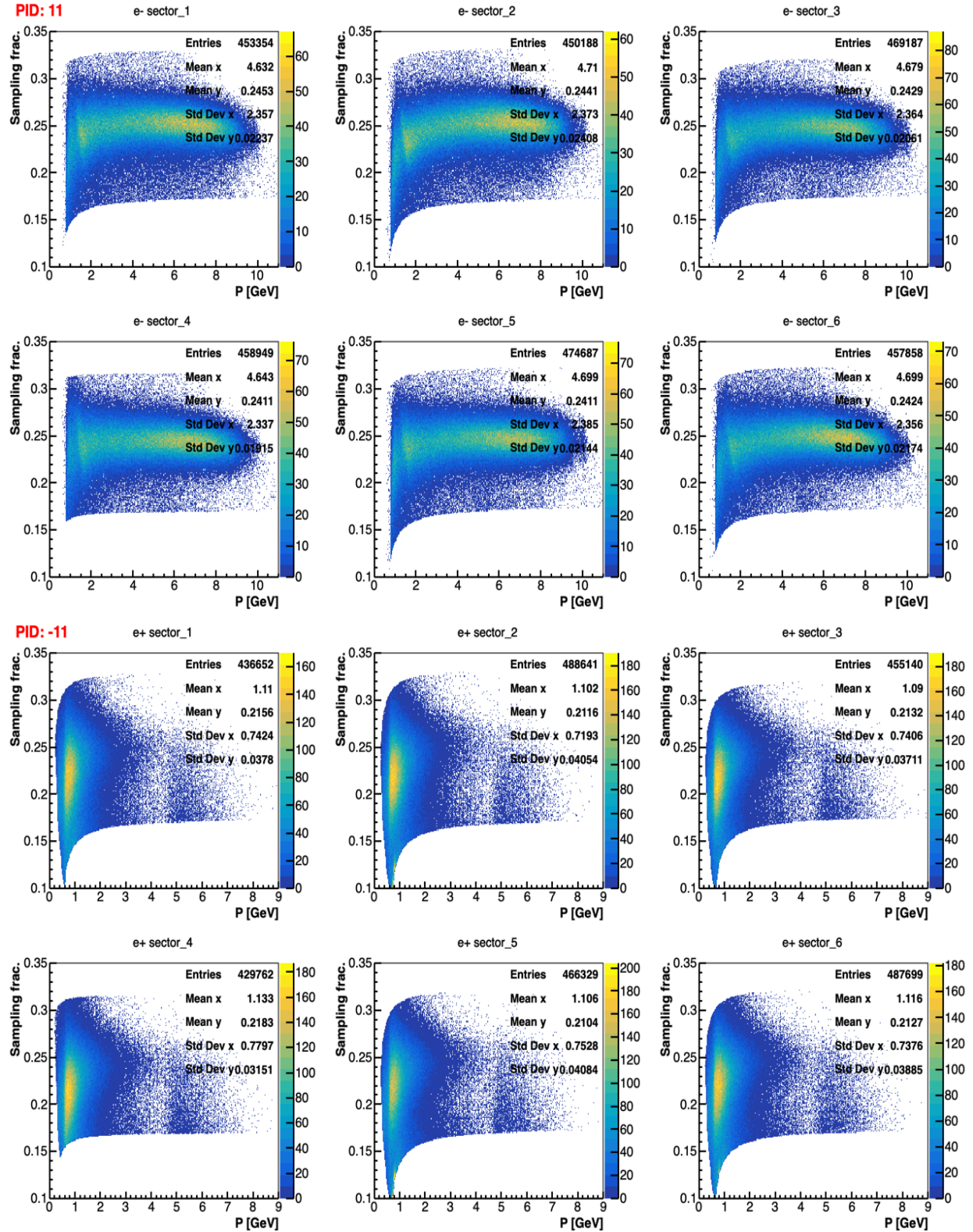


FIG. 76: Sampling fraction distribution of electrons and positrons as a function of momentum in six different sectors of CLAS12 (top: electrons, bottom: positrons).

4.3.2 PID REFINEMENT CUTS

We chose different cuts to remove possible contamination in the selected sample which could be due to the detector geometry and poor reconstruction. The first cut we applied is a fiducial cut on the calorimeter. A particle passing through the calorimeter loses its energy along its path with a distinct energy profile. The electron showers generated by a particle towards the edges of the calorimeter do not account for the full profile because of shower leakage. This insufficient information could lead to mis-reconstruction. To mitigate its effect, a fiducial cut is applied in the PCAL, removing events corresponding to edges of the PCAL, where the sampling fraction drops sharply. In concordance with the RG-A study (common analysis note within RG-A) on the fiducial cut, we chose to implement loose fiducial cuts of 9 cm on lv and lw, and 410 cm cut on lu for leptons. The sampling fraction distribution corresponding to the distance on the three sides of PCAL geometry (lu, lv, lw) are as shown in the Appendix D, which shows that these fiducial cuts would be fine for outbending runs, which we are analyzing now, to remove the outer edge of PCAL that is contributing the shower leakage.

In addition, the events corresponding to the tail of the sampling fraction distribution in Fig. 76 towards the lower momentum region are discarded choosing sampling fraction above 0.16, lower limit of the 5σ sampling fraction band of the energetic leptons. Pions mostly have lower sampling fraction compared to the leptons, so removing the events corresponding to this region, also reduces the contamination of pions within the sample of TCS events.

Furthermore, we added a tighter cut on the quality of PID assignment based on the parameterized sampling fraction by choosing a 4σ cut. This obviously helped to reduce the mis-identified pions in the TCS sample. One more cut was employed in this refinement process to make sure that we further reduce the pion contamination. As pions mostly lose energy in the inner layer of the calorimeter compared to leptons, which lose energy in the pre-shower, we could remove impurities of pions from the ECIN-PCAL sampling fraction correlation as shown in Fig. 77. The scattering data towards the left of the anti-diagonal band is the cause of the lower energy deposition of particles in the PCAL, most probably by pions. This possible contamination is removed by selecting a diagonal cut of $4SF_{ECIN} + 4.5SF_{PCAL} = 0.8$ in the correlation plot. This non-symmetric cut is chosen so that the pion-contamination observed as clusters in the sampling fraction distribution in Fig. 76 above 4.9 GeV could be reduced, but at the same time without further losing leptons below the limit.

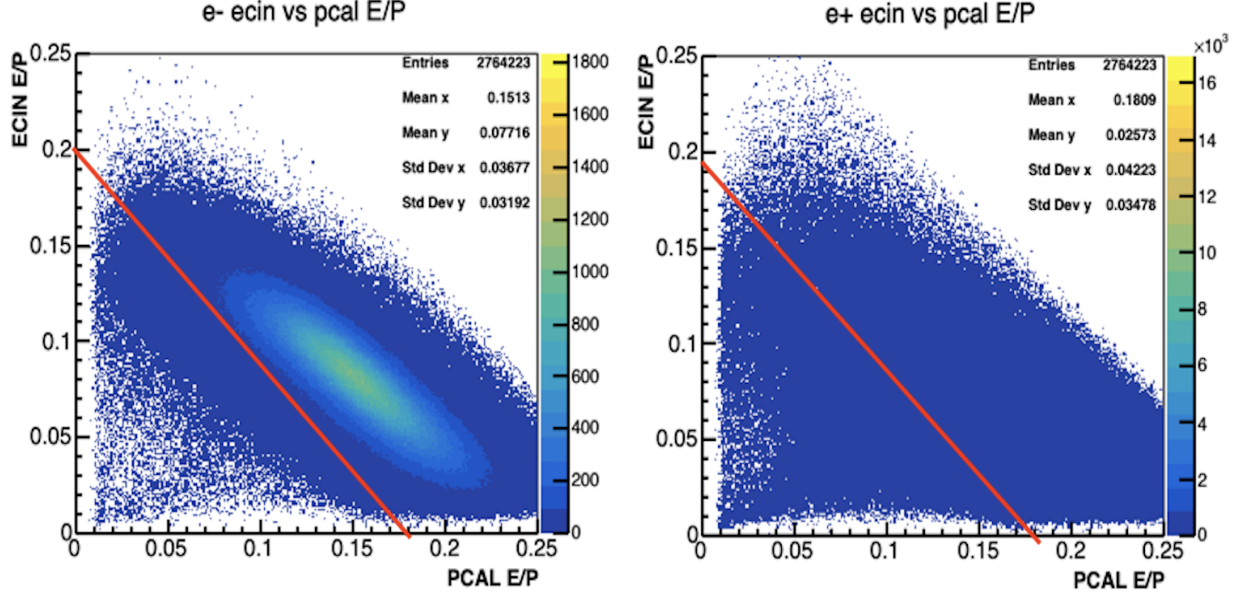


FIG. 77: PCAL and ECIN sampling fraction correlation for electron (left) and positron (right) with red line $4SF_{ECIN} + 4.5SF_{PCAL} = 0.8$ to reject pions.

In addition to all the above cuts on PIDs, we also chose electron-positron pairs in different sectors to diminish possible interference in timing as well as EC cluster during the event reconstruction. After having all these cuts on PID refinement, we chose to scrutinize the sample with TCS kinematics.

4.3.3 TCS KINEMATICS

Events for the TCS analysis are chosen through the reaction

$$ep \rightarrow p'e^-e^+X \quad (23)$$

in which I consider the initial state electron and proton four momentum as $k \equiv (E_e, 0, 0, k_z)$ and $p \equiv (m_p, 0, 0, 0)$; and final state proton, electron and positron four momentum as $p' \equiv (E_{p'}, p'_x, p'_y, p'_z)$, $k_- \equiv (E_-, k_{-x}, k_{-y}, k_{-z})$ and $k_+ \equiv (E_+, k_{+x}, k_{+y}, k_{+z})$, respectively. Now, considering the missing particle four momentum as:

$$k' \equiv (E_{miss}, k'_x, k'_y, k'_z) = (p + k) - (p' + k_- + k_+) \quad (24)$$

the relevant kinematics for the selection of quasi-real photo-production of time-like photon are:

- Missing mass square (m_{miss}^2): Square of the mass of the missing particle

$$k'^2 = m_{miss}^2 \sim 0 \quad (25)$$

- Q^2 of quasi-real photon:

$$\begin{aligned} Q^2 &= (k - k')^2 = (p - p' - k^- - k^+)^2 \sim 0 \\ \implies Q^2 &= 2E_e(|k'| - k'_z) \sim 0 \end{aligned} \quad (26)$$

- Conservation of momentum and Energy:

$$k'_x = -(p'_x + k_x^- + k_x^+) \sim 0 \quad (27)$$

$$k'_y = -(p'_y + k_y^- + k_y^+) \sim 0 \quad (28)$$

$$k'_z + (p'_z + k_z^- + k_z^+) \approx E_{photon}$$

$$m_p + (k'_z + k_z^- + k_z^+) = E_{p'} + E^- + E^+ \quad (29)$$

$$\implies \sum E_{out} - \sum Pz_{out} = m_p \quad (30)$$

where missing transverse momentum $k'_x \sim 0$ and $k'_y \sim 0$ implies $k'_z = E_{miss}$.

Different kinematic variables related with the TCS analysis are plotted as shown in Fig. 78 with all the events that passed the PID refinement cuts. Wide ranges of square of missing mass (MM^2), Q^2 and transverse momentum of missing particle could be clearly observed. So, to satisfy the above mentioned TCS kinematics, we chose the following preliminary cuts in these events to isolate those that pass TCS criteria.

- $|MM^2| \leq 0.4$
- $|k'_x/k'| \leq 0.05$, $|k'_y/k'| \leq 0.05$

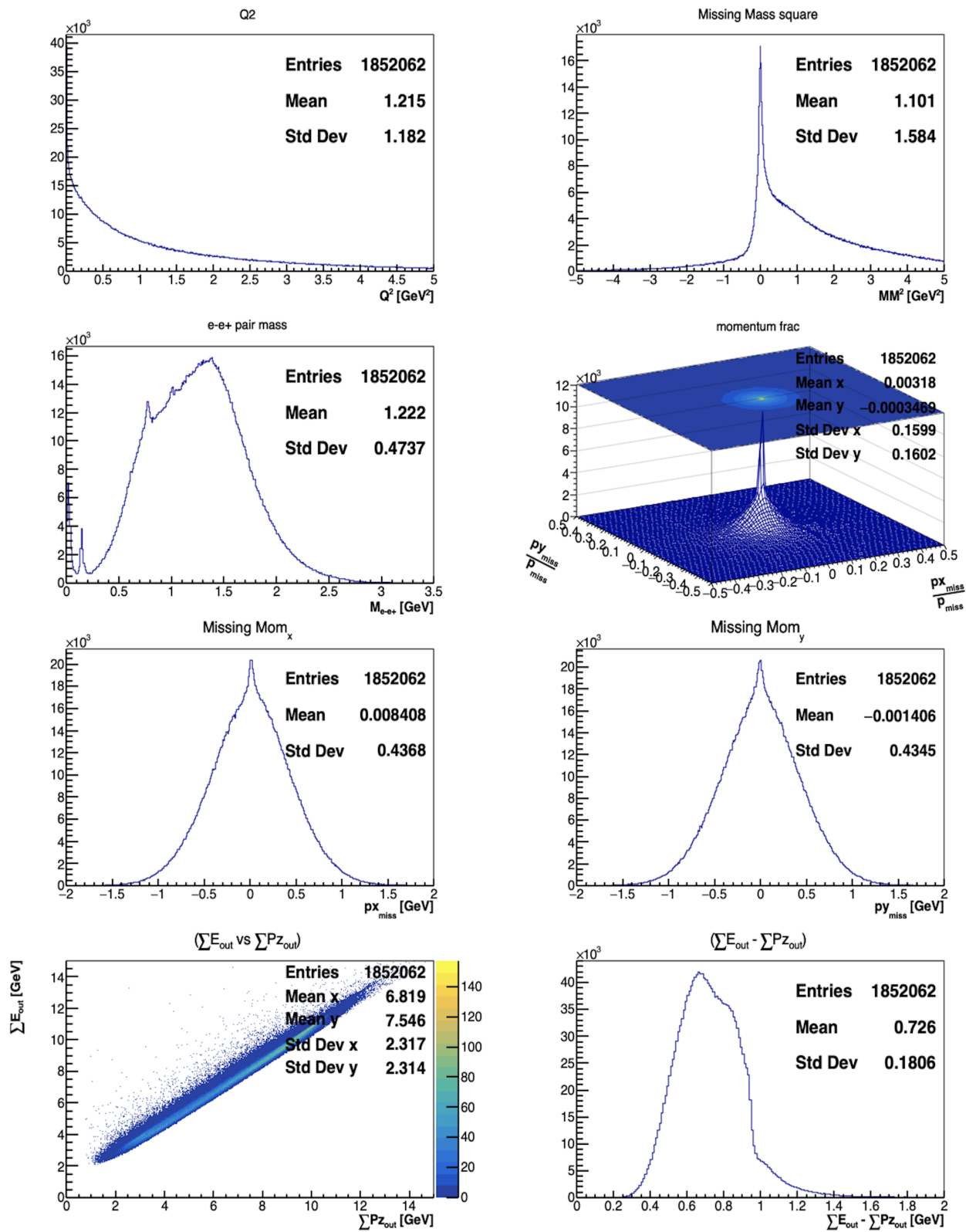


FIG. 78: Distribution of TCS kinematic variables among the sample events before the selected TCS kinematic cut.

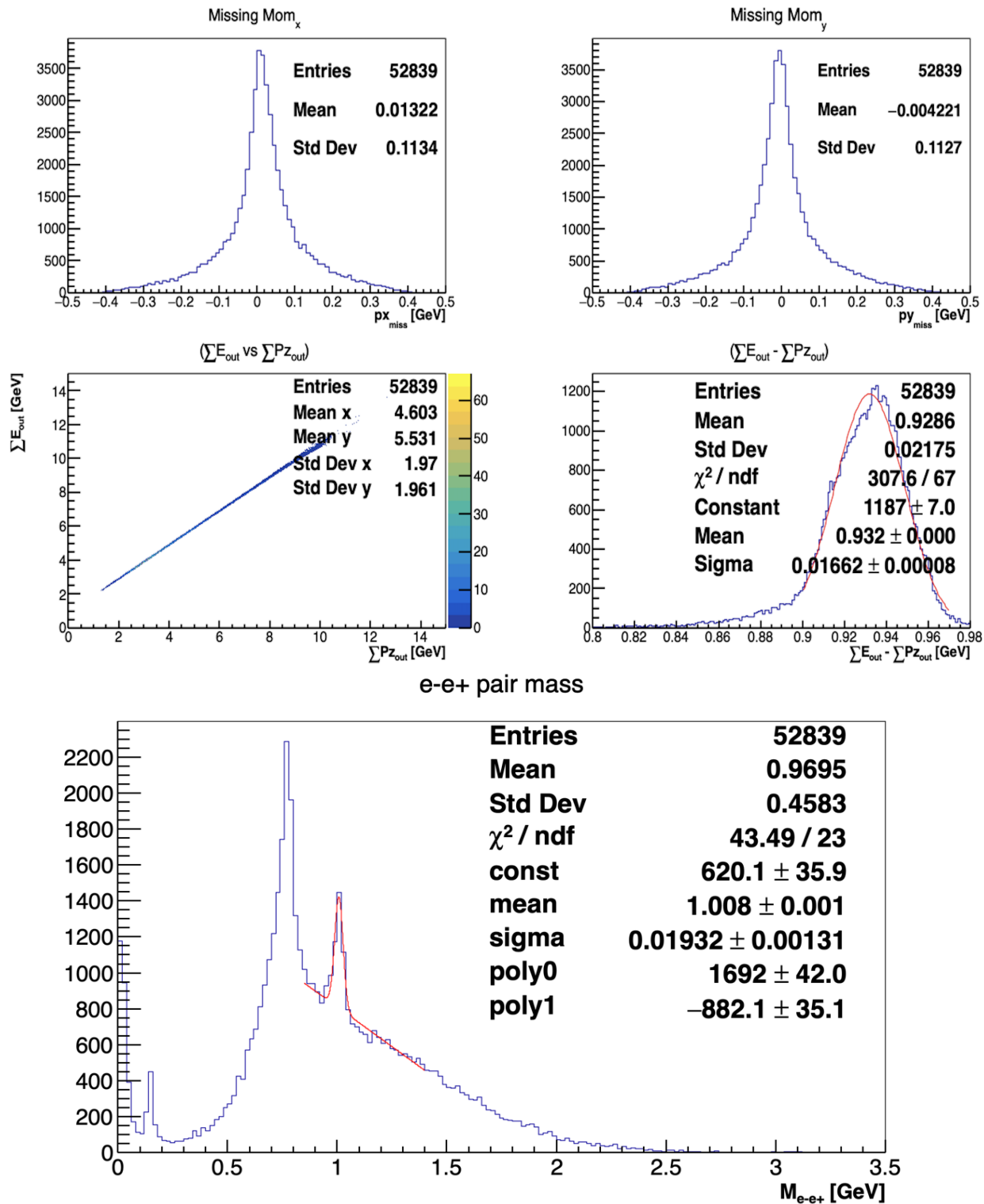


FIG. 79: TCS kinematic variables after the selected MM^2 and transverse momentum cuts.

4.4 TCS OBSERVABLE

To obtain the TCS observable, we selected events beyond the resonance region of electron-positron pairs. In this analysis we particularly chose the region $1.5 \text{ GeV} \leq M_{e^-e^+} \leq 3.0 \text{ GeV}$ in the invariant mass ($M_{e^-e^+}$) distribution shown at the bottom in Fig. 79. In addition to the previous kinematic cuts, the tail of the $(\sum E_{out} - \sum Pz_{out})$, as shown in the mid-right plot of Fig. 79, was also rejected by selecting events with $0.90 \text{ GeV} \leq (\sum E_{out} - \sum Pz_{out}) \leq 0.96 \text{ GeV}$. The physics observable that is obtained from this TCS analysis is the beam spin asymmetry ($A_{\odot U}$) which is calculated using the relation

$$A_{\odot U} = \frac{1}{C} \frac{N^+ - N^-}{N^+ + N^-} \quad (31)$$

where C accounts for the effective polarization of the beam, which is on average $\sim 89\%$ for the 2018 outbending runs and $\sim 86\%$ for the 2018 inbending runs. N^+ and N^- are the number of events with positive and negative helicity, respectively.

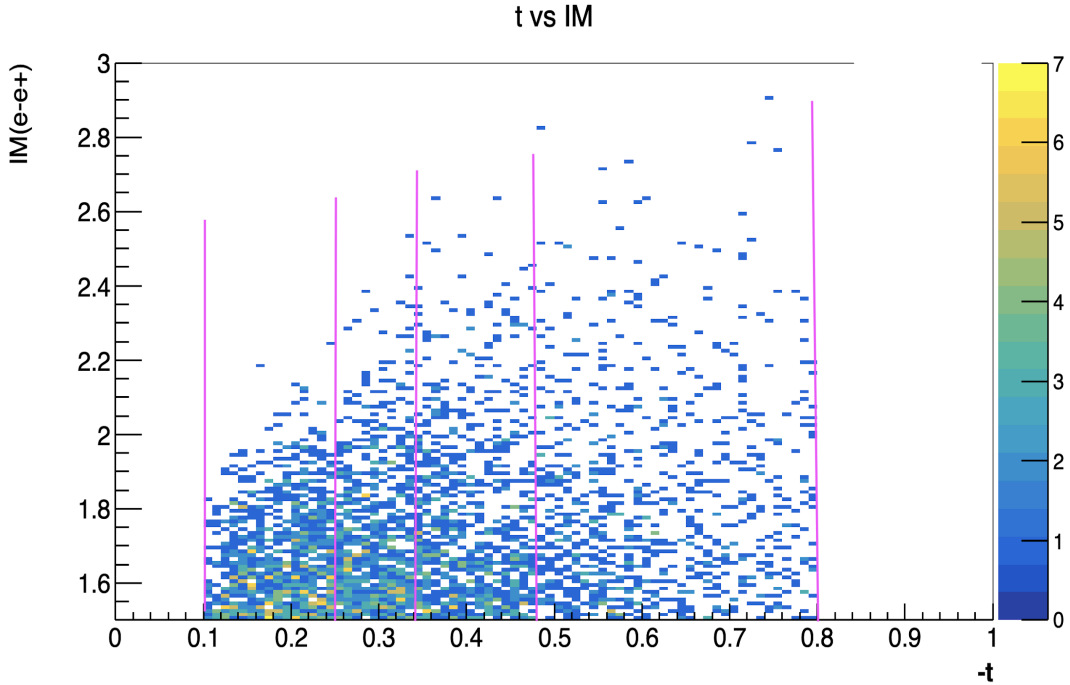


FIG. 80: Distribution invariant mass as a function of t variable and four different t bins to extract BSA.

We selected events within $0.1 \text{ GeV}^2 \leq -t < 0.8 \text{ GeV}^2$ which are further divided into four different $-t$ bins of almost equal number of events to calculate the BSA. Four bins are selected as $0.1 \text{ GeV}^2 \leq -t < 0.25 \text{ GeV}^2$, $0.25 \text{ GeV}^2 \leq -t < 0.34 \text{ GeV}^2$, $0.34 \text{ GeV}^2 \leq -t < 0.48 \text{ GeV}^2$ and $0.48 \text{ GeV}^2 \leq -t < 0.8 \text{ GeV}^2$. The beam spin asymmetry that is extracted from this TCS analysis of the 2018 outbending configuration is shown in Fig. 81. The asymmetry data points are fitted with a sine function and the amplitude of the fit is displayed as ‘ p_0 ’ in each bin. Similar analysis steps and the cuts are followed for the 2018 inbending data as well, and the BSA result of inbending configuration is shown in Fig. 82. (As mentioned previously, the distributions of kinematic variables for the inbending run are kept in Appendix E).

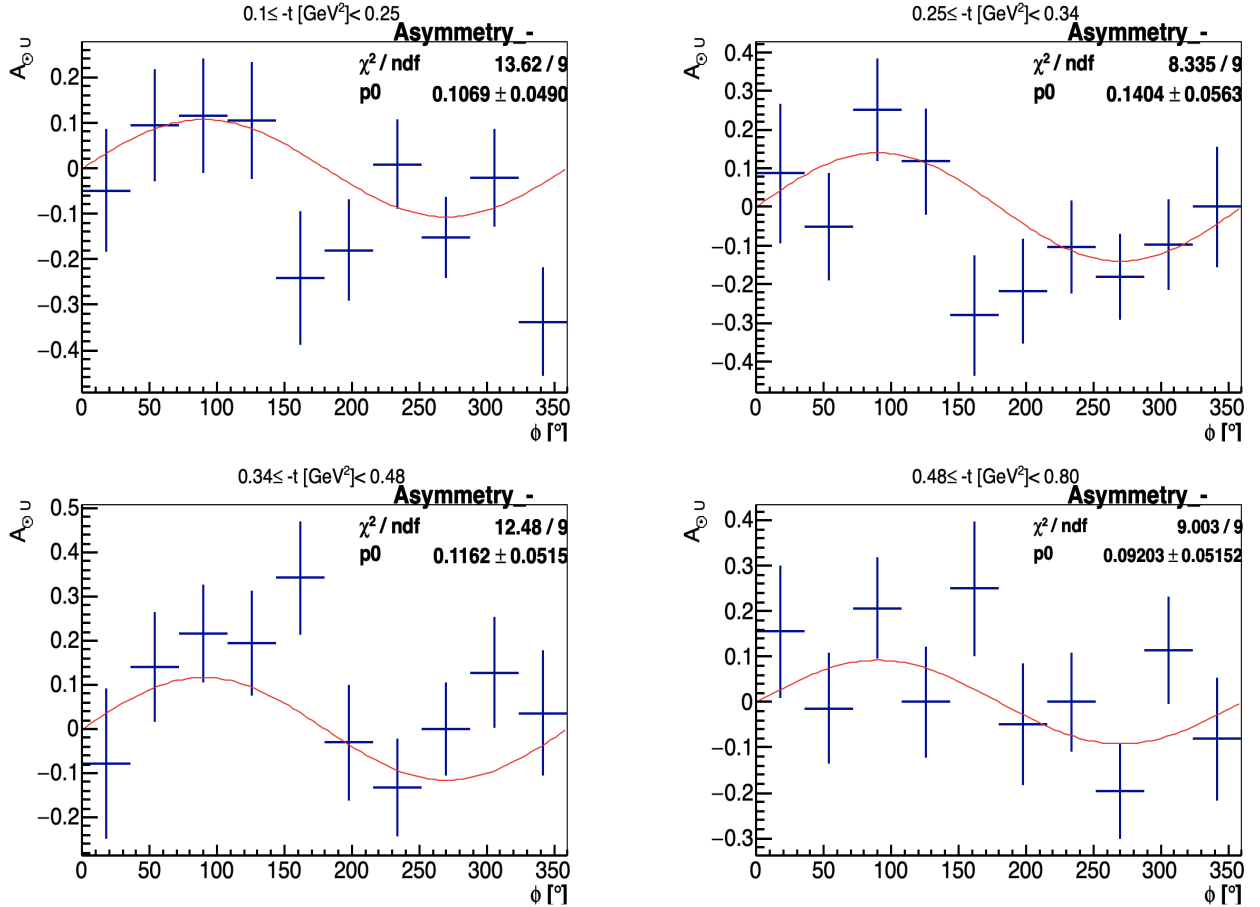


FIG. 81: Beam spin asymmetry calculated using the TCS analysis in various t bins (2018 Outbending run).

The BSA does not depend on the outbending and inbending runs, but our preliminary analysis results (summarized in Table 3) are showing a smaller asymmetry amplitude in the outbending data compared to the inbending in each t bin. This could be because of the efficiency of the particle identification in the CLAS12 system could vary for the outbending and inbending runs because of the change in the path of the charged particles. Various PID refinement cuts that we implemented in this analysis framework are the same for both outbending and inbending runs, which might not be equally effective on both of these data sets. A more rigorous comparison study of two data sets varying different cuts could illustrate the details behind the lower asymmetry and the larger error in the outbending data compared to the inbending. Slight modification in the ranges of the cuts in between two data sets could be more effective to minimize the difference.

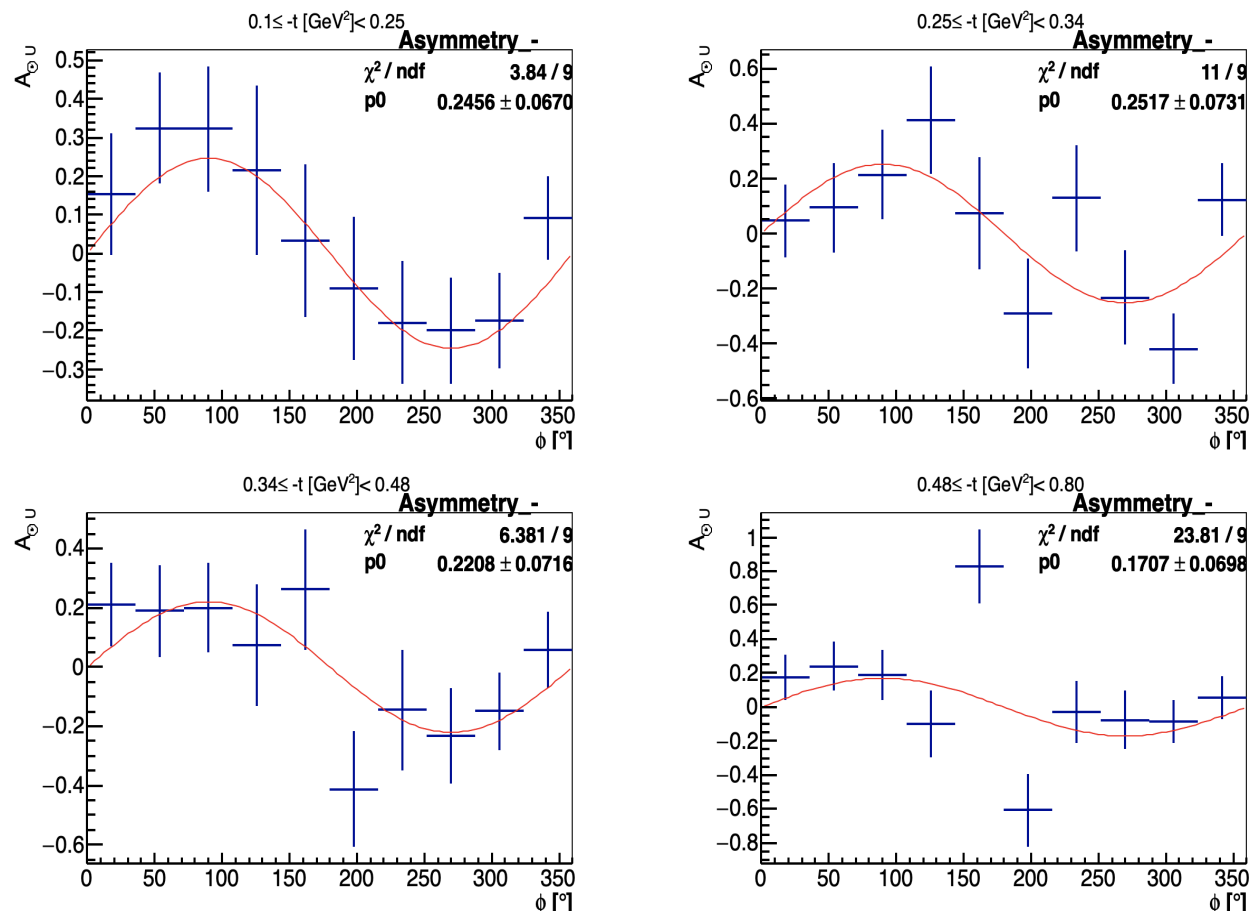


FIG. 82: Beam spin asymmetry calculated using the TCS analysis (2018 Inbending run).

The preliminary BSA results from this analysis is also compared to our recently published result (Fig. 83, taken from Ref. [57]) of the CLAS collaboration (CLAS12 dilepton group) using the RG-A 2018 inbending data. The overall trend of the BSA over t bins that is extracted from this analysis are comparable with the published result. Gentle PID refinement as well as loose kinematic cuts in this preliminary analysis could allow the contamination to infiltrate into our TCS sample altering the final outcome of the BSA. Further detailed study of the particle identification, the energy correction of the final state particles and the stricter cut in the TCS kinematics could lead a better result of asymmetry, lowering the amount of contamination in the selected study samples.

TABLE 3: Summary of preliminary TCS beam spin asymmetry from this analysis of 2018 outbending and inbending runs.

-t bins [GeV ²]	BSA	
	2018 Outbending	2018 Inbending
$0.10 \leq -t < 0.25$	0.107 ± 0.049	0.246 ± 0.067
$0.25 \leq -t < 0.34$	0.140 ± 0.056	0.252 ± 0.073
$0.34 \leq -t < 0.48$	0.116 ± 0.052	0.221 ± 0.072
$0.48 \leq -t < 0.80$	0.092 ± 0.052	0.171 ± 0.070

Furthermore, lower statistics in the individual bins is the reason of the higher error bars in this analysis as well as the published CLAS collaboration result. With a more detailed study of both data sets of 2018 (inbending and outbending) and combined with the 2019 inbending data set, higher statistics of desired TCS events will be accumulated. The higher statistics will allow us to study the asymmetry with significantly reduced errors, and over a smaller bin size. Study of the dependence of the TCS observable with other kinematic variables such as the virtuality (Q'^2) of the timelike photon and the energy of the quasi-real photon (E_γ) could be possible with higher statistics and allow us to constrain its behaviour.

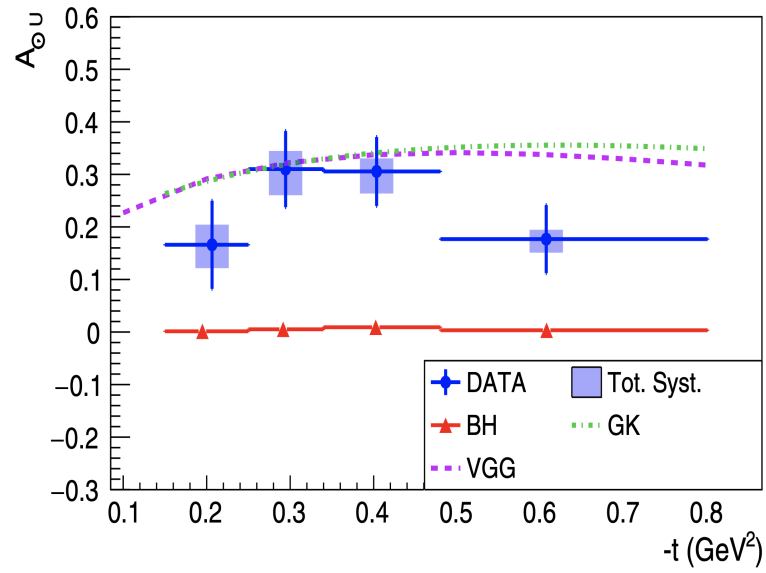


FIG. 83: TCS beam spin asymmetry as a function of $-t$ in the recent publication of CLAS12 with the RG-A 2018 Inbending data comparing with theoretical VGG and GK models [57].

CHAPTER 5

CONCLUSION AND OUTLOOK

5.1 BONuS12 EXPERIMENT

The foremost goal of the BONuS12 experimental group at the beginning of my thesis work was to get ready for the experiment in Hall B of Jefferson Lab and to collect a sufficient amount of high quality data. This required the construction of a new RTPC detector, testing all of its components, integrating with the CLAS12 detector system and monitoring the performances. During that time, simulation and reconstruction software of the RTPC were under development within the BONuS12 group. Designing and construction of the RTPC detector was in the early phase. There were already three graduate students working in these projects, but the group was looking for someone to participate in the hands-on experience of the detector handling and operation. The RTPC data acquisition system had to be tested and to be made available for data taking as well. Motivated by the physics of studying the neutron structure function at large Bjorken- x by using proton tagging technique, I joined the BONuS12 group and got involved in the instrumentation and laboratory work, starting from prototyping of the GEM based detector to the testing and preparing of the DREAM based data acquisition system to the testing of highly pressurized thin foil straws. Our group (Run group F) successfully completed the data taking using the RTPC at Hall B in between February 12 and September 21, 2020, which partly represents the success of our hard work. Calibration and the preliminary data analysis of the BONuS12 data are still ongoing during this thesis writing. I am summarizing below some of the BONuS12 accomplishment we had during my thesis work:

5.1.1 RTPC DETECTOR

Hands-on experience with the GEM based prototype had an immense impact understanding the principles of GEM-based detectors. This allowed us to provide feedback to improve the RTPC design based on the issues we faced in the lab. The skills and expertise acquired during the prototyping of the GEM detector was critical for the handling and operation of the BONuS12 RTPC. The adeptness in the RTPC detector system and its testing procedure

had made us confident to debug the problem in the RTPC and repair it without further complications and damages. The result of our dedicated work for the RTPC detector could be perceived from the individual event track (Fig. 84) that we wanted to collect in this experiment. These tracks were captured from the online CLAS event display (CED) software owned by CLAS collaboration.

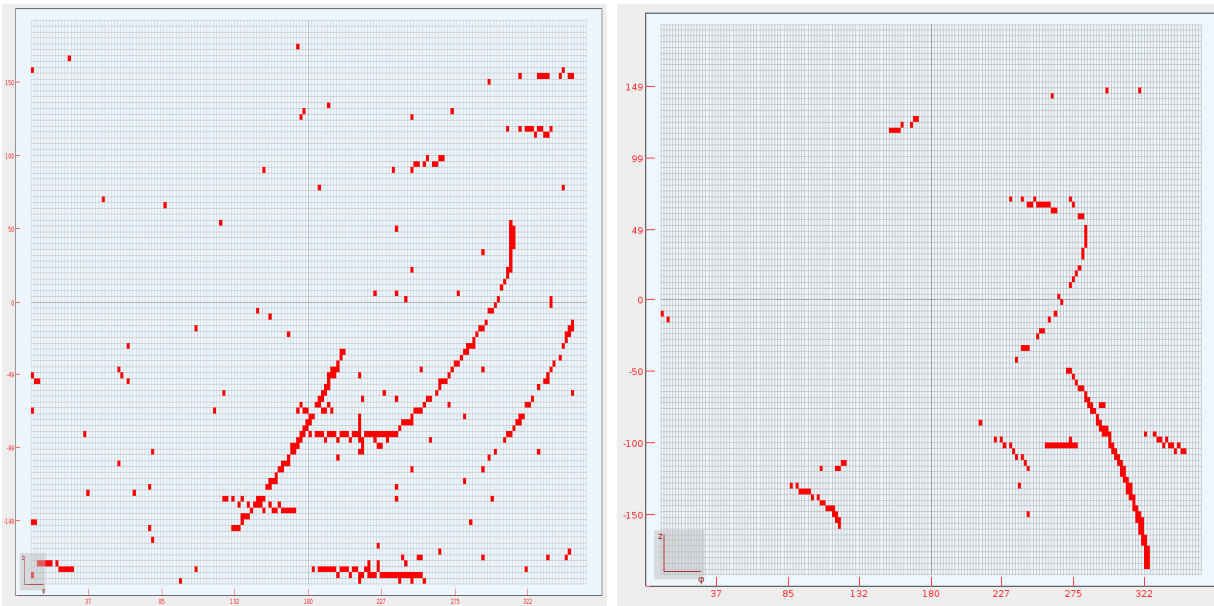


FIG. 84: RTPC tracks visualized in the online CLAS Event Display (CED) gui during the experiment.

Even if RTPC-1 had an electrical failure at the downstream plate, our goal to accumulate sufficient data in the experiment was not compromised that much, completing the RTPC swap much faster than the expected time-frame, without wasting much of our beam time.

5.1.2 BONUS12 TARGET

The BONuS12 target was an extremely delicate part of our experiment maintained under pressure of ~ 68 psig. It was made up of thin Kapton film of $\sim 60 \mu\text{m}$ and can hold almost

double the required pressure. Along with bursting of straws, the leakage from the target was a big concern. Diffusion (two way) of deuterium and helium through the thin wall of the target was also very challenging. The straightness of the straw was another issue. After testing various types of straws, we could not find any straw that satisfied all requirements. Ultimately, we asked a company to produce straws with Kapton foil provided. The first batch needed improvement, but a second production run yielded straws following our requirements. These straws were made from aluminum coated polyimide foil and also perfectly straight. These straws satisfied the Jefferson Lab burst limit as well. As a result of rigorous testing, we did not have target burst issue during the run. The diffusion rate was almost 3 to 4 times less compared to uncoated Kapton straws, which guaranteed a lower contamination of the target gas. The straightness of the target assured proper electron beam alignment of the entire length of the target straw. Observation of the end-cap of the target (Fig. 85) after the experiment clearly indicated that the beam passed through the center of the target without any issue.



FIG. 85: Spot on the target endcap by the irradiation of the electron beam during the first part of the BONuS12 experiment.

5.1.3 BONuS12 DATA ACQUISITION

The BONuS12 experiment took scattering data of about 5.7 billion electron trigger events (Table 2) in the Hall B of the Jefferson Lab, even though the the run was halted for about four months due to the COVID19 shutdown of the lab. The production run was taken with 240 nA electron beam energy. Event rate was somewhat reduced in BONuS12 compared to other experiments using CLAS12. This was due to the trigger inhibition within 10 μ s to readout all the samples of large readout window size of $\sim 7.2 \mu$ s for the RTPC. Almost 90% of the proposed number of events were collected in this experiment which are now available for further analysis to extract the neutron structure function as well as neutron-DVCS (an additional run group proposal to RG-F).

5.2 TIMELIKE COMPTON SCATTERING

Timelike Compton Scattering, an inverse process of DVCS, is a reaction which is well described in leading order and leading twist. This reaction is complementary to DVCS to access the GPDs experimentally. GPDs are widely studied topics in Nuclear and Particle Physics to explore the 3-D tomography of partons within nucleons. I have also been involved in analyzing the CLAS12 RG-A data, in parallel with BONuS12 work, to extract the beam spin asymmetry using TCS events within the CLAS12 di-lepton analysis group. We were successful in constructing an introductory analysis framework to extract preliminary results of the TCS beam spin asymmetry, even though a complete analysis is still in progress. A full analysis with higher statistics and a tight cut on the TCS kinematics would allow us to extract a more precise TCS beam spin asymmetry, which could access the imaginary part of the Compton amplitude in the GPDs formalism.

5.3 OUTLOOK

After the successful completion of data taking, the BONuS12 group is currently looking into the collected data. Calibration of the detectors and adjustment in the CCDB is ongoing. I have also been involved analyzing the BONuS12 data for the energy correction of electrons using π^0 analysis, which will be completed soon. Realistic data simulation and its analysis is underway within the BONuS12 group replicating the various experimental conditions. An RTPC manuscript is already in progress and will be submitted for publication in Nuclear Instruments and Methods, soon.

Furthermore, data collected by CLAS12 RG-A group during 2018 and 2019 are all ready

for analysis now. A preliminary TCS analysis result has recently been published by the CLAS12 di-lepton analysis group using 2018 inbending data, which paved the path to the full TCS analysis. Even if I was mainly focused on the beam spin asymmetry analysis until now, I will continue analyzing the full RG-A data to extract the final result of TCS observables, both real and imaginary part of Compton amplitude. Further improvement of lepton particle identification, particle energy correction, acceptance correction, comparison with the simulated results and the uncertainty/error calculations will be performed in the next phase of full analysis.

BIBLIOGRAPHY

- [1] National Academies of Sciences, Engineering, and Medicine, *An assessment of u.s.-based electron-ion collider science* (Washington, DC, 2018).
- [2] A. Accardi *et al.*, Eur. Phys. J. A **52**, edited by A. Deshpande, Z. E. Meziani, and J. W. Qiu, 268 (2016).
- [3] G. Dodge *et al.*, A New Research Proposal to Jefferson Lab **PAC 23** (2003).
- [4] A. Amarian *et al.*, A 12GeV Research Proposal to Jefferson Lab **PAC 30** (2006).
- [5] M. N. Rosenbluth, Phys. Rev. **79**, 615 (1950).
- [6] S. Tkachenko *et al.* (CLAS Collaboration), Phys. Rev. C **89**, 045206 (2014).
- [7] N. Baillie *et al.* (CLAS Collaboration), Phys. Rev. Lett. **108**, 142001 (2012).
- [8] M. Hattawy *et al.*, A CLAS12 Run-Group Additional Proposal **PAC 47** (2019).
- [9] X. Ji, Phys. Rev. Lett. **78**, 610 (1997).
- [10] A. Radyushkin, Physics Letters B **380**, 417 (1996).
- [11] X. Ji, Phys. Rev. D **55**, 7114 (1997).
- [12] M. Burkardt, Phys. Rev. D **62**, 071503 (2000).
- [13] M. Diehl, Physics Reports **388**, 41 (2003).
- [14] X. Ji, Ann. Rev. Nucl. Part. Sci. **54**, 413 (2004).
- [15] E. R. Berger, M. Diehl, and B. Pire, Eur. Phys. J. C **23**, 675 (2002).
- [16] M. Guidal, H. Moutarde, and M. Vanderhaeghen, Rep. Prog. Phys. **76**, 066202 (2013).
- [17] M. Boër, M. Guidal, and M. Vanderhaeghen, Eur. Phys. J. A **51**, 103 (2015).
- [18] R. Parendyan *et al.*, CLAS Approved Analyses Proposal **CAA-DP09-01** (2009).
- [19] R. Parendyan, “Timelike compton scattering”, Phd Thesis (Yarevan Institute of Physics, 2010).
- [20] I. Albayrak *et al.*, A New Research Proposal to Jefferson Lab **PAC 39** (2012).
- [21] H. Moutarde *et al.*, Phys. Rev. D **87**, 054029 (2013).
- [22] P. Chatagnon, “Nucleon structure studies with clas12 at jefferson lab: timelike compton scattering and the central neutron detector”, Phd Thesis (Universite Paris-Saclay, Oct. 2020).

- [23] F. Sauli, Nucl. Instrum. Meth. A **419**, 189 (1998).
- [24] F. Sauli, Nucl. Instrum. Meth. A **805**, Special Issue in memory of Glenn F. Knoll, 2 (2016).
- [25] F. Sauli, Nucl. Instrum. Meth. A **505**, 195 (2003).
- [26] S. Bachmann *et al.*, Nucl. Instrum. Meth. A **470**, 548 (2001).
- [27] F. Sauli, Nucl. Instrum. Meth. A **522**, 93 (2004).
- [28] F. Sauli, Nucl. Instrum. Meth. A **580**, 971 (2007).
- [29] H. Fenker *et al.*, Nucl. Instrum. Meth. A **592**, 273 (2008).
- [30] N. Dzbenski, “Simulation and development of the radial time projection chamber for the bonus12 experiment in clas12”, PhD Thesis (Old Dominion University, May 2020).
- [31] A. Acker *et al.*, Nucl. Instrum. Meth. A **957**, 163423 (2020).
- [32] P. Baron, E. Delagnes, C. Flouzat, and F. Guilloux, *Dream, a front end ASIC for clas12 detector (user’s manual)* (2014).
- [33] D. Attie *et al.*, in 2014 19th IEEE-NPSS Real Time Conference (2014), pp. 1–11.
- [34] I. Mandjavidze, *Feu: a frontend unit for micromegas trackers (user’s manual)* (2016).
- [35] S. Boyarinov *et al.*, Nucl. Instrum. Meth. A **966**, 163698 (2020).
- [36] D. Payette, “Spectator proton detection and reconstruction in deep inelastic d(e,eps) scattering”, PhD Thesis (Old Dominion University, May 2021).
- [37] C. W. Leemann, D. R. Douglas, and G. A. Krafft, Ann. Rev. Nucl. Part. Sci. **51**, 413 (2001).
- [38] V. D. Burkert, Ann. Rev. Nucl. Part. Sci. **68**, 405 (2018).
- [39] C. H. Rode, in AIP conference proceedings, Vol. 1218, 1 (2010), pp. 26–33.
- [40] R. D. McKeown, in Journal of physics: conference series, Vol. 312, 3 (Sept. 2011), p. 032014.
- [41] R. Fair *et al.*, Nucl. Instrum. Meth. A **962**, 163578 (2020).
- [42] G. Asryan *et al.*, Nucl. Instrum. Meth. A **959**, 163425 (2020).
- [43] D. Carman *et al.*, Nucl. Instrum. Meth. A **960**, 163629 (2020).
- [44] M. Ungaro *et al.*, Nucl. Instrum. Meth. A **957**, 163420 (2020).
- [45] M. Contalbrigo *et al.*, Nucl. Instrum. Meth. A **964**, 163791 (2020).

- [46] M. Mestayer *et al.*, Nucl. Instrum. Meth. A **959**, 163518 (2020).
- [47] Y. Sharabian *et al.*, Nucl. Instrum. Meth. A **968**, 163824 (2020).
- [48] S. Niccolai *et al.*, Nucl. Instrum. Meth. A **904**, 81 (2018).
- [49] D. Carman *et al.*, Nucl. Instrum. Meth. A **960**, 163626 (2020).
- [50] M. Antonioli *et al.*, Nucl. Instrum. Meth. A **962**, 163701 (2020).
- [51] N. Baltzell *et al.*, Nucl. Instrum. Meth. A **959**, 163421 (2020).
- [52] B. Raydo *et al.*, Nucl. Instrum. Meth. A **960**, 163529 (2020).
- [53] V. Ziegler *et al.*, Nucl. Instrum. Meth. A **959**, 163472 (2020).
- [54] *Clas12 dsts*, Online; access March 2022, https://clasweb.jlab.org/wiki/index.php/CLAS12_DSTs.
- [55] *Clas12 related data banks*, Online; access March 2022, <https://github.com/JeffersonLab/clas12-offline-software/blob/development/etc/bankdefs/hipo4/event.json>.
- [56] *Clas12 event builder*, Online; access March 2022, https://clasweb.jlab.org/wiki/index.php/CLAS12_EventBuilder.
- [57] P. Chatagnon *et al.* (CLAS Collaboration), Phys. Rev. Lett. **127**, 262501 (2021).

APPENDIX A

PEDESTALS COMPARISION OF FEUS

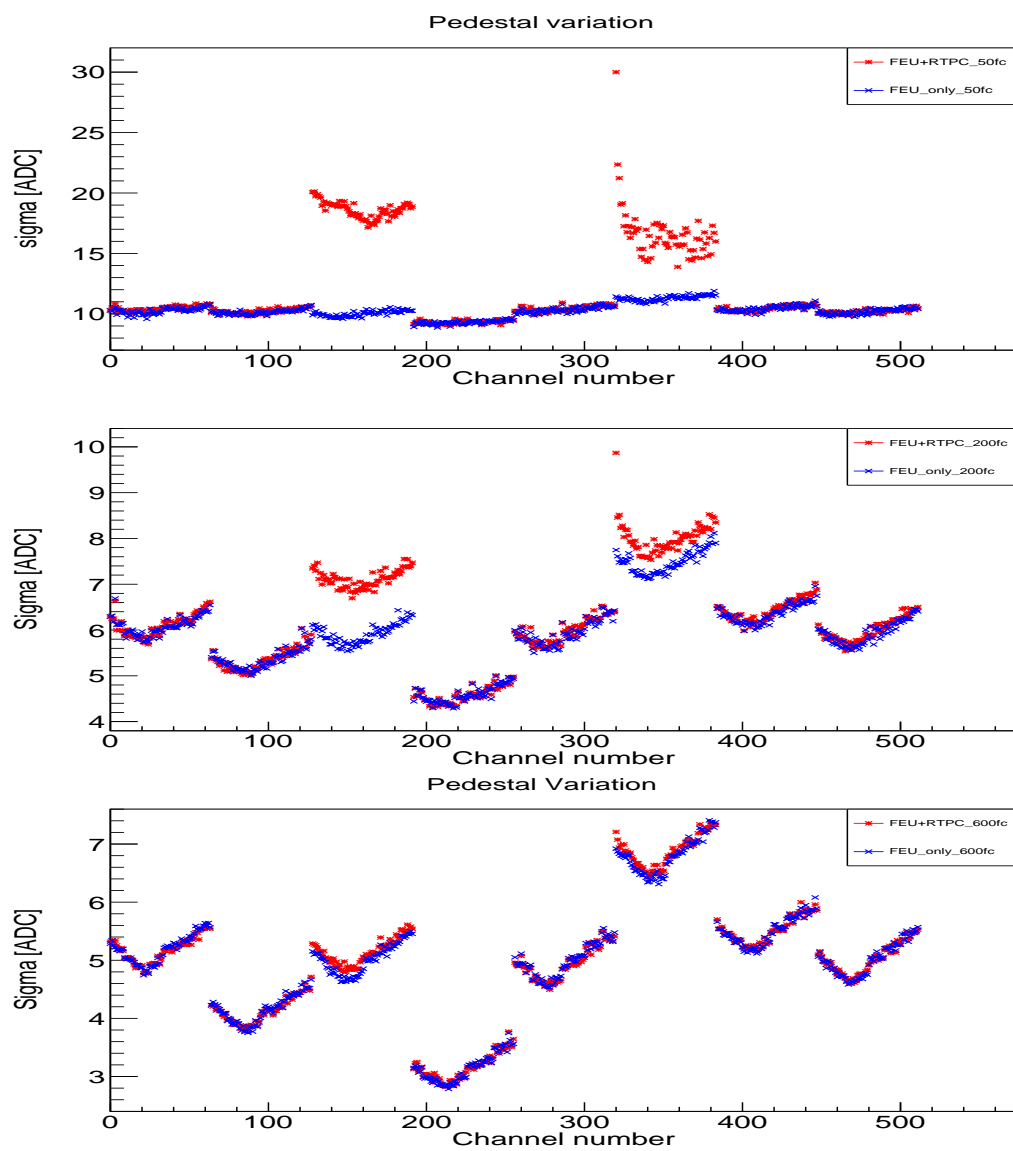


FIG. 86: Pedestal study of the FEU with the change in the gain capacitance as indicated in the right corner of plot.

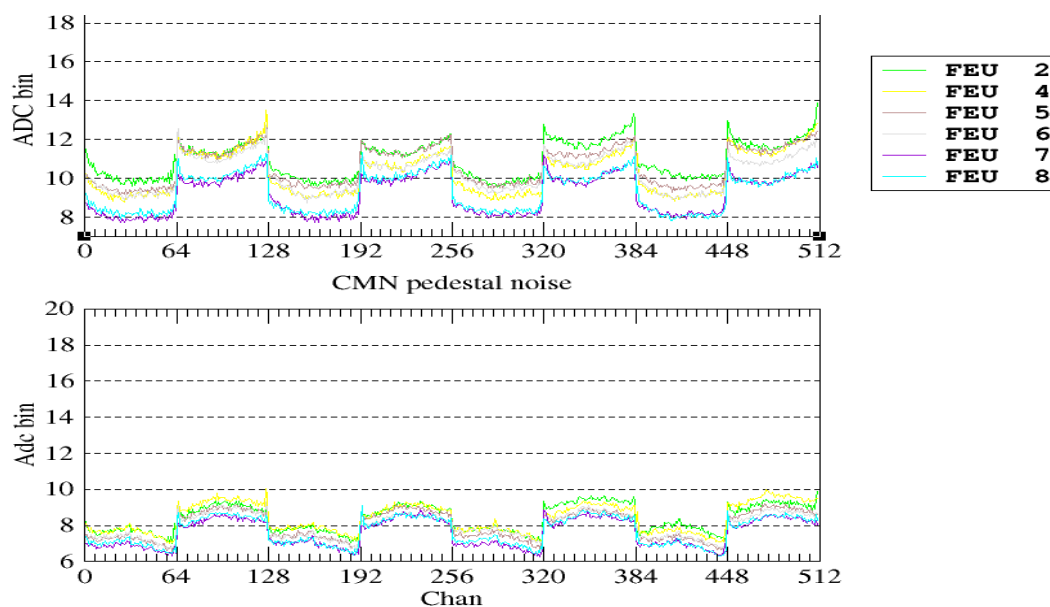


FIG. 87: Pedestal noise analysis during the the cosmic test at the Jlab testbench consisting of six FEUs.

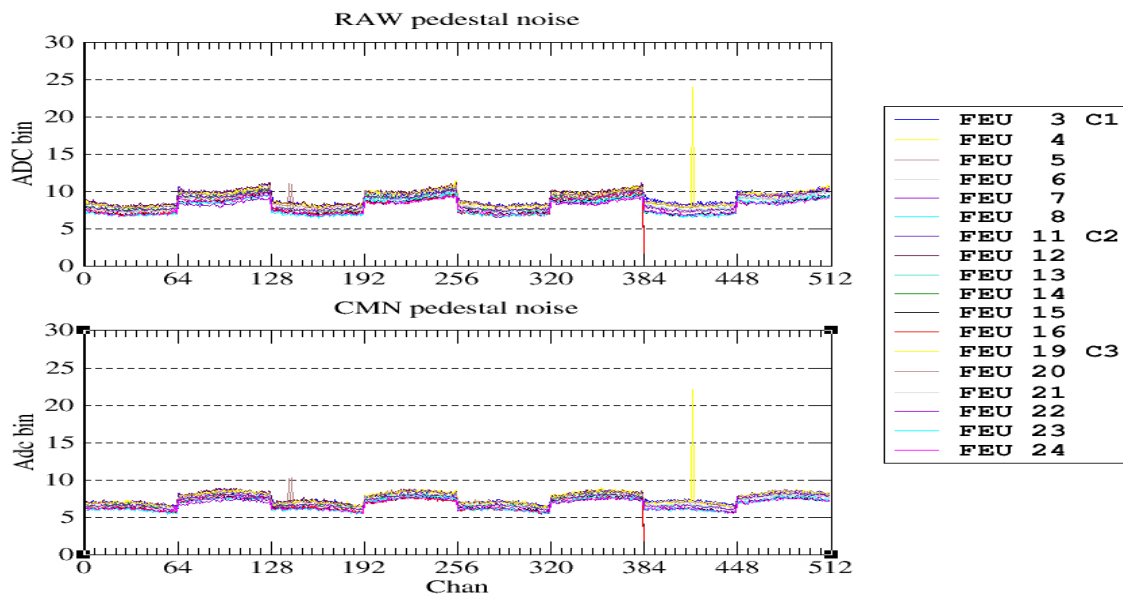


FIG. 88: Pedestal noise of the RTPC in the hall (FEU crates 1, 2 and 3).

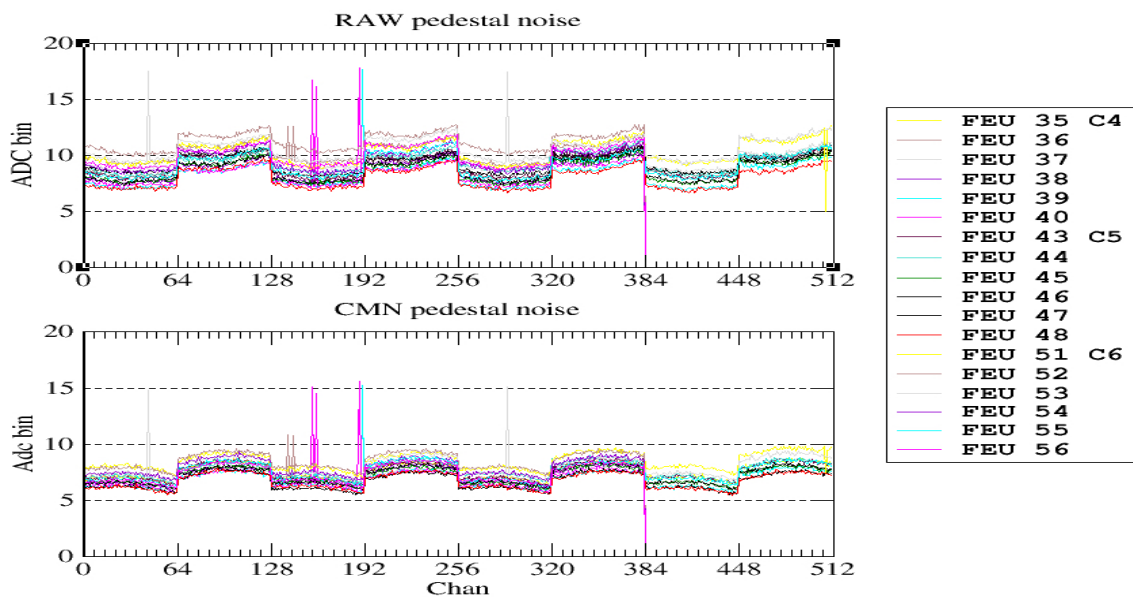


FIG. 89: Pedestal noise of the RTPC in the hall (FEU crates 4, 5 and 6).

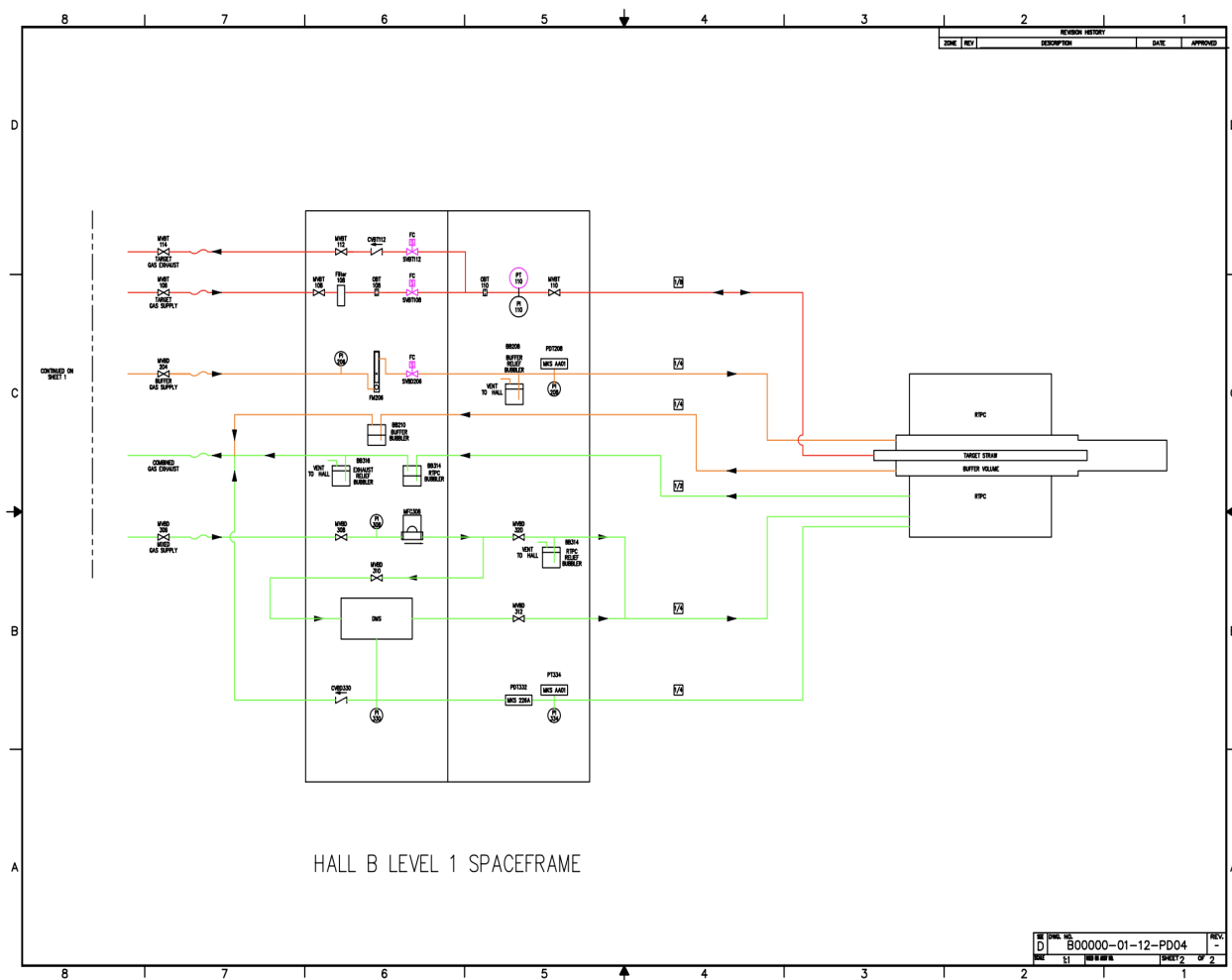


FIG. 91: BONuS12 gas system for both RTPC and Target (Inside the hall).

APPENDIX C

COMMANDS AND CONFIGURATION FOR FEU

Standalone DAQ Commands:

While collecting data using DREAM, we need to specify the configuration file (configfile.cfg). A typical configuration file of the DREAM Electronics, appended in this documentation, has different parameters which could be changed according to the need of an experiment. Before describing the details of these parameters, I would like to describe some commands to run the DAQ.

(I) Pedestal Run:

- (i) To run the data acquisition in the command line, we should use following command inside a directory where the Feu executional files are placed:

```
../FeuUdpControl -a 0x2 -c ped.cfg -f pedestal
```

In this command, **-a** is used to declare the number of ‘active FEU’s’ in hex format, **-c** for the ‘configuration file’ to be used, and **-f** for the output file name (prefix) respectively. Make sure that the configuration file has all the relevant parameters for your run. In addition, we can also fix the number of events; for example appending **-n 100** in the above command collects the first 100 events only (that means it processes first 100 triggers only). Above command generates a new screen where the number of triggers processed can be visible.

The **ped.cfg** is a configuration file, which is used to allocate the different parameters required for the particular run. The parameters are described in next section. Make sure that the FEU ID and IP address are correct (See Parameter section to put right ID number and the address).

When the new screen appears, press **shift+i** (upper case I) to initialize the local parameters in the configuration file and then press **shift+g** (upper case G) to start accepting/processing the trigger. Now, the number of triggers processed and the elapsed time can be seen on the screen. To stop the trigger processing, press **g** (lower case g) and to go back from the screen to command line, press **shift+q** (upper case Q). If you didn’t see the increment of processed triggers, DREAM

doesn't collect any data, so you will have 0 byte output file. If it happens, recheck your trigger source in the configuration file used and try it again. Output file of the above command looks like:

pedestal_YYMMDD_HHMM_000_01.fdf.

Sometimes, you might get empty (0 Kb) data file (*.fdf) after this run, which means there was a problem running the program and no data is saved on that run. If so, make sure all the parameters of configuration file are adequate and run again to check the problem is fixed or not. If this problem persists while taking data in linux platform, it could be due to the incompatibility of the config file. If you tried to run the program after changing some parameters in the config file or you tried a new config file obtained from outside source, there could be conflict to run the config file which might have prepared in windows platform. Anyway it is good to check the new config file in linux machine using command: **dos2unix config.cfg** which makes the config file compatible to linux. Once you do this, you can change the parameters in the config file as many times as you want without using this command again for that file. Some other problem might be due to firewall of computer which could have changed if the computer is restarted. If so and you are using linux machine, you can use command such as: **sudo /etc/init.d/iptables save** and after that **sudo /etc/init.d/iptables stop** to change the firewall state.

Along with this file, we also get **pedestal_YYMMDD_HHMM.cfg** file with the same name as output filename, which summarises the parameters used for that particular run. This file helps to confirm the parameters that are used for that particular run, which we can view any time later.

- (ii) To convert the **pedestal_YYMMDD_HHMM_000_01.fdf** file into readable text file, use the following command:

```
../FeuDataFileReader -p 256 pedestal_YYMM...000_01.fdf
```

Output will be **pedestal_YYMMDD_HHMM_000_01_ped.aux** which can be viewed using text editor. Along with this, there will be another file **pedestal_YYMMDD_HHMM_000_01_ped.prg** useful for pedestal subtraction (this will be described latter) in configuration file.

(II) Self Trigger Run:

- (1) To run the data acquisition in the command line, we should use following command inside a directory where the Feu executational files are placed:

```
../FeuUdpControl -a 0x2 -c Self_trig.cfg -f Slftrig
```

As mentioned above, **-a** is used to declare the number of ‘active FEU’s’ in hex format, **-c** for the ‘configuration file’ to be used, and **-f** for the output file name (prefix) respectively. Make sure that the configuration file has all the relevant parameters for your run. In addition, we can also fix the number of events; for example appending **-n 100** in the above command collects the first 100 events only (that means it processes first 100 triggers only). Above command generates a new screen where the number of triggers processed can be visible.

The **Self_trig.cfg** is a configuration file, which is used to allocate the different parameters required for the particular run. The parameters are described in next section. Make sure that the FEU ID and IP address are correct (See Parameter section to put right ID number and the address). For self trigger, the global threshold should also be matched in the register 1 of the DREAM configuration (will be discussed in the next section).

When the new screen appears, press **shift+i** (upper case I) to initialize the local parameters in the configuration file and then press **shift+g** (upper case G) to start accepting/processing the trigger. Now, the number of triggers processed and the elapsed time can be seen on the screen. To stop the trigger processing, press **g** (lower case g) and to go back from the screen to command line, press **shift+q** (upper case Q). If you didn’t see the increment of processed triggers, DREAM doesn’t collect any data, so you will have 0 byte output file. If it happens, recheck your trigger source in the configuration file used and try it again.

Output file will be:

```
Slftrig_YYMMDD_HHMM_000_01.fdf
```

- (2) To convert the **Slftrig_YYMMDD_HHMM_000_01.fdf** file into readable file (ascii file format readable in text editor), use the following command:

```
../FeuDataFileReader -A Slftrig_YYMM....000_01.fdf
```

Note: The conversion of **output_file.fdf** into another format can be done only for a particular number of events, starting from any event number. It is done by an addition of **-f N1 -l N2** in the above command which converts binary file into a desired output format starting from event N1 and ending at N2.

- (3) To convert the **Slftrig_YYMMDD_HHMM_000_01.fdf** file into inbuilt event display, use the following command:

```
../FeuDataFileReader -D 1 Slftrig_YYMM...000_01.fdf
```

Output will be **Slftrig_YYMMDD_HHMM_000_01.dsp**

- (4) View events from *.dsp file using command:

```
../FeuEvtDisp Slftrig_YYMMDD_HHMM_000_01.dsp.
```

Use **shift+e** (upper case E) to increase event number and use **shift+c** and **c** (upper case C and lower case c) to view events channel by channel.

(III) External trigger run:

- (i) To run the data acquisition, we should use following command inside a directory where the Feu executional files are placed:

```
../FeuUdpControl -a 0x2 -c Ext_trig.cfg -f Exttrig
```

The **Ext_trig.cfg** is the configuration file for the use of External trigger. For this we need a TTL signal which is sent to the TCM (Trigger Control Module) and trigger is distributed from TCM to FEUs using JTAG cables.

All the other procedures remains same as in Self trigger run, so use the previous page to proceed further.

- (IV) Various options related to different commands can be viewed using help command which appears if used -h, for example **../FeuUdpControl -h ../FeuDataFileReader -h ../FeuEvtDisp -h** It shows all the options corresponding to the commands 'Feu-UdpControl', 'FeuDataFileReader', and 'FeuEvtDisp'.

Commands within the CLAS12 system:

After logging to the CLAS12 server, the following commands are used inside /mvt/CodaScripts/ directory for FEU related data.

- **MvtRunBatchCol:** This was a bash script which was widely used for the pedestal run with following options

MvtRunBatchCol PEDRUN ./mvt2crates_bonus 500 DEBUG

As BONuS12 used large samples during data taking, it **MvtRunBatchCol** was modified to **MvtRunBatchCol_HR** making a default 16 samples events of the pedestal run, bypassing numbers in configuration file. With PEDRUN option, it automatically took data, produced pedestal and threshold files for zero suppression, including all necessary channel masking. As two crates (mvt1 and mvt2) are used for BONuS12, configuration for both crates FEUs are included in mvt2crates_bonus.cfg. This can be observed by the opening of two new windows right after the above command. Another option, number of events could be any, based upon the detector and noise. DEBUG option prevented the final clean up after pedestal analysis, allowing to observe details in console output. PEDRUNSET option was used during data taking, because it prepared a new configuration file ready for CLAS12 CODA data taking by updating the information and copying pedestal and zs files to \$CLONPARMS/mvt/.

Instead of PEDRUN, DATRUN was used for initial data taking before integrating to the CODA framework.

- **MvtCompFileReader:** This was also a bash script which was used to convert the evio file from JLab to fdf file after which standalone utilities for the FEU mentioned above could be used. It was used like: **MvtCompFileReader -F *.evio** where *.evio is a file obtained from CLAS12.
- **FeuDataFileReader and FeuEvtDisp:** Details using of both of these are mentioned above, and these were used for the same purpose as above.

FEU and DREAM Configuration Parameters:

(a) Feu ID and IPs

Feu 1 Feu_RunCtrl_Id	18
Feu 1 NetChan_Ip	192.168.10.30

Feu 1 at the beginning both lines implies the first FEU (Front End Unit). If more than one FEU are used, we have to add other lines based on number of FEUs used eg

Feu 2, Feu 3 etc. The number 18 for `Feu_RunCtrl_Id` is the number present at the front of every FEU. So if another FEU is used, we first need to find the number present at the front top part of corresponding FEU and have to used same number here.

`NetChan_Ip` has always 192.168.10. same, however the last number will depend on previous line. We need to add 12 to `Feu_RunCtrl_Id` number to get the Ip address, so here 30 (12+18).

(b) Trigger Interface/Generator configuration

```

Feu * Trig_Conf_Rate           0
Feu * Trig_Conf_Src           Tg_Src_ExtSyn
Feu * Trig_Conf_TrigPipeLen    1
Feu * Trig_Conf_TrigVetoLen    500
Feu * Trig_Conf_File           None

```

`Feu *` at the beginning of every line is used to configure the particular parameter in all the active FEUs.

Note: We can also change configuration parameters of a particular FEU by changing `*` with the corresponding FEU number 1, 2 This could be done by adding one more parameter line below the corresponding line with `*`.

`Trig_Conf_Rate` is the rate of trigger generation based on the trigger source selected on `Trig_Conf_Src` parameter. For example if the `Trig_Conf_Src` is `Tg_Src_Constant`, rate could be 0, 1, 10 or 100 Hz depending on Rate parameters: 0,1,2 or 3 respectively.

`Trig_Conf_Src` allows to choose a trigger source among 8 different sources: In the prototype detector (RTPC), we have used three different `Trig_Conf_Src` parameters `Tg_Src_NegExp`, `Tg_Src_PushBotton` and `Tg_Src_ExtSyn` in the RTPC prototype. Initially, `Tg_Src_NegExp` was used to study the pedestals. Then `Tg_Src_PushButton` was used to study the signal with some arbitrary threshold for the generation of Self-trigger. This parameter is utilized with a Sr^{90} source as well as cosmic radiation. The other parameter, `Tg_Src_ExtSyn` was used to study cosmic signals and calculate drift-time. Signal corresponding to cosmic was obtained using scintillator which is then converted to TTL ($\sim +3\text{V}$) signal. This signal was directly sent to FEU service board along with the `Tg_Src_ExtSyn` parameter in configuration file.

Tg_Src_Int : Input from FPGA logic **Tg_Src_ExtAsyn** : External Asynchronous signal
Tg_Src_ExtSyn : External signal brought to the core clock domain
Tg_Src_PushBotton : DREAM HIT based trigger (Self-Trigger) **Tg_Src_Soft** :
 Software generated trigger **Tg_Src_Constant** : Internally generated constant rate
 trigger **Tg_Src_Memory** : Internally generated trigger from memory pattern
Tg_Src_NegExp : Internally generated random trigger

The bottom four parameters make the internal trigger generator logic active, so **Rate** parameter is also active in each case.

Trig_Conf_TrigPipeLen is used to set the delay time of trigger which means the system trigger directly goes to readout logic. Its default value is '1' in terms of trigger clock cycle (described in next section). Actually, trigger generator produces two triggers: raw trigger and delayed copy. So the **TrigPipeLen** determines the time of the delayed copy.

Trig_Conf_TrigVetoLen is used to veto delay the trigger in trigger clock cycle. The maximum value of **TrigVetoLen** that could be 1023. This means 1023 trigger clock cycles which is equal to (1023×8) ns.

Trig_Conf_File is used to indicate a trigger configuration file, if any, but we don't use it here.

(c) Main configuration register

```

Feu * Main_Conf_ClkSel      OnBoardClk
Feu * Main_Conf_DreamMask  0xDF
Feu * Main_Conf_DreamPol  0x00
Feu * Main_Conf_SparseRd  2
Feu * Main_Conf_Samples    80
  
```

Main_Conf_ClkSel parameter could have 3 different values: 00 or **OnBoardClk**, 01 or **TrgIfConClk** and 1x or **RecClk**. In **OnBoardClk** 125MHz clock in the FEU is used which implies 8ns trigger clock cycle. While testing the prototype, we mostly use **OnBoardClk**. In **TrgIfConClk** the clock is due to the auxiliary trigger interface. Furthermore, in Clas12 μ Megas the clock recovered from the optical synchronous link from the backend units are used with parameter value **RecClk**.

`Main_Conf_DreamMask` is used to mask the DREAM channel of any FEUs. Each Feu has 8 DREAM chips and each chip has 64 channels. Here we should use hex format to declare the masking. For example, we use `0xDF` here. To understand better, we can convert the hex value to binary. Binary of `0xDF` is `11011111`, so we can easily say now that only one Dream chip (Dream 6) is unmasked and all other dreams are masked. This means only 64 channels corresponding to this channel are unmasked. If we want no mask at all, we then use `0x00`. We can do this in individual FEU mentioning FEU number in stead of using `*` as mentioned in Note above.

`Main_Conf_DreamPol` is used to choose the negative or positive polarity of the signal from the detector. `0x00` is default negative signal, and `0x01` for positive signals.

`Main_Conf_SparseRd` is used to sparse read the data. Different values from 0 - 3 can be used. 0 implies no spare reading, 1 implies every alternative data value is read, 2 implies first, fourth and seventh samples are read, and 3 implies the one out of four samples are read.

`Main_Conf_Samples` determines the number of samples in each event. The maximum value be 255, so no more that two events could be stored in 512 buffer for this sample size. So we should be sure about our trigger rate to put such large value. Based on the signal size and peaking value (it will be discussed later), we used 50-100 sample size in the RTPC prototype.

(d) Trigger logic register

```

Feu * Main_Trig_TimeStamp  0
Feu * Main_Trig_OvrWrnLwm  3
Feu * Main_Trig_OvrWrnHwm  6
Feu * Main_Trig_OvrThersh  62
Feu * Main_Trig_LocThrot   1

```

`Main_Trig_TimeStamp` is used to offset the timestamp of trigger. If It's value is set to '0', it will not offset the time everytime trigger is obtained, but if '1', it will offset the time.

`Main_Trig_OvrWrnHwm` is used to set the upper limit of number of triggers that will be queued in the trigger FIFO which can hold 64 triggers. If the number of triggers

in the deranzomization trigger FIFO surpass the `Main_Trig_OvrWrnHwm` value we set, Overflowwarning flag is set to '1'. This is quite helpful to determine the adequate trigger rate in the DREAM. As we have 512 cell circular buffer in the DREAM and the sample size is 80, the buffer could process upto 6 trigger at the same time. So `Main_Trig_OvrWrnHwm` is set to **6**.

`Main_Trig_OvrWrnLwm` is used to set the lower limit of trigger that will be queud in the trigger FIFO which helps to set the overflowwarning flag '0'. So if the trigger occupancy is less than `Main_Trig_OvrWrnLwm` value, the overflowwarning flag will be set to '0'. Based on the `Main_Trig_OvrWrnHwm` which is set to **6**, the `Main_Trig_OvrWrnLwm` is set to **3** (which should be less that upper limit)

`Main_Trig_OvrThersh` is also related with the number of maximum triggers corresponding to the FIFO. If the trigger occupancy increases this value allocated to `Main_Trig_OvrThersh`, an Overflow flag is raised which could be removed only by resetting or resynchronisation procedure. The best way of resetting is to restart the run again. If you don't reset, the data collected has no meaning at all after the Overflow.

`Main_Trig_LocThrot` is used for throttling the trigger in overflowwarning condition. If `Main_Trig_LocThrot` is set to '1', no trigger is accepted in overflowwarning condition, and if '0', triggers are accepted in warning condition as well.

(e) FEU Power register

```

Feu * Feu_Pwr_Dream    0xF
Feu * Feu_Pwr_PrtFlt   0xFFFF
Feu * Feu_Pwr_Adc      0

```

`Feu_Pwr_Dream` is used to power the DREAM of corresponding FEU. Among the 8 DREAM chips in one FEU, all DREAM are powered on using the value `0xF`. It's easy to visualize in binary. Binary value of `0xF` is `1111` and each bit is used to power a pair of DREAMs. Bit 1 is used to power on and bit 0 is used to power off. Hence we can set the value for this parameter in a range `0x0` to `0xF`.

`Feu_Pwr_PrtFlt` is used to ground or float the channels of within FEU. All the channels are grounded using `0xFFFF`. We can see this using binary value. Each bit in binary value represents 32 channels among 512 channels in a FEU, and bits 0 is used for floating and bit 1 for grounding.

`Feu_Pwr_Adc` is used for ADC synchronisation. Bits 0 or 1 are used as it's value where 0 means not ready and 1 means done.

(f) FEU Runcontrol register

<code>Feu * Feu_RunCtrl_Pd</code>	1
<code>Feu * Feu_RunCtrl_CM</code>	1
<code>Feu * Feu_RunCtrl_ZS</code>	0
<code>Feu * Feu_RunCtrl_ZsTyp 0</code>	
<code>Feu * Feu_RunCtrl_DrOvr</code>	0
<code>Feu * Feu_RunCtrl_RdDel</code>	0
<code>Feu * Feu_RunCtrl_ZsChkSmp</code>	3
<code>Feu * Feu_RunCtrl_CmOffset</code>	256
<code>Feu * Feu_RunCtrl_Id</code>	-1
<code>Feu * Feu_RunCtrl_AdcDatRdyDel</code>	8
<code>Feu * Feu_RunCtrl_EvTstExt</code>	0
<code>Feu * Feu_RunCtrl_DrDblSmpClk</code>	0
<code>Feu * Feu_RunCtrl_PdFile</code>	None
<code>Feu 1 Feu_RunCtrl_PdFile</code>	<code>ped_170824_20H48_000_01_ped.prg</code>
<code>Feu * Feu_RunCtrl_ZsFile</code>	None

`Feu_RunCtrl_Pd` is used to determine the pedestal subtraction. If we don't want pedestal subtraction, we use 0. Generally, while using only one config file to get both pedestal and signal data, we set the parameter value to 0 if we are collecting pedestals only. And for the pedestal subtraction, we use 1. When 1 is used along with a pedestal filename in the `Feu_RunCtrl_PdFile` parameter, we get output file of this run with automatic pedestal subtraction.

`Feu_RunCtrl_CM` is used for the common mode subtraction. If it's value is set to 0, it determines there is no common mode subtraction. But, if it is set to 1, it implies that the output file of the run will have data set after common mode subtraction embedded in the program.

`Feu_RunCtrl_ZS` is used to for the Zero Suppression. There is no zero suppression, if the value of `Feu_RunCtrl_ZS` is set to 0. But if it is set to 1, zero suppression in

allowed. After setting `Feu_RunCtrl_ZS` to 1, we should also put appropriate value of `Feu_RunCtrl_ZsChkSmp` to indicate how many samples to be compared with threshold for zero suppression.

`Feu_RunCtrl_ZsTyp` is the type of the zero suppression which could be two different types. One is BONuS12 type in which chunk of a signal sample over a large window are checked and taken out from FPGA, where as other type has zero-suppression effective over whole signal at once.

`Feu_RunCtrl_RdDel` is used to delay the DREAM read signal by fixed latency. It is mostly used for test purposes. If `Feu_RunCtrl_RdDel` is set to 0, the readout of DREAM starts with the trigger. If `Feu_RunCtrl_RdDel` is set to 1, the DREAM read signal is delayed by 1536 trigger clock cycles which corresponds to (1536×8) ns for Onboard 125 MHz clock.

`Feu_RunCtrl_ZsChkSmp` becomes active only if `Feu_RunCtrl_ZS` is set to 1. This parameter can have five different values 0, 1, 2, 3, and 4. If 0, samples 1 and 2 are compared with zero suppression threshold. If 1, samples 1, 2 and 3 are compared to threshold. Similarly, one more sample is compared for next value. So if 4, samples 1, 2, 3, 4, 5 and 6 are compared with the zero suppression threshold. Note that output contains sample 0 also, but in the above setting sample 0 is not compared with the threshold.

`Feu_RunCtrl_CmOffset` is used to configure the offset pedestal value in the output data after the common mode and pedestal subtraction. This parameter is active, if `Feu_RunCtrl_Pd` and `Feu_RunCtrl_CM` are active.

`Feu_RunCtrl_AdcDatRdyDel` is used to delay on waiting between the DREAM Read signal and corresponding ADC data. It is usually set to 8 clock cycles.

`Feu_RunCtrl_EvTstExt` is used to set the event id and time stamp filed width in the FEU data packet. If it is set to 0, event id and time stamp field are 12-bits width and FEU header are absent. However, if it is set to 1, the event id is extended to 24-bits, time stamp is extended to 45-bits and FEU header is also included in data.

(g) FEU Pulser register

<code>Feu * Feu_Pulser_DreamTst</code>	0x00
<code>Feu * Feu_Pulser_PulseWid</code>	512
<code>Feu * Feu_Pulser_Enable</code>	0

Pulser register is used for the test of electronics, so we disabled the pulser by setting `Feu_Pulser_Enable` to 0 while taking data using the electronics.

(h) FEU Prescale register

```
Feu * Feu_PreScale_EvtData  1
Feu * Feu_InterPacket_Delay 0
```

`Feu_PreScale_EvtData` is used to limit the event data sent to the backened unit or computer from FEU. If it is set to 1, FEU sends data of each event. However, if it is greater than 1, FEU ouputs event data in slower rate. For example, if it is set to 10 then event 10 and events divisible by 10 are only sent out by FEU.

`Feu_InterPacket_Delay` is used to delay the output in terms of trigger clock cycle.

(i) Communication register

```
Feu * UdpChan_Enable        1
Feu * UdpChan_MultiPackEnb 0
Feu * UdpChan_MultiPackThr 4888
Feu * ComChan_Enable        0
```

`UdpChan_Enable` is used to determine the UDP link between FEU and computer. Value set to 1 implies there is UDP connection and 0 implies there is no UDP connection. There could be Optical serial link connection in which we disable `UdpChan_Enable` by setting 0 and enable `ComChan_Enable`.

`UdpChan_MultiPackEnb` is to enable/disable the multi-packet data transfer. If it is set to 1 (i.e. enabled), several data samples are packed to a single UDP pack as buffer and sent to computer.

`UdpChan_MultiPackThr` is used to determine the threshold of multipacket, if `UdpChan_MultiPackEnb` is enabled. It's value depends on MTU (maximum transfer unit) of the devices used. When the `UdpChan_MultiPackThr` is set to a particular value, the UDP buffer is filled with data packets from FEU untill the buffer reach

the threshold. After exceeding the threshold, the UDP datagram is transferred to computer.

`ComChan_Enable` is used to determine the optical link between FEU and computer. Value set to 1 implies Optical connection and 0 implies no optical connection. When UDP link is used, we disable the Optical link by setting 0 in `ComChan_Enable`.

(j) Auxiliary Trigger Interface

```

Feu * TI_DcBal_Enc 0
Feu * TI_DcBal_Dec 0
Feu * TI_Ignore    1
Feu * TI_Bert      0

```

Auxiliary trigger interface is used when the TCM (Trigger and Control Module) is used, which also sets the clock accordingly as described in `Main_Conf_ClkSel`. We are not using TCM, so we don't care about auxiliary interface. Here, everything is disabled.

(k) Self trigger parameters

```

Feu * SelfTrig_DreamMask 0xFF
Feu * SelfTrig_Mult      7
Feu * SelfTrig_CmbHitProp01 0
Feu * SelfTrig_CmbHitPropFb 0
Feu * SelfTrig_DrmHitWid 63
Feu * SelfTrig_CmbHitWid 63
Feu * SelfTrig_TrigTopo  0
Feu * SelfTrig_Veto      180000

```

`SelfTrig_DreamMask` is used to active or mask the particular DREAM in the FEU for the Self-trigger. If the parameter `Trig_Conf_Src` in Trigger generator configuration above is set other than `Tg_Src_SelfTrig`, it's better to mask all i.e. set the value `0xFF`. There are eight DREAMs in each FEU and digit 1 is used for masking each DREAM. On the other hand, unmasking of particular DREAM of specific FEU is done using

Hex values if Self trigger is implemented. So we can put hex values from 0xFF to 0x00 while using Self trigger. For example to unmask DREAM 6 only, we use 0xDF.

`SelfTrig_Mult` is used to define the number of simultaneous hits required to generate trigger. It could be set to zero.

`SelfTrig_CmbHitProp01` is one bit register used to declare the active combined hit propagation over bussed signal. Bussed signal is used to propagate trigger to other FEUs using slow control cable. It is set to 0 to disable and set to 1 to enable.

`SelfTrig_CmbHitPropFb` is also one bit register used to declare the active combined hit propagation over the optical link. It is set to 0 to disable and set to 1 to enable.

`SelfTrig_DrmHitWid` is used to define the hit width in terms of trigger clock cycle to be considered active hit.

`SelfTrig_CmbHitWid` is used to define the combined hit width to be considered active. This is also expressed in terms of trigger clock cycle which is 8ns for Onboard clock in DREAM.

`SelfTrig_TrigTopo` is used to declare the use of topological trigger. If it is set to 0, it means simple coincidence trigger and if 1, it means topological trigger. If topological trigger is enabled, the topological pattern should be pre-defined in the next Self trigger topology sub-section.

`SelfTrig_Veto` is used to veto between two active combined hits in terms of trigger clock cycles.

(l) Self trigger topology

The self trigger topology is active only if `Feu * SelfTrig_TrigTopo` is set to 1 in self trigger parameters above. If this value is set to 0, topology is disabled. For the self-trigger topology, pre-calculated trigger pattern is required and is implemented by assymmetric dual port memory. In RTPC prototype we have not used topology, so it is always disabled. Hence, we don't care about parameter values in the topology register.

(m) DREAM registers

```

Feu * Dream * 1 0x081F 0xC023 0x0000 0x0000
Feu * Dream * 2 0x0000 0x0008 0x0000 0x0000
Feu * Dream * 3 0x0000 0x0000 0x0000 0x0000
Feu * Dream * 4 0x0000 0x0000 0x0000 0x0000

```

```

Feu * Dream * 6 0xFFFF 0xFFFF 0xFFFF 0xFFFF
Feu * Dream * 7 0xFFFF 0xFFFF 0xFFFF 0xFFFF
Feu * Dream * 8 0xFFFF 0xFFFF 0x0000 0x0000
Feu * Dream * 9 0xFFFF 0xFFFF 0x0000 0x0000
Feu * Dream * 10 0xFFFF 0xFFFF 0x0000 0x0000
Feu * Dream * 11 0xFFFF 0xFFFF 0x0000 0x0000
Feu * Dream * 12 0x000F 0x0000 0x0000 0x0000

```

In each FEU, we have 12 DREAM chips, and each FEU and DREAM could be declared by putting the corresponding FEU number and DREAM number in above parameter list. Just replace the * by corresponding number to apply for particular parameter in the FEU or DREAM you would like a change.

The digit after `Feu * Dream *` in each line imply the DREAM register number and after that parameter values for that register in hexadecimal format. The parameter values in this config file are written in 64 bits format, so while dealing with 16 bits register we care only first column, while dealing with 32 bits register we set values in first two columns and for 64 bits all the four columns. The remaining columns are set to zero. The details of the use of different bits is described in DREAM Users manual.

Register 1 is 32 bits register which controls the main configuration parameters, so we set parameter values in first two columns and last two columns are left zeros.

Register 2 is also 32 bits register which is used for the test modes and to control SCA (Switched Capacitor Array) readout.

Register 3 and 4 are also 32 bits registers and used to select the channels for the test mode. Register 3 is used for channels 1 to 32 and register 4 for channels 33 to 64 of the specific DREAM chip.

Register 5 is 16 bits register which contains the version number of circuit so we don't need to configure it.

Register 6 and 7 are 64 bits registers which are used to configure the gain of the channels. The gain of the CSA (Charge Sensitive Capacitor) are defined from 4 different pre-defined capacitors (50fC, 100fC, 200fC and 600fC) as described in DREAM manual.

Register 6 is used for channel 1 to 32 and register 7 for channel 33 to 64 of the specific DREAM chip.

Register 8 and 9 are 32 bits registers which are used to inhibit the discriminator of the particular channel of the DREAM chip. Register 8 is used for channel 1 to 32 and register 9 for channel 33 to 64 of the specific DREAM chip.

Register 10 and 11 are also 32 bits registers which are used to enable the SCA readout of channels. Register 10 is used to enable channel 1 to 32 and register 11 to enable channel 33 to 64 of the specific DREAM chip.

Register 12 is 16 bits register, however only 9 bits are currently used. This means the maximum hex value is 0x01FF. This register is used to specify the trigger latency. The trigger latency is easy to understand from the following figure:

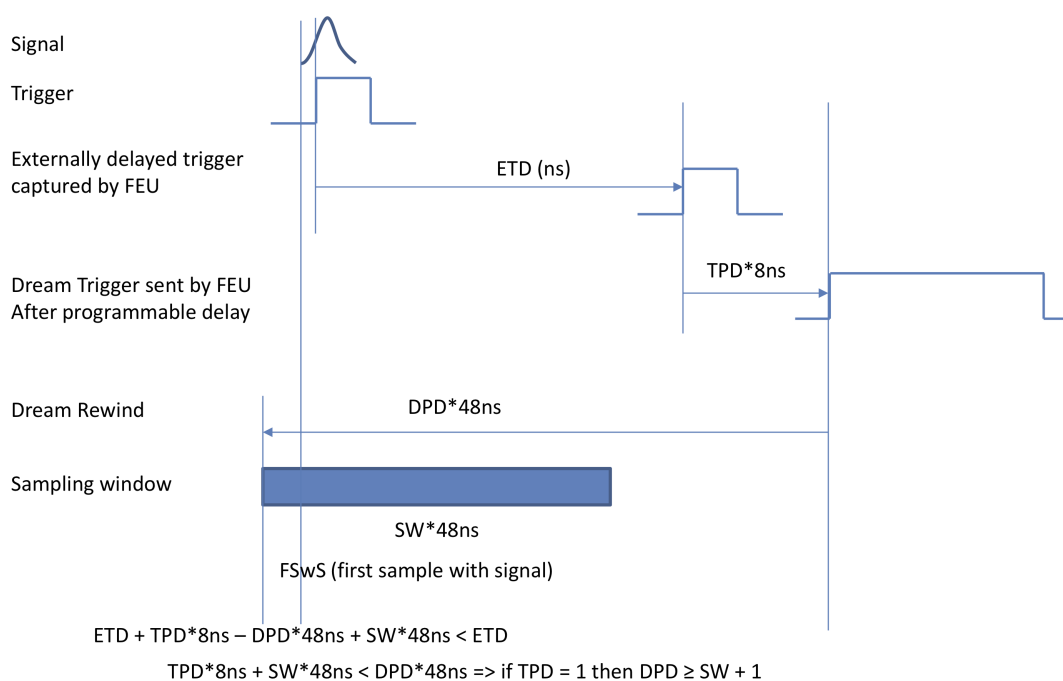


FIG. 92: Delay setting with various parameters.

(n) ADC register

```
Feu * Adc 0x16 0x00 1
```

ADC register AD92222 ADCs are used in FEU, which are octal (8 ADCs integrated into one pack) 12-bit with 40/50/65 MSPS analog to digital converters. It can operate at a maximum 65 MSPS. It has 325 MHz full-power analog bandwidth which can operate upto 390 MHz frequency and supports double data rate operation.

(o) DREAM clock values

```
Feu * DnmClk RdClk_Div      5.0
Feu * DnmClk WrClk_Div      5.0
Feu * DnmClk WrClk_Phase    2
Feu * DnmClk AdcClk_Phase   5
```

Dream Read-clock and write-clock division 5.0 corresponds to 40 ns bins and 6.0 to 48 ns bins.

APPENDIX D

RG-A 2018 OUTBENDING FIDUCIAL

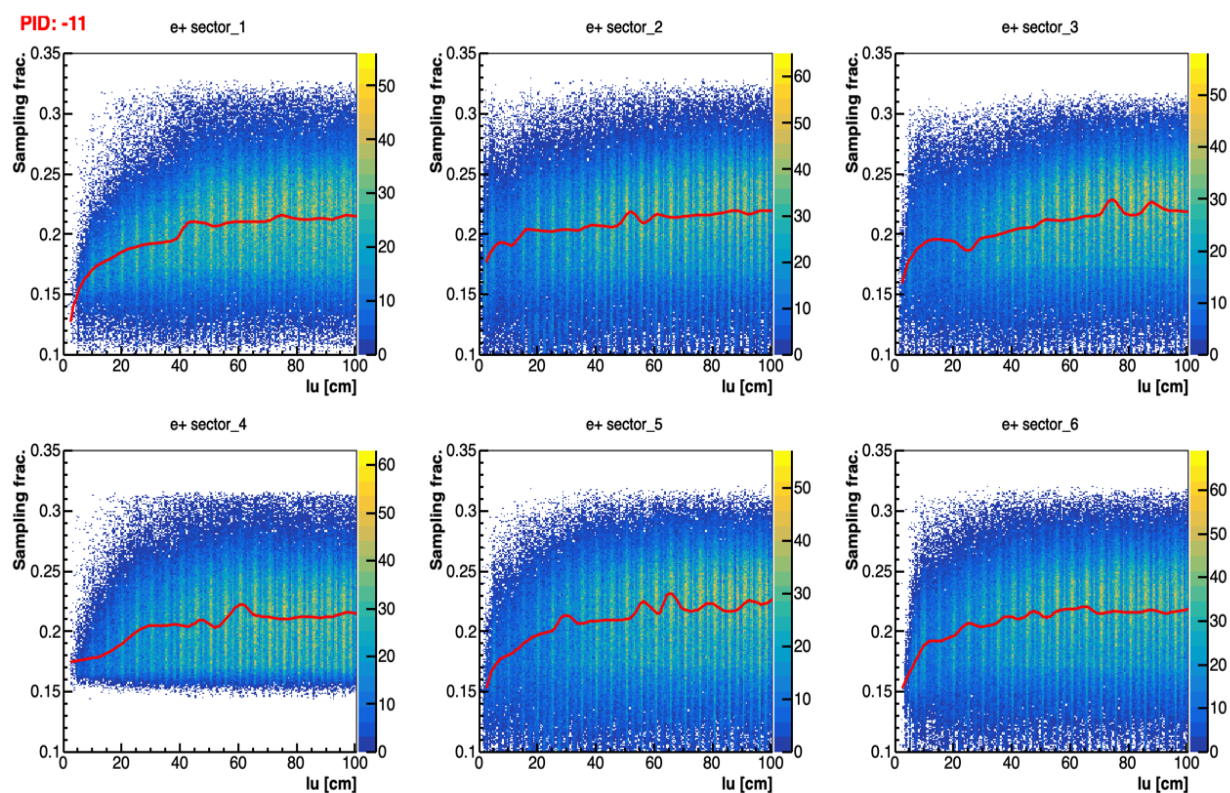


FIG. 93: Positron sampling fraction in correlation with lu (zoomed in near edge) in six different sectors of CLAS12. Red line shows the average sampling fraction corresponding to the x-axis bins.

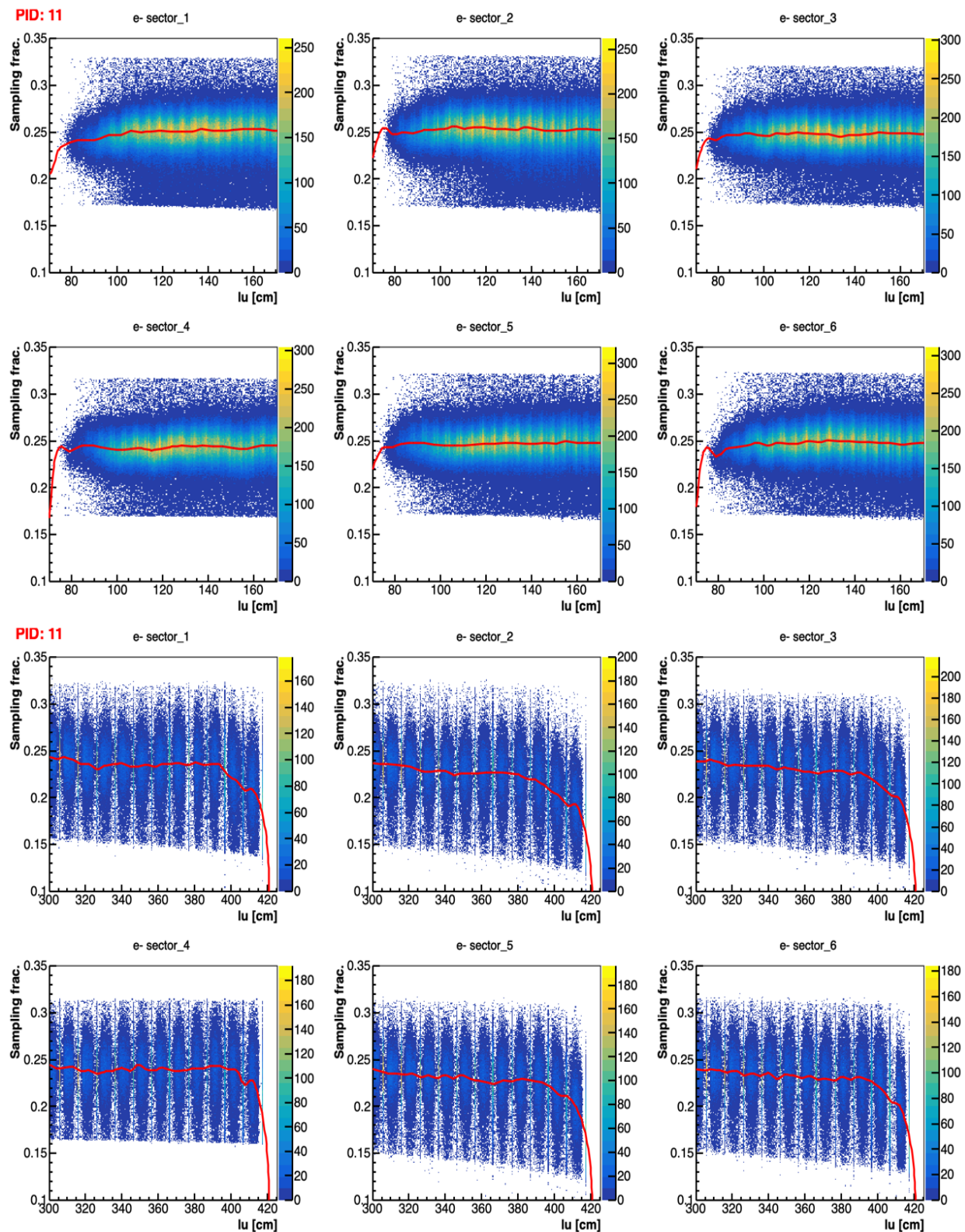


FIG. 94: Electron sampling fraction in correlation with lu (zoomed in near edge). Red line shows the average sampling fraction corresponding to the x-axis bins.

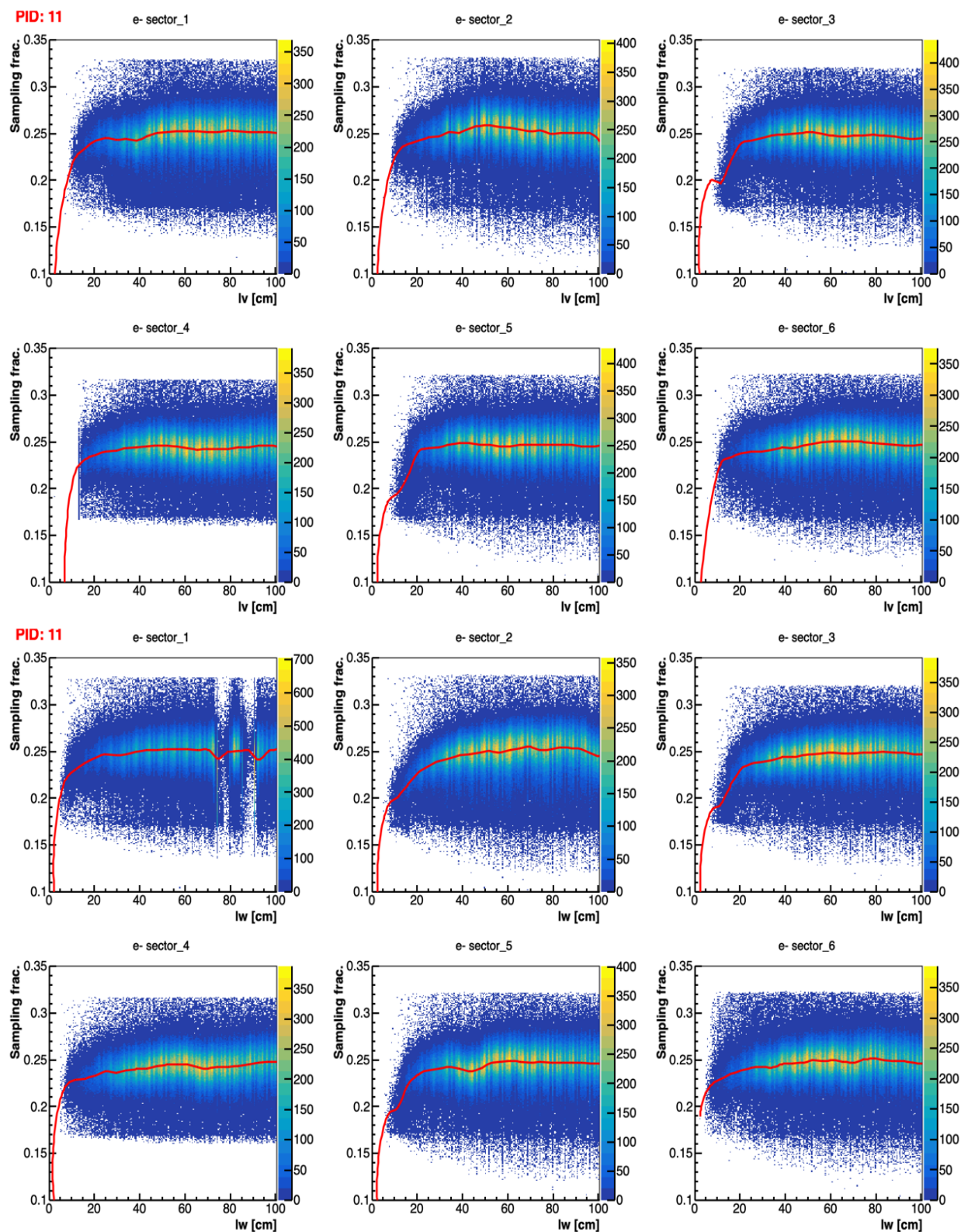


FIG. 95: Electron sampling fraction in correlation with lv (top) and lw (bottom) (zoomed in near edge). Red line shows the average sampling fraction corresponding to the x-axis bins.

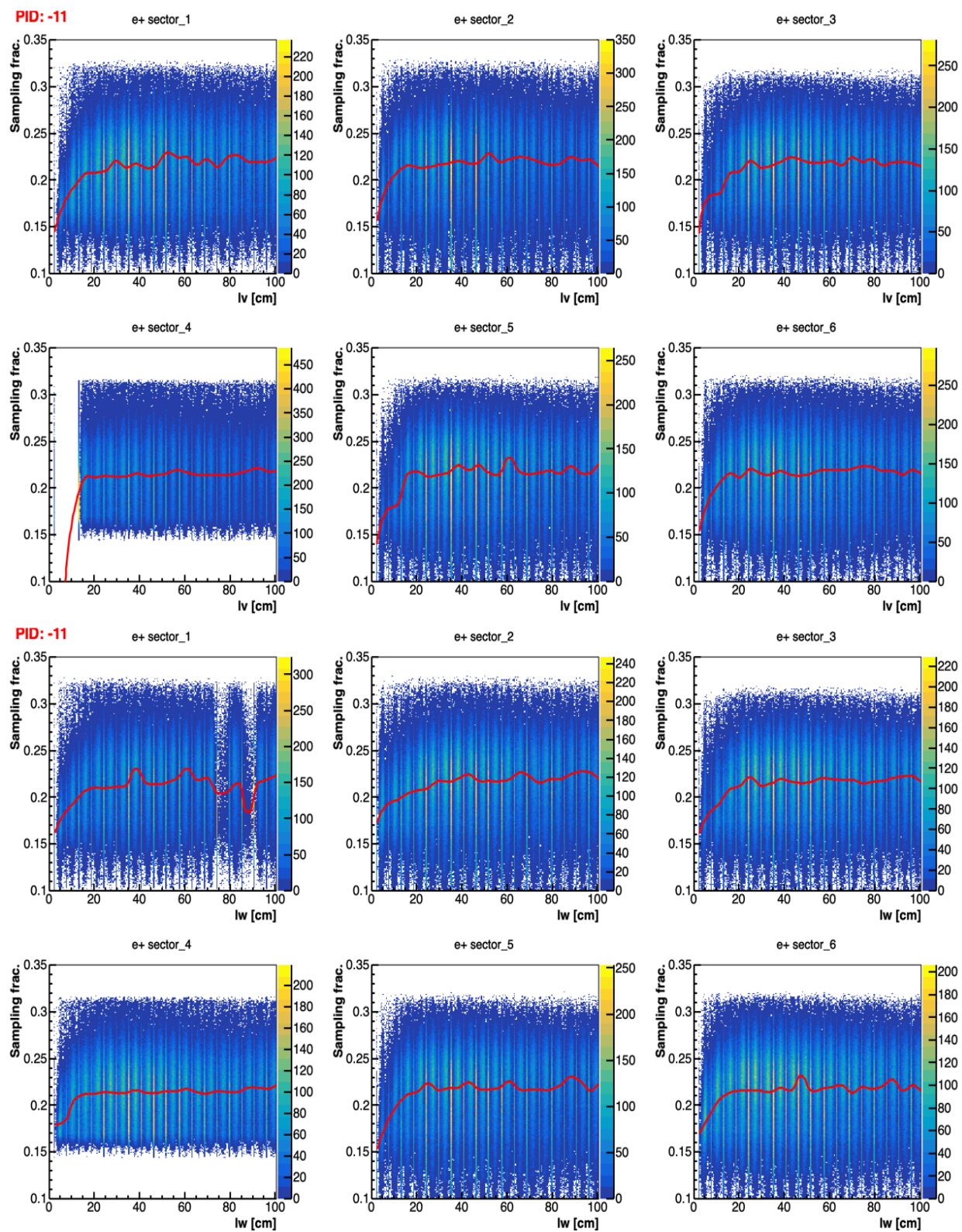


FIG. 96: Positron sampling fraction in correlation with lv and lw (zoomed in near edge). Red line shows the average sampling fraction corresponding to the x-axis bins.

APPENDIX E

RG-A 2018 INBENDING DISTRIBUTIONS

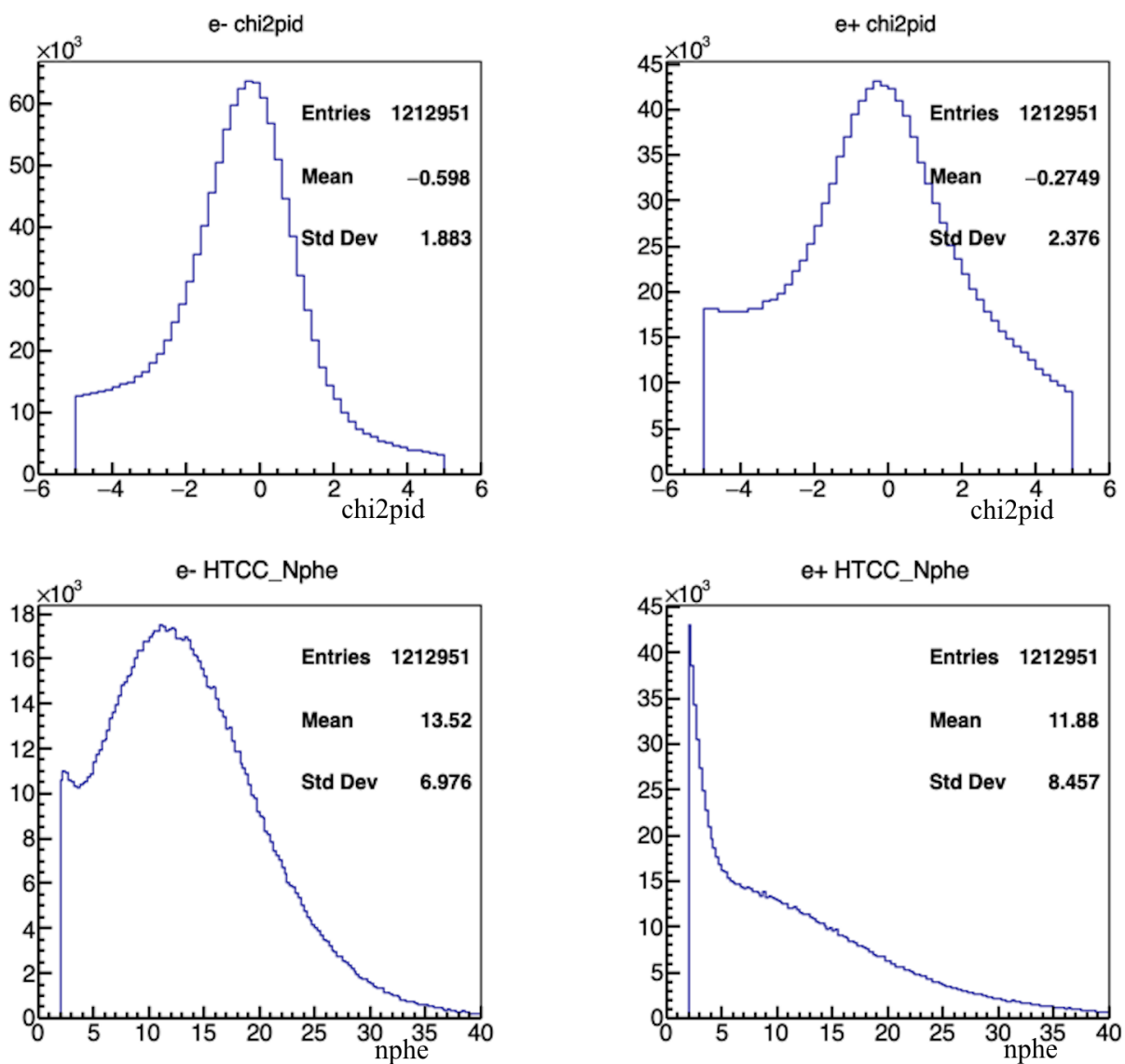


FIG. 97: Distribution of e^- (left) and e^+ (right) of EC sampling fraction χ^2_{pid} (bottom) and HTCC photoelectrons (top) in 2018 inbending run.

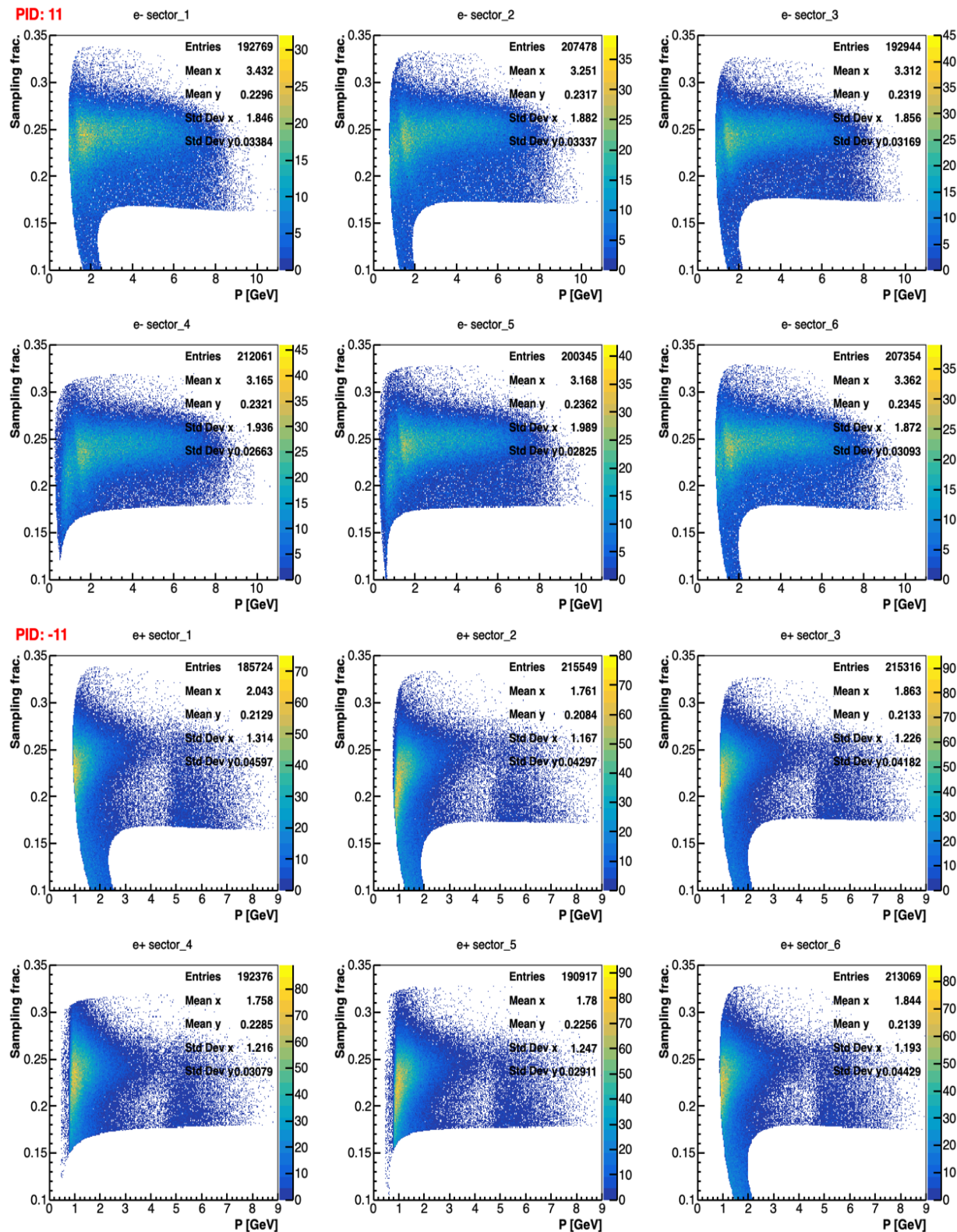


FIG. 98: Sampling fraction distribution of e^- and e^+ as a function of momentum in six different sectors of CLAS12 for 2018 Inbending runs (top 6: electrons, bottom 6: positrons).

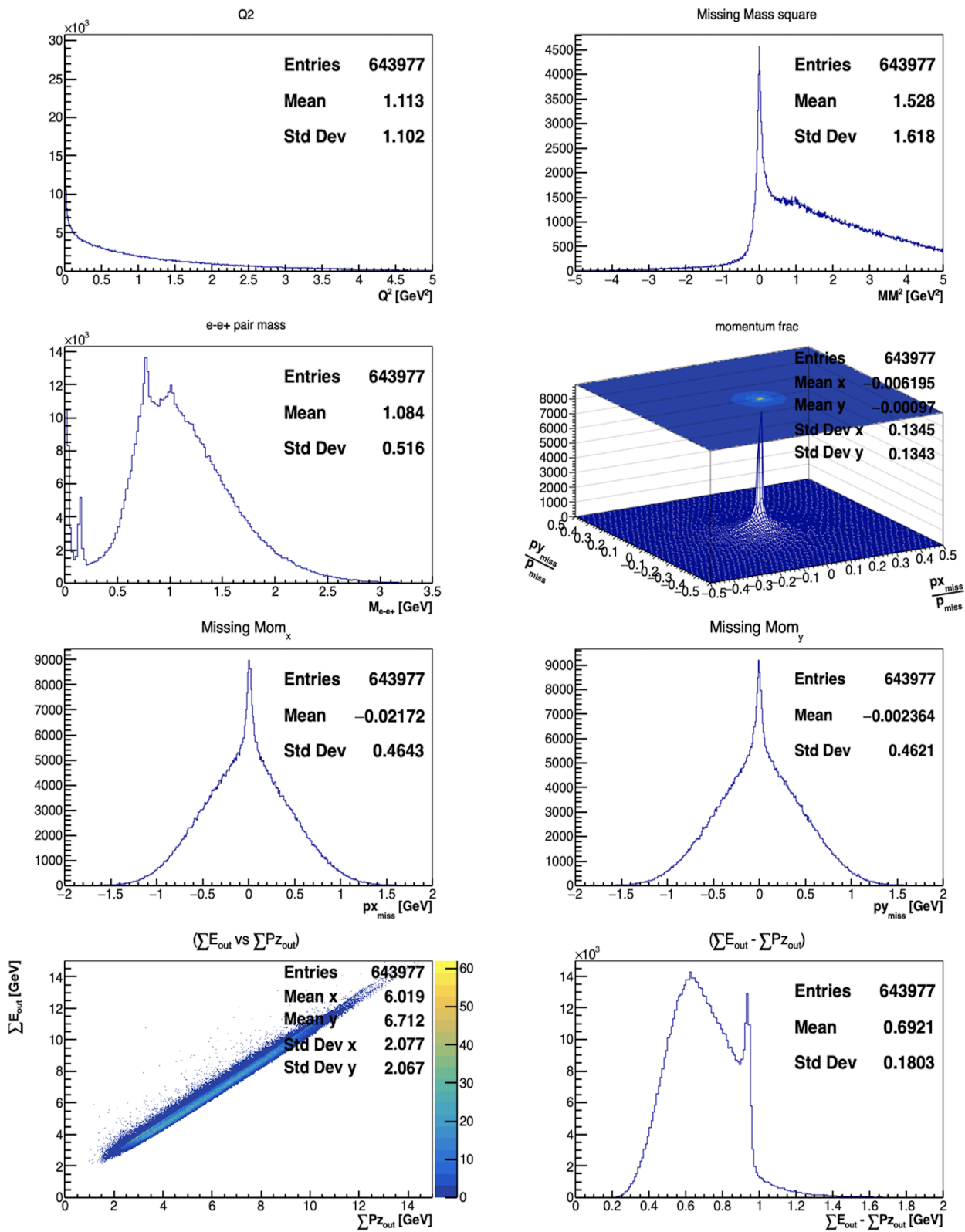


FIG. 99: Distribution of TCS kinematic variables among the sample events before the selected TCS kinematic cut (2018 Inbending run).

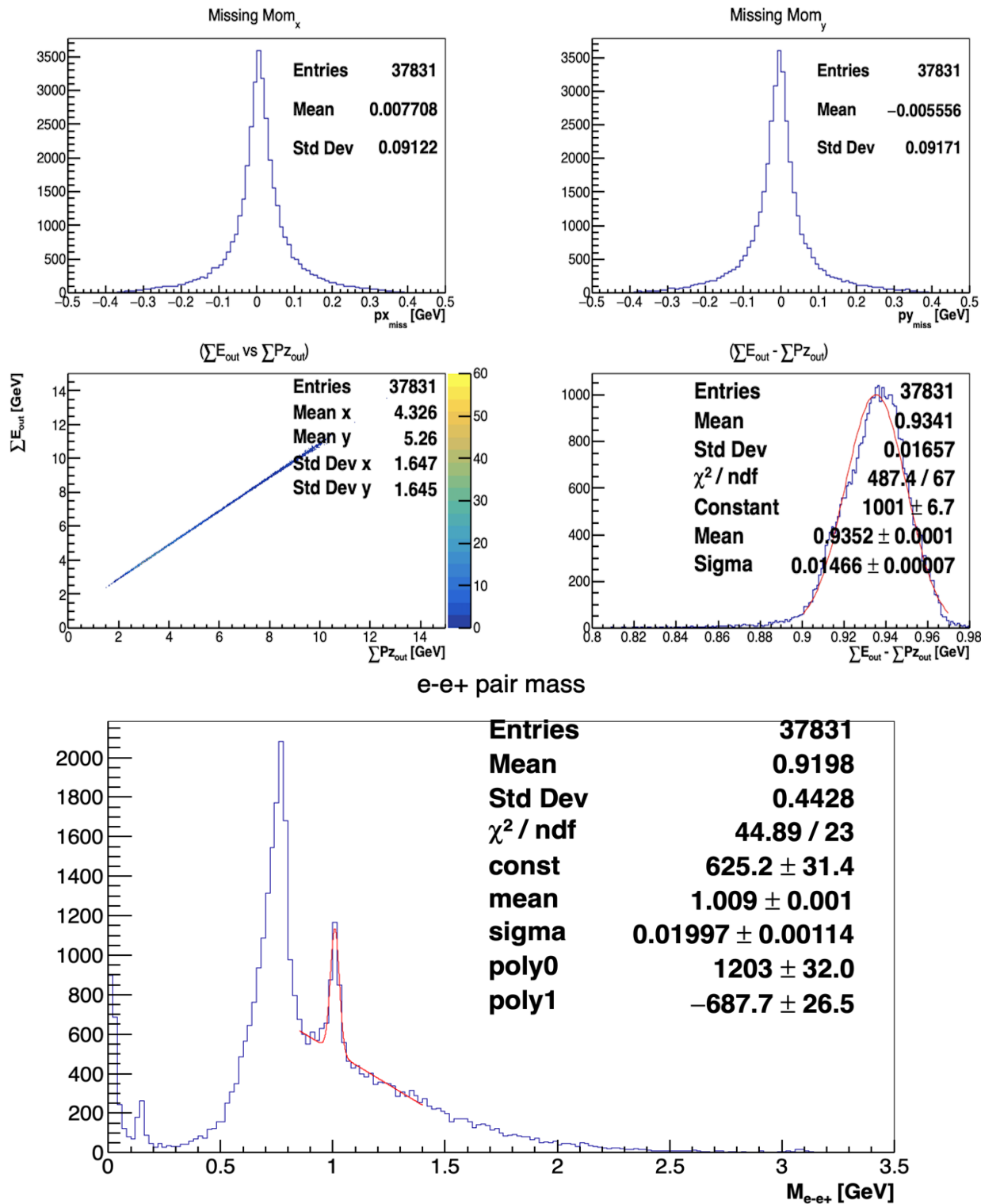


FIG. 100: TCS kinematic variables after the selected MM^2 and transverse momentum cuts (2018 Inbending run).

VITA

Jiwan Poudel
Department of Physics
Old Dominion University
Norfolk, VA 23529

Jiwan Poudel enrolled in PhD program at Old Dominion University in 2015 . Mr. Poudel joined the Experimental Nuclear/Particle Physics group in 2016. He became a doctoral candidate in 2016, and also got MS degree en route to PhD in May 2017. The projected date of doctoral graduation is May 2022. Jiwan Poudel is a member of American Physical Society and CLAS Collaboration at Jefferson Lab, VA.